Optimal Sizing and Control of Battery Energy Storage Systems for Hybrid-Electric, Distributed-Propulsion Regional Aircraft

Presented in Partial Fulfillment of the Requirements for the Degree Master of Science in the Graduate School of The Ohio State University

By

Aaronn Sergent, B.S.

Graduate Program in Mechanical Engineering

The Ohio State University

2020

Thesis Committee:

Professor Marcello Canova, Advisor

Professor Yann Guezennec

Professor Giorgio Rizzoni

Abstract

Volatile oil prices, rapidly increasing air travel demand, growing concern for health and climate impacts of emissions, and limited performance of existing aircraft technologies have generated substantial interest in distributed propulsion and hybridization, even without significant government regulation. This work details the development of the Map-based Aircraft Propulsion Simulator (tMAPS), a modular framework of reduced-order models of aircraft propulsion subsystems, and its application in optimizing the size and control of a battery energy storage system (BESS) in a hybrid-electric, distributed-propulsion (HEDP) regional jet aircraft. tMAPS is validated against the NPSS-based Georgia Tech Hybrid Electric Aircraft Test-bed. The supervisory energy management strategy is formulated into a discrete-time optimal control problem and solved via dynamic programming. Both state-of-the-art and future battery technologies are evaluated, with energy density ranging from 230-400 Wh/kg and power density ranging from 350-1200 W/kg. The optimal energy management strategy is evaluated as a function of BESS size, cell chemistry, and mission range to deduce system-level implications. The performance of HEDP is compared to a turbo-electric, distributed-propulsion (TEDP) aircraft that assumes improvements in weight, drag, and engine efficiency consistent with a regional jet entering operation in 2035.

Dedication

To my family, who have shown me constant love and support; to my friends, who share with me all the challenges and excitement of life; and to my mentors, who have taught me perserverance and guided my path

Acknowledgments

I would like to first thank Prof. Marcello Canova, Dr. Matilde D'Arpino, Prashanth Ramesh, and Prof. Yann Guezennec for their support and guidance during my Master degree studies. I am thankful for the technical feedback of Mike Ramunno and Chris Perullo (Georgia Tech) specifically related to this work. I am grateful for the financial support of the NASA University Led Initiative (ULI) program. There are many who are responsible for the wealth of opportunity at the Center for Automotive Research (CAR), but I would especially like to thank Giorgio Rizzoni, professor and director of CAR, for his longstanding commitment to develop the center. Lastly, thank you to Polina, Mike (again), Shreshta, Sai, Chitra, Ke, and the Buckeye Current team members (through the years) for being friends, in addition to coworkers.

Vita

July 1995 . . . . Born,
Canton, OH, USA

May 2013 . . . . High School Diploma,
Dover High School, OH, USA

Dec. 2017 - July 2018 . . . . Undergraduate Research Associate,
Center for Automotive Research,
The Ohio State University, OH, USA

May 2018 . . . . B.S. Mechanical Engineering,
The Ohio State University, OH, USA

Aug. 2018 - Present . . . . Graduate Research Associate,
Center for Automotive Research,
The Ohio State University, OH, USA

Publications

M. D'Arpino, M. Cancian, A. Sergent, M. Canova, and C. Perullo, "A Simulation Tool for Turbo-Hybrid-Electric Aircraft Battery Life Predication for the NASA ULI Program," *AIAA Propulsion and Energy Forum*, 2019.

A. Sergent, M. Ramunno, Matilde D'Arpino, M. Canova, and C. Perullo, "Optimal Sizing and Control of Battery Energy Storage Systems for Hybrid Turboelectric Aircraft," *SAE AeroTech*, 2020.

Fields of Study

Major Field: Mechanical Engineering

Table of Contents

List of Tables

List of Figures

Chapter 1: Introduction

1.1 Motivation

Oil prices have always been and will continue to be a driver for electrification in the transportation industry, but a growing influence is public concern for environmental pollution, global warming, and emissions' health impacts. Public concern elicits government regulation and design evolution. While, light-duty vehicles are predicted to remain the main source of fuel consumption and emissions, unprecedented growth in air travel demand is forecast, and action is warranted. Beginning in the 1990s, research interest developed in the area of aircraft electrification; coupled with the development of hybrid-electric and fully-electric ground vehicles, rapid advancement in the associated technologies was achieved, resulting in the recent development and production of "more-electric aircraft" (MEA). The Airbus A380 (first delivered in 2007) and Boeing 787 (first delivered in 2011) feature substantial increases in electric power generations, and electrification of propulsion systems is now a highly active area of research in academia, industry, and government, alike.

1.1.1 Oil Market Outlook

The volatile and upward-trending price of fuel has historically been the driver for research and development to improve the fuel efficiency of aircraft and other vehicles. The cost of jet

fuel more than quadrupled in recent decades (Figure 1.1). Oil prices are subject to available

supply, worldwide economic growth/decline (demand), and geopolitical developments.
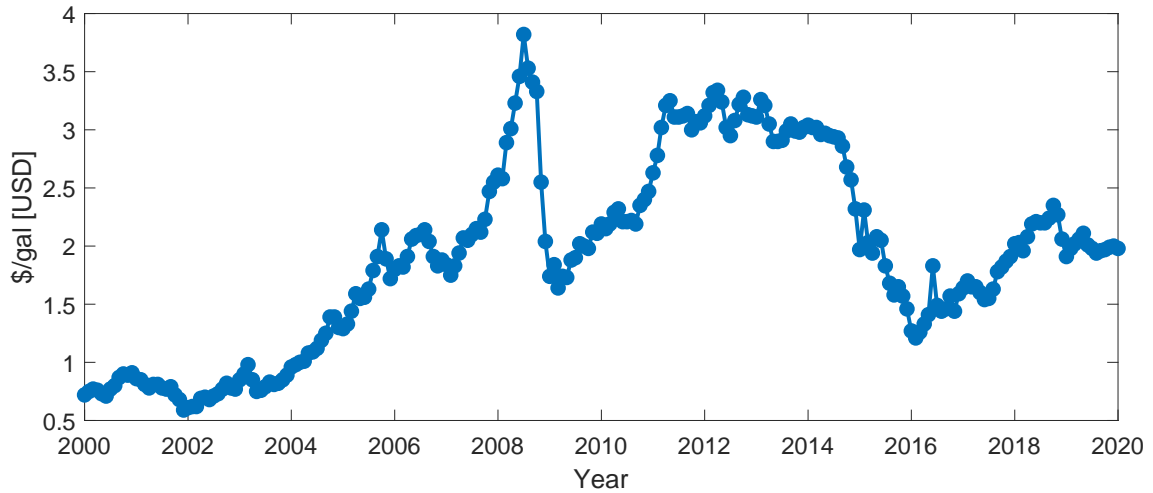
Figure 1.1: Cost of jet fuel for US Carriers (20M USD revenue/yr) from 2000-2020 [US Bureau of Transportation Statistics]

North Sea Brent crude oil is used to price two-thirds of the world's internationally

traded crude oil and, thus, serves as a good indicator for global oil cost. The US Energy

Information Administration's 2020 Annual Energy Outlook projects the price of Brent crude

oil to increase by approximately 58% (in 2020 dollars) by 2050 (Figure 1.2). The model

cannot forecast instability in the market, but assessments of international markets were

considered to be most influential, and extreme scenarios were evaluated in which supply or

demand outweighs the other in the low and high oil price cases, respectively.

Major changes in oil market dynamics could increase instability in the market and

cause end-users to quicken their pace of diversifying their energy consumption (Figure 1.3).

United States (US) shale oil production has seen rapid growth in recent years and is expected

AEO2020 North Sea Brent crude oil price
2019 dollars per barrel

2019
history | projections

200
180 — High Oil Price
160
140
120 — Low Oil and Gas Supply
100 — Reference
80 — High Oil and Gas Supply
60 — Low Oil Price
40
20
0

2010   2020   2030   2040   2050
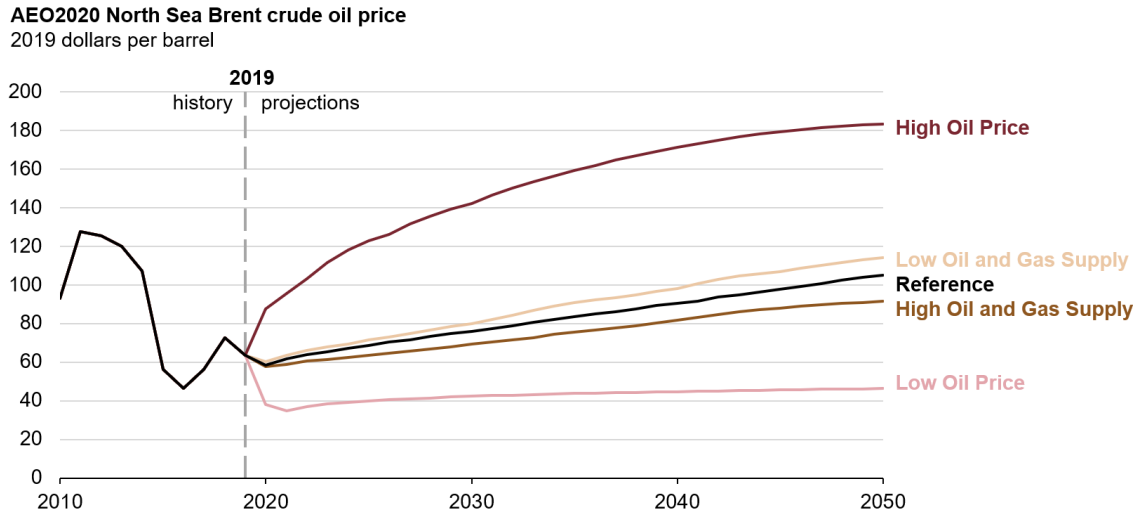
Figure 1.2: North Sea Brent crude oil price projections [5]

to have continued growth, enabling the US to become a net exporter of petroleum [5]. The share of global oil production of the Organization of the Petroleum Exporting Countries (OPEC) plus Russia is expected to drop to 47% by 2030, but OPEC should remain the largest net exporter of oil to world markets, according to the International Energy Agency (IEA) [6]. As economies in the Middle East, Africa, and Asia-Pacific develop, their demand for imported oil is projected to increase substantially, which could place pressure on the OPEC and create tension between countries in these regions.

1.1.2 Air Travel Market Outlook

Recently, increasing concern regarding the environmental impacts of aircraft and anticipation of significant increases in demand of air transportation have compounded with the oil market outlook to further elevate the priority of high-energy-efficiency aircraft technology. There is a mutual benefit for airlines and consumers in achieving significant improvement
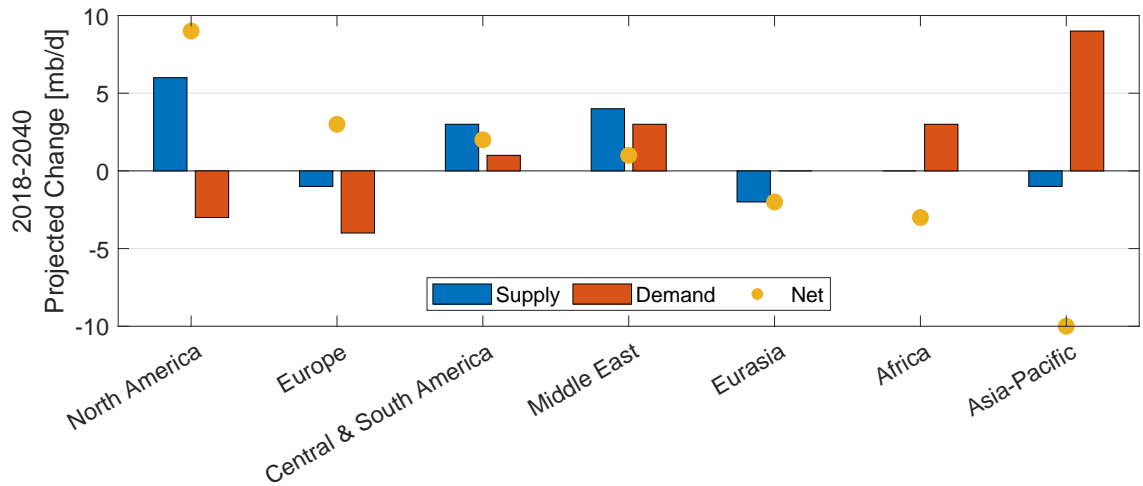
Figure 1.3: Change in oil demand, supply, and net trade position, 2018-2040 [6]

in energy efficiency, as energy consumption and emissions are directly related to fuel consumption in modern-day aircraft. Boeing's 2019-2038 Commercial Market Outlook reports average growth of 6.7% in Revenue Passenger Kilometers (RPK) over the past five years due to growth in travel and tourism. A combination of lower cost fare, growing middle class (earning >$20,000 USD in purchasing power parity) in large emerging markets, and new airline business models have enabled a growing percent of the global population to travel by air. Between 2008-2018, the increase of approximately three billion RPKS (60%) was led by 40% growth between/within emerging markets, 34% between advanced and emerging markets, and 26% between/within advanced markets [1]. Forecasts for growth until 2038 are summarized in Table 1.1.

The Asia-Pacific market, containing China, Southeast Asia, South Asia, Northeast Asia, and Oceania, is projected to continue to be the primary contributor of global aviation growth due to rapid growth in consumer purchasing power, in intra-regional economies, and in

Table 1.1: Summary of Boeing's 2019-2038 Commercial Market Outlook [1].

Market	GDP Growth [%]	Traffic Growth [%]	Fleet Growth [%]	Aircraft Deliveries
China	4.7	6.0	4.5	8,090
Southeast Asia	4.4	5.9	5.7	4,500
South Asia	5.8	7.4	7.3	2,560
Northeast Asia	1.2	1.9	1.5	1,420
Oceania	2.4	2.7	2.6	820
North America	1.9	3.2	1.9	9,130
Europe	1.6	3.6	2.9	8,990
Middle East	3.2	5.1	4.9	3,130
Latin America	2.9	5.9	3.9	2,960
Russia and Central Asia	2.0	3.3	2.1	1,280
Africa	3.4	5.9	4.0	1,160

intra-regional economic ties considering also the vast geographical area and many island nations. Africa is projected to have the largest working age population (1060 million) by 2040, economic diversification is expected to stabilize and grow the African economies, and policy changes have been adopted with hopes to liberalize the civil transportation market. Sustained market growth projected in Europe combined with the aforementioned growth in Asia-Pacific and Africa leads to growth in the Middle East, which serves as the hub for these markets, connecting 80% of the world's population and economies responsible for 70% of global economic growth (2019-2038) via an eight hour flight [1].

North America is expected to see sustained growth as network carriers focus on optimizing their fleets and operations to increase load factors and extend international networks. Market liberalization and expansion of low-cost carriers are projected to significantly increase travel within South America, while economic ties and tourism will sustain demand for travel between North America and Latin America.
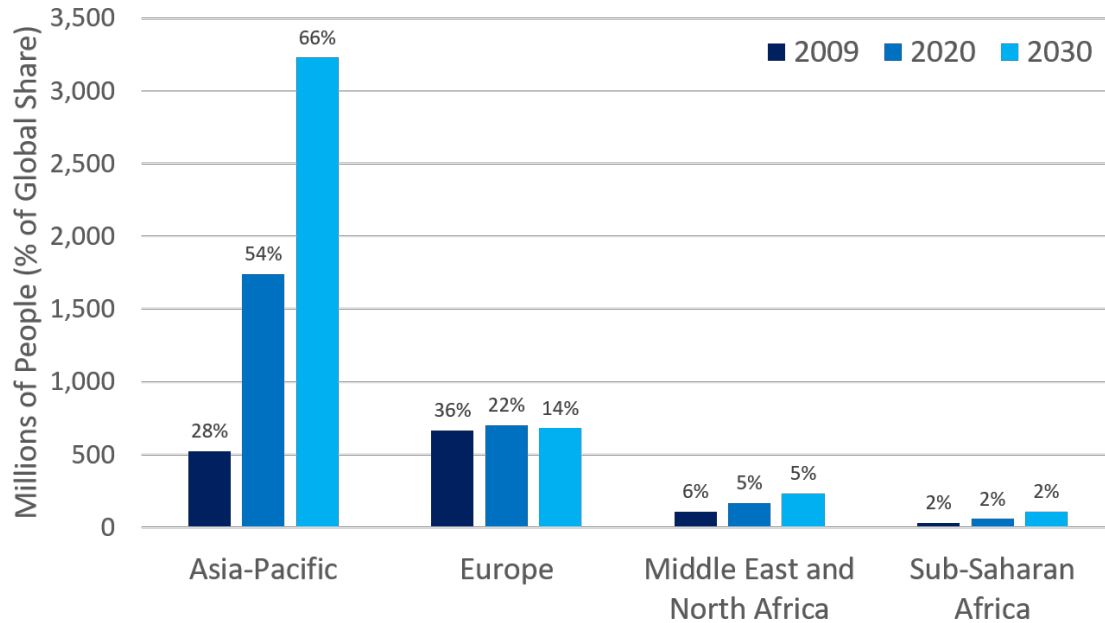
Figure 1.4: Projection of middle class population in the Middle East and surrounding markets from 2009-2030 [7]

1.1.3 Health and Environment

Between 1998-2013, carbon dioxide (CO_2) emissions per RPK have reduced 51%, and emissions have increased by only 33% of the traffic volume growth [1]. However, according to the IEA's Sustainable Development Scenario (SDS), which presents a solution "fully aligned with the Paris Agreement...and meets objectives related to universal energy access and cleaner air," transportation sector energy consumption must be reduced by 276 Mtoe (Mega tonnes oil equivalent) by 2040. The Stated Policies Scenario (STEPS), which incorporates policy initiatives already in place, predicts a 701 Mtoe increase in consumption [6].

While transportation accounts for only 24% of US energy consumption, it is responsible for approximately 36% of CO_2 emissions because of its heavy reliance on oil and efficiency

limitations of on-board, combustion-based power plants. Transportation consumption and emissions are projected to decline through 2030 largely due to substantial improvements in on-road vehicle energy efficiency; however, regulations do not require additional efficiency improvements after 2027, and travel growth quickly outpaces efficiency gains anticipated this decade. Meanwhile, jet fuel consumption is projected to steadily increase 31% by 2050, again as the rate of technological advances is not expected to match the rate of increasing demand [5].
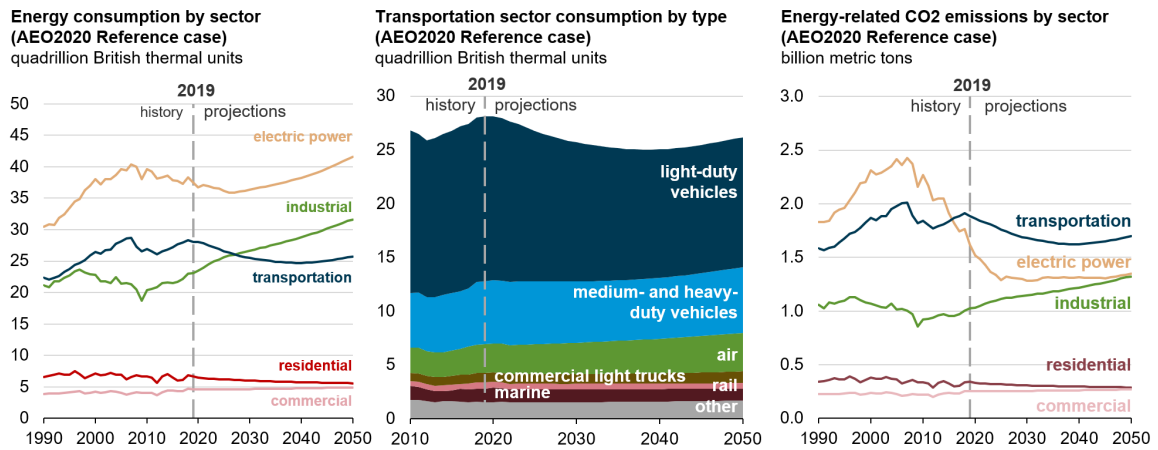
Figure 1.5: Projections of US energy consumption by sector and by transportation type and CO_2 emissions by sector between 2020-2050 [5]

Aviation emissions not only adversely affect climate change but also human health, which is estimated to have economic impacts nearly equal to, if not greater than, climate costs. While CO_2 emissions are primarily a contributor to climate change, non-CO_2 emissions are also responsible for damage to both the climate and human health (Table 1.2). Non-CO_2 emissions include water (H_2O), nitrates (NO_x), sulfates (SO_x), hydroxide (OH), carbon monoxide (CO), hydrocarbons (HC), and fine particulate matter (PM 2.5). Grobler *et*

al defined speciated cost metrics for both climate and air quality per unit aviation fuel consumption. Referencing the fuel consumption and emissions data from the US Federal Aviation Administration's (FAA) Aviation Environmental Design Tool (AEDT) for 2006, the total cost was determined to be $560/mt (metric ton) of fuel burned (2015 USD) with 90% of the cost resulting from cruise emissions (relative to other phases of flight) and 64% from air quality impacts (relative to climate impacts) [4]. In a similar study focused on health impacts, again referencing data from 2006, 16,000 premature deaths were predicted from global, full-flight emissions with an estimated cost of $112/mt of fuel burned (2006 USD) with 75% of global health impacts due to cruise emissions [3].

Boeing's fleet growth and replacement forecast comprises 44,040 aircraft deliveries with just 6,620 of existing aircraft remaining in service by 2038, which presents an opportunity [1]. Current regulation and technology improvements correlate to significantly increased fuel consumption; thus, investment in advanced aircraft concepts and improvement in fuel efficiency must rapidly grow to surpass current projections and mitigate global climate and health impacts anticipated from the future demand in civil aviation.

1.1.4   More-Electric Aircraft

A potential path towards reduction of fuel consumption and CO_2 emissions involves improving the energy conversion efficiency of power generation or propulsion systems. The first systems in ground vehicles to be electrified were primarily safety and comfort systems or engine accessories [19]. More recently, there has been a focus on hybridization of the propulsion system through electrification and engine downsizing. The concept of an "all-electric" aircraft originated in military aircraft designed in World War II, though, until recently, low technology levels of electrical power generation and conversion devices,

Table 1.2: Summary of aviation CO_2 and non-CO_2 emissions' impact on human health and the climate [2, 3, 4]

Species	Source	Climate Impact	Health Impact
CO_2	Primary combustion product, decreases with increasing combustion pressure and temperature	Greenhouse gas (warming)	N/A
H_2O	Primary combustion product	Water vapor emission (warming), contrail precursor (net warming)	N/A
NO_x	Trace combustion product, increases with increasing combustion pressure and temperature	Formation of O_3 (warming), aerosol (cooling) and contrail cirrus precursors (net warming) from HNO_x	NO_3^- Combines with NH_4^+ to form secondary PM 2.5, O_3 linked to respiratory disease
SO_x	Trace combustion product, increases with increasing fuel sulfur content and combustion pressure and temperature	Combines with OH to form H_2SO_4, likely the most important aerosol precursor (cooling)	SO_4^{2-} combines with NH_4^+ to form secondary PM 2.5
OH	Trace combustion product	Combines with NO_x (reducing O_3 formation, cooling) and with SO_x (aerosol precursor, cooling)	O_3 linked to respiratory disease
CO	Trace combustion product, results from incomplete combustion	N/A	Poisonous gas
HC	Trace combustion product, results from incomplete combustion	Aerosol formation and growth (cooling)	N/A
PM 2.5	Trace combustion product	Particle emission (warming), uncertain impact on cirrus cloud formation (warming/cooling)	Increased rates of lung cancer, cardiovascular disease, and respiratory disease

coupled with limited understanding of the system control, inhibited the inclusion of "more electric" power systems in aircraft. Programs such as US Air Force More Electric Aircraft (Generation I: 1991-1998, Generation II: 1998-2005, Generation II: 2005-2012), Totally Integrated More Electric Systems (2001-2004), and Power Optimized Aircraft (2002-2007) were responsible for driving the acquisition of knowledge and development of technology required to make increased reliance on electrical power a feasible solution [20, 21, 22].

The concept of MEA is based on replacement of existing mechanical, hydraulic, and pneumatic non-propulsive systems with electrical power systems (Figure 1.6). Conventionally, a relatively small amount of engine power is converted to four main forms of non-propulsive power: mechanical, hydraulic, pneumatic, and electrical. Hydraulic and pneumatic systems have low transfer efficiency and are prone to leaks that decrease system efficiency, have the potential to fully disrupt operation of the network, and are difficult to locate and repair, resulting in grounded aircraft. Hydraulic systems are robust and have high power density but their heavy and inflexible piping limits optimization of system integration and potential for future aircraft reconfiguration [23]. Research and development of distributed electro-hydraulic or electro-mechanical actuators/systems is intended to eliminate the need for extensive pneumatic and hydraulic networks [24, 25]. These could also enable the removal of engine air bleeds such that the engine design problem can be decoupled and optimized separately from that of the non-propulsive power subsystems.

The fact that many of these applications require a power conversion stage for control may seem cumbersome but actually can have net benefit. Distributed power converters enable flexibility in system design for redundancy and reduce constraints on the engine's electro-mechanical power conversion. Gearbox-less, variable-frequency electrical power generation from directly-driven main generators are now feasible [24, 25]. Electric starting

10
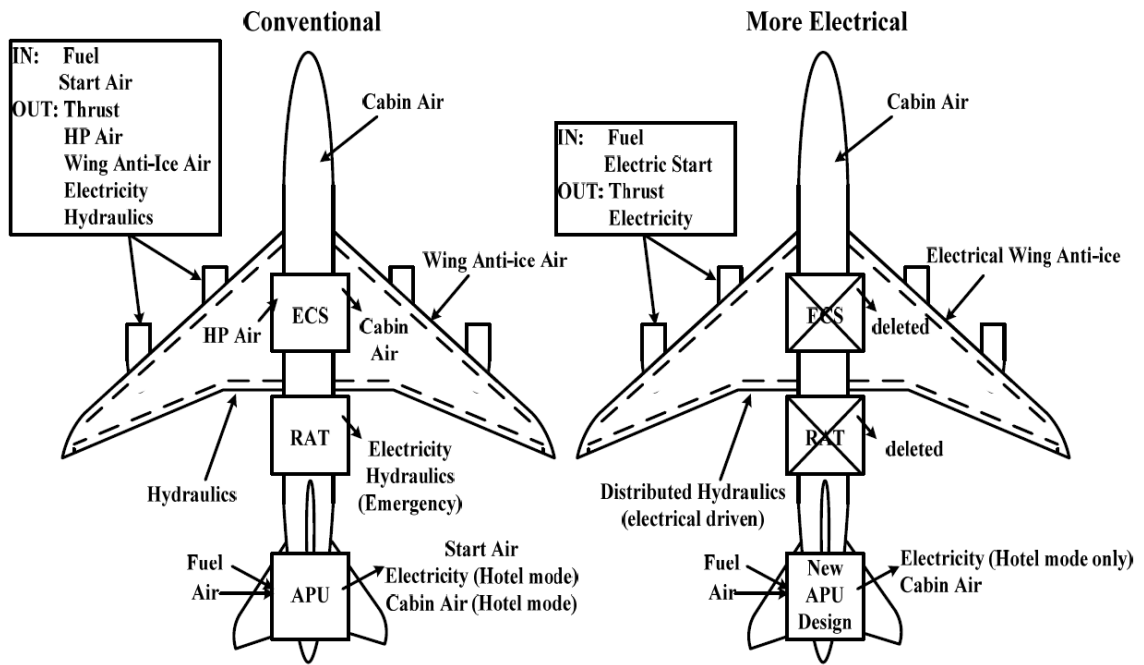
Figure 1.6: Comparison of conventional and "more electric" aircraft non-propulsive power generation equipment [8]

of the engine through the starter/generator such that accessory gearboxes can be eliminated and cold-weather starting power is reduced. This move also enables the auxiliary power unit (APU) to be fully converted to and optimized for electrical power generation [8, 25].

For example, the systems architecture of the Boeing 787 places significantly more emphasis on electrical systems than any prior aircraft. The 787 features a no-bleed engine with electrification of the wing deicing protection, engine starting, control surface hydraulics (partial, EHAs), and ECS. The starter/generators are also directly connected to the engine gearboxes and produce a variable frequency proportional to engine speed. Overall, the system architecture changes are predicted to account for 3% fuel savings, along with increased reliability, improved prognosis and diagnosis, and reduced maintenance costs [26]. Even with its vastly expanded electrical system, the Boeing 787's non-propulsive power is only a small percentage of its total system power – approximately 1 MW of non-propulsive power compared to 28 MW of propulsive power in cruise, considering a MTOW of 227 mt, L/D of 20 [27], and cruise speed of 250 m/s.

1.1.5 Turbofan Efficiency Limitations

A traditional aircraft used for civil aviation is equipped with one turbofan engine on each wing. A diagram of a turbofan engine is shown in Figure 1.7. The core of the engine consists of separate low- and high-pressure compressor, shaft, and turbine assemblies, referred to as spools, which are fluidly coupled. The compressor stages compress the air before fuel is injected and the mixture is combusted. The thermal efficiency of the core generally increases with increasing combustor temeprature and pressure. The exhaust gases are expanded through the turbine stages with some work being transmitted to the compressor stages through concentric shafts, or spools. Work is also done on the fan, which is mechanically

coupled to the low-pressure shaft either directly or through a gearbox. Turbofan engines employ a co-annular nozzle; the exhaust gases exit through the center, and the bypassed air, that which passes around the core, exits through the annular nozzle.
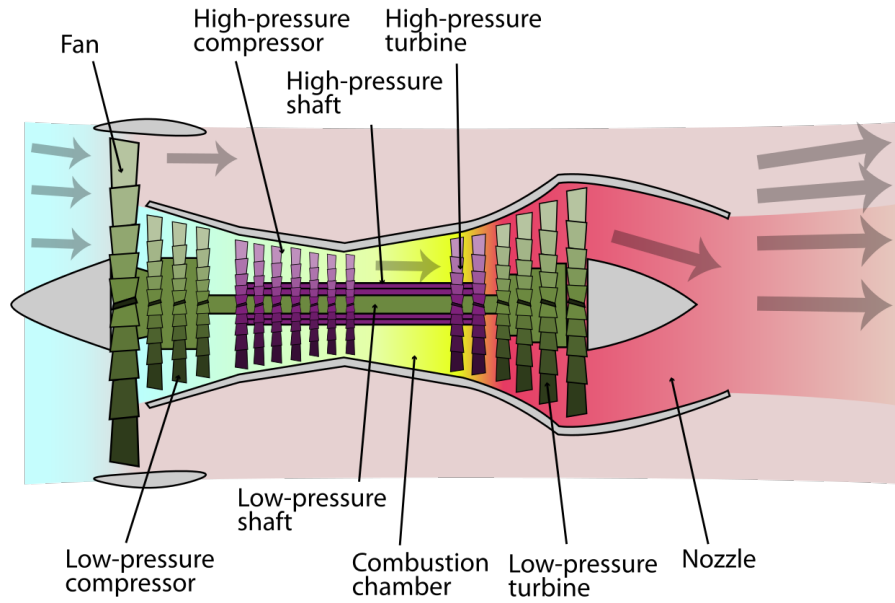
Figure 1.7: Schematic diagram illustrating the operation of a 2-spool, high-bypass turbofan engine, with LP spool in green and HP spool in purple. Copyright © 2008 K. Aainsqatsi

The ratio of air that bypasses the core to that of the air that passes through the core is called the bypass ratio (BPR). At a high level, the propulsive efficiency of the fan is related to the BPR and fan pressure ratio (FPR). Generally, the FPR is inversely proportional to the BPR, and propulsive efficiency increases with increasing BPR. The thrust output of a turbofan is described by

$$F = \text{BPR} \cdot \dot{m}_c V_b + \dot{m}_e V_e - \dot{m}_0 V_0 \tag{1.1}$$

where $\dot{m}$ and V are the mass flow rate and velocity, respectively, of air in the free (0), bypass (b), and core enter (c) and exit (e) streams, and the BPR is defined as $\dot{m}_b/\dot{m}_c$. A metric

more closely related to efficiency, the thrust-specific fuel consumption, defined as F/m_{fuel}, generally increases with increasing BPR. However, for the same core and fuel input with increased BPR, the kinetic energy in the core air stream would be negatively impacted.

There are practical limitations to further increasing the BPR of a turbofan engine. For the same shaft speed and increasing fan diameter, fan blade inertia (mechanical stress) and tip speed increase. When approaching supersonic tip speed, fan efficiency begins to decrease significantly. Further, the low-pressure spool achieves maximum efficiency at relatively high speeds compared to those required for peak fan efficiency. This divide becomes larger with increasing fan diameter. A gearbox could be added to the system but would negatively impact complexity, weight, and cost. The larger fan would require a larger nacelle, again increasing weight and cost, as well as drag. If the larger fan required more power to drive, additional stages could be added to the low-pressure spool, yet again increasing complexity, weight, and cost, or the core could be enlarged, which effectively reduces the BPR and also increases cost. Without electrification, further improvement is subject to the law of diminishing returns.

1.1.6 Electric Distributed Propulsion

The second methodology to reducing fuel consumption requires substantial technological development of the propulsion system and the aircraft body. Goals, such as those outlined by the International Civil Aviation Organization's (ICAO) Carbon Offsetting and Reduction Scheme for International Aviation (CORSIA) and the National Aeronautics and Space Administration's (NASA) Subsonic Fixed Wing (SFW) project (Table 1.3), are not projected to be met with the current rate of technological advances, as indicated by the International Air Transport Association (IATA) in Figure 1.8 and noted in [10, 28, 29, 30, 31].

14

Table 1.3: NASA SFW goals for the recent and future aircraft generations

Corners of Trade Space	N+1 (2015)* Tech. Benefits Rel. to Single Aisle Ref. Config.	N+2 (2020)* Tech. Benefits Rel. to Large Twin Aisle Ref. Config.	N+3 (2025)* Tech. Benefits
Noise reduction (cum. below stage 4)	32 dB	42 dB	71 dB
LTO NO_x reduction (below CAEP 6)	60%	75%	>75%
Block fuel burn reduction	33%**	50%**	>70%
Field length reduction	33%	50%	Exploit metroplex*** concepts

*Technology Readiness Level for key technologies = 4-6
**Additional gains may be possible through operational improvements
***Concepts that enable optimal use of runways at multiple airports within the metropolitan areas
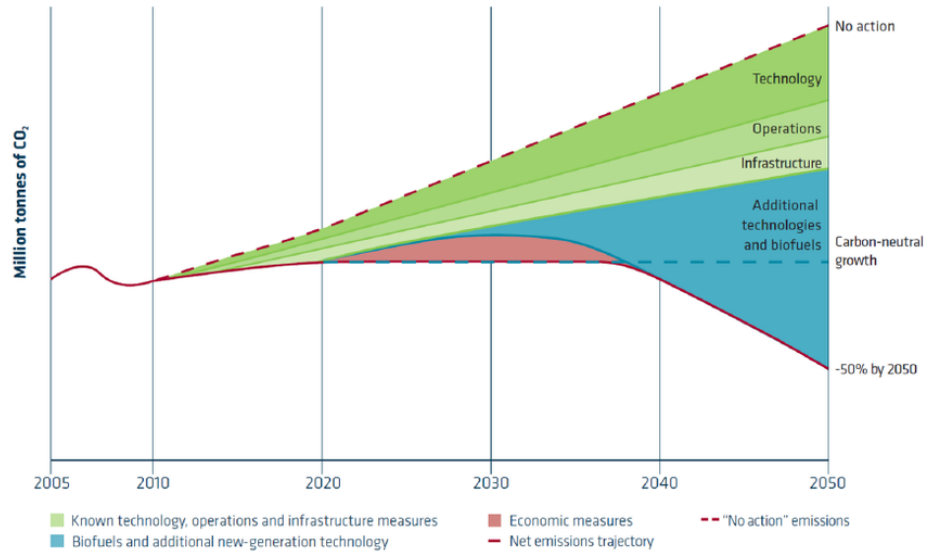
Figure 1.8: IATA's carbon neutral growth roadmap to meet CORSIA targets [9]

Electric distributed propulsion (EDP) is considered to be a disruptive technology, one that is a key enabler for reaching the aforementioned goals. Distributed propulsion alone is considered to encompass any propulsion system with a spanwise distribution of the propulsive thrust stream. There are many classifications for the related technologies and architectures, but the focus here is on propulsor sets, distributed across each wing and powered by an individual source, which will be referred to as the single-source, multi-propulsor (SSMP) architecture.

A benefit of the SSMP architecture, aerodynamic coupling of the propulsors to the airframe makes possible boundary layer ingestion (BLI) to increase propulsive efficiency and boundary layer control, thrust vectoring, and supercirculation to increase lift and reduce weight (removal of all control surfaces). Air-breathing engines are limited in these applications because they perform best in free stream inlet flow conditions. Thrust vectoring also

requires flexibility in propulsor location; this flexibility further enables airframe shielding to reduce community noise [29, 32]. The aerodynamic benefits were not exploited in this report's studies; thus, they will not be discussed further. They are mentioned because they served as significant motivation for early efforts developing distributed propulsion.

The primary benefit of the SSMP architecture leveraged here is the ability to independently optimize the engines' thermal efficiency (or that of any other power source) and the propulsors' propulsive efficiency. The highest BPR of a turbofan to-date is 12.5 for the Pratt & Whitney PW1100G installed on the Airbus A320neo, while SSMP concepts have attained effective BPRs (eBPRs) of between 15-30 [28, 30, 33, 34]. eBPR is used simply to represent that the flow through the fans does not explicitly "bypass" the engine.

The earliest designs of SSMP architectures transmitted (1) hot engine exhaust fluid to wing-embedded fans and (2) relatively cold fluid from the engine compressor stage to tip-driven propulsors. The fluid-powered propulsor designs were followed by multiple concepts utilizing mechanical coupling of the engine to adjacent fans. However, there are obvious limitations to extensive fluid networks and large numbers of mechanical connections as described previously. Following behind MEA initiatives, EDP systems, which distribute power electrically from a power source to propulsors, have become the most popular design for the following reasons:

1. Power sources can be any combination of electrical-power-producing devices, e.g. turbogenerators, batteries, fuel cells, etc.

2. Electrical distribution allows for a high degree of flexibility in component placement to take advantage of synergistic propulsor-airframe aerodynamics and makes use of MEA electric, non-propulsive power system development

17

3. Power inverters enable independent operation of electric machines to maximize system efficiency

4. Electric machines produce relatively low noise levels and quickly respond to torque commands

In simulation, NASA's N3-X turbo-electric, distributed-propulsion (TEDP) aircraft achieved 72% block fuel burn reduction compared to its baseline, the Boering 777-200LR. The N3-X is equipped with two turbogenerators (coupled turboshaft engine and generator, hence "turbo-electric"), 14 motor-driven fans, a hybrid wing body, and a liquid-hydrogen-cooled, superconducting electrical bus (Figure 1.9) [30].
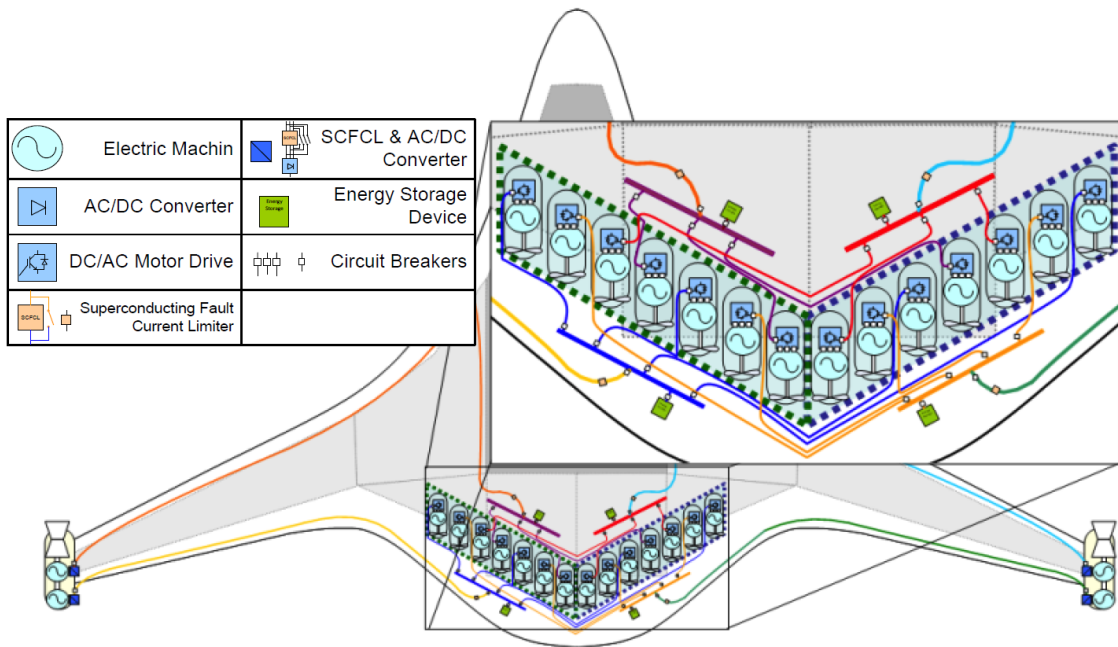
Figure 1.9: NASA's N3-X hybrid wing body, superconducting TEDP aircraft with detailed view of radial layout for electrical system [10]

1.2 Problem Statement

To enable fully sustainable aviation, fuel must be displaced with another form of energy storage that is sourced from renewables (Figure 1.10). Over the past 20 years, Lithium-ion batteries (LIBs) have been extensively researched and developed, but it is a relatively young technology with projections for significant advancement in the near-future. Battery energy storage systems (BESSs) have become commonplace in a variety of form factors and applications from Wh-scale mobile phone battery cells to kWh-scale hybrid-electric and fully-electric ground vehicle battery packs to MWh-scale ocean-going ship and stationary utility battery systems. Today, many LIB manufacturers are developing technology tailored to the aviation industry, as academia, industry, and the government have markedly increased the pace of battery-electric propulsion research and development, especially for drones, UAVs and urban mobility. To date, there have been limited studies in the space of regional aircraft, utilizing SOA (SOA) LIB technology in a series-parallel hybrid architecture. Further, the tools that had been used to perform related studies were not reported, unavailable, or would have required significant modification.

A hybrid-electric, distributed-propulsion (HEDP) regional aircraft was conceptualized as part of NASA's University Led Initiative (ULI) program "Electric Propulsion: Challenges and Opportunities." The control of the BESS significantly impacts overall energy efficiency, fuel burn (and emissions) reduction, thermal management system (TMS) design, electrical distribution system (EDS) design, installation and maintenance costs, and payback period, among others. Further, these impacts are uniquely influenced by the cell chemistry, BESS sizing, and mission range and profile.

In [35] a review of existing tools and approaches for hybrid-electric aircraft energy management showed it was common to assume a constant power split or rule-based strategy,
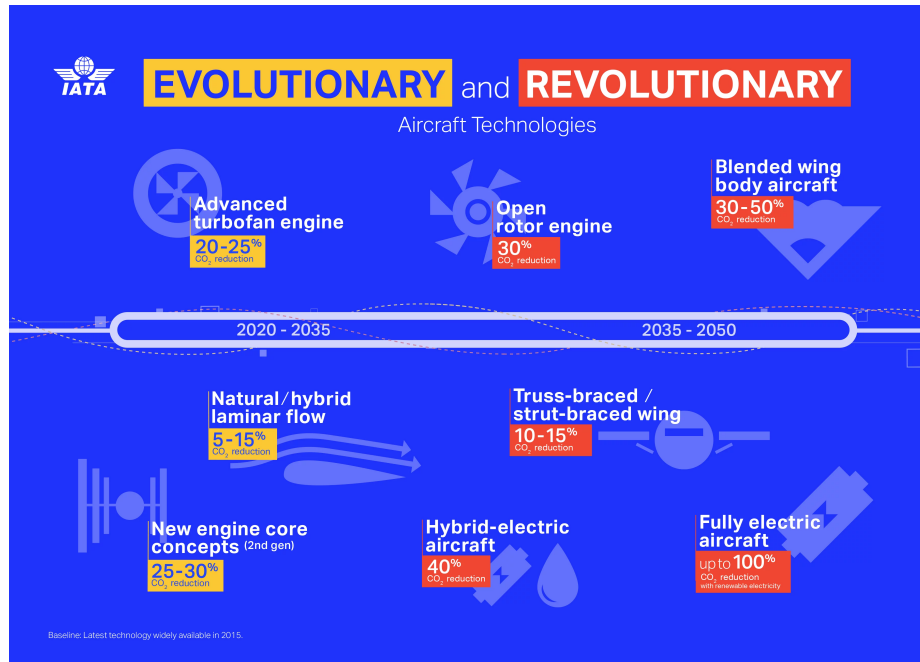
Figure 1.10: Evolutionary and revolutionary technologies to meet near- and far-term goals [9]

to optimize control/design over points of interest and neglect dependencies on past and future mission requirements and system states, and to neglect battery dynamics. In some cases, the split was constant throughout the mission; otherwise, the mission was divided into some small number of segments with unique rules. The proposed solution features a Model Predictive Control energy management optimizer within an outer design loop, such that the design and energy management could be co-optimized. Still, many more recent studies [36, 37, 38, 39] have been reported, in which the limitations identified by [35] persist.

In [40] the authors employed the tool proposed by [41] and reconsidered the optimization method, with its results instead supporting the validity of rudimentary energy management strategies. However, all of these studies considered parallel-hybrid configurations, likely due to its higher performance in automotive applications. Conversely, series-hybrid and

series/parallel-hybrid configurations (Figure 1.11) enable complete decoupling of the design of the conventional engine and electric propulsion system, and the losses associated with the additional energy conversion process are likely overcome by improvements in propulsive efficiency from increased BPR and added BLI.
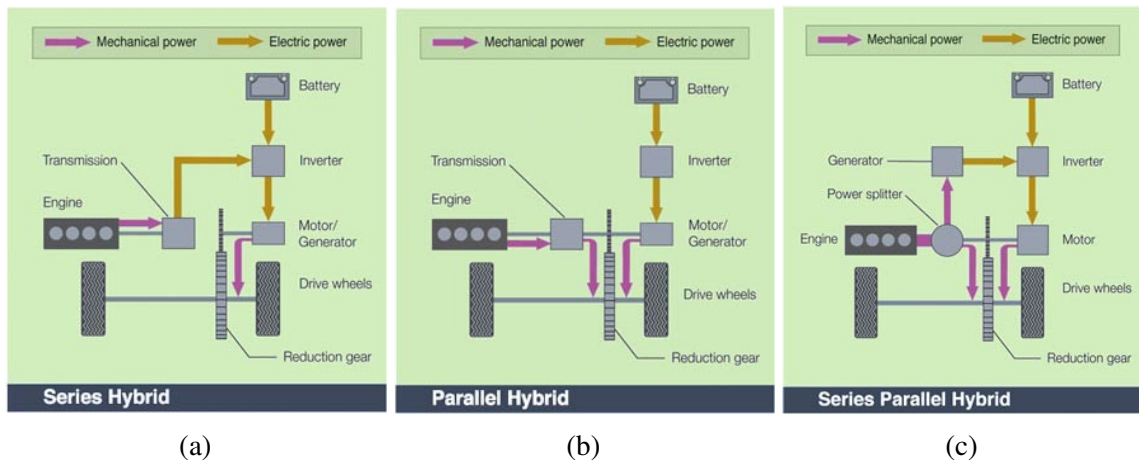
Figure 1.11: (a) Series, (b) parellel, and (c) series-parallel hybrid-electric vehicle configurations per automotive industry definition (Figure courtesy of CAAT)

Common optimization objectives for hybrid-electric vehicles (HEVs) such as minimizing fuel consumption, minimizing energy consumption, minimizing system weight, and minimizing total cost have a strong dependence on both the design and control of the system. The multi-objective optimization problem becomes increasingly challenging to solve both with increasing system complexity and increasing design variability. Dynamic programming (DP) is an optimization method that enables objective comparison of results from a large design space but requires reduced-order models (ROMs) to reduce computational time.

1.3   Objectives

This work presents a model-based design optimization of the BESS for a hybrid turboelectric generator for regional aircraft applications. The objective of this work is to optimally define the cell technology, BESS size, and energy management strategy that together minimize the fuel consumption of the aircraft, and investigate design trade-offs based on different flight missions. A reduced-order model and initialization process must be developed that results in negligible losses in accuracy relative to a proven tool, while enabling exploration of BESS design factors and coupling with an open-source DP algorithm. The ROM developed here will be validated against the NPSS-based Georgia Tech Hybrid Electric Aircraft Test-bed (GT-HEAT). SOA and future battery technology will be evaluated for feasibility in missions with range up to 1850 km. The optimal energy management strategy will be evaluated as a function of cell characteristics, BESS size, and mission range to deduce system-level implications and inform detailed design decisions.

1.4   Outline

The next chapter discusses opportunities and challenges of LIBs from the cell-level to system-level and examples of battery packs in aviation applications. Then, the system architecture and model architecture, calibration, and validation are detailed. The results chapter begins with an overview of dynamic programming, definition of HEV energy management problem, and analysis of the model and solver's convergence behavior. The chapter concludes with analysis of the impact of cell selection, battery energy storage system (BESS) sizing, and mission range on the energy management strategy and fuel savings. Finally, conclusions are discussed and future work is proposed.

Chapter 2: Lithium-ion Batteries

For the next 5-10 years, Li-ion is expected to remain the most capable commercially-available, rechargeable battery technology. Lithium has the lowest reduction potential of all elements, it is the third lightest element, and it has one of the smallest ionic radii of any singly-charged ion, resulting in high gravimetric and volumetric energy and power density [12]. Compared to common alternatives, Li-ion offers significantly higher energy density than lead-acid, does not suffer from the memory affect of Ni-Cd, operates at almost three times the voltage of Ni-based batteries, and has a low self-discharge rate [42].

Relative to jet fuel and jet engines, the performance of Li-ion is still quite limited. Jet fuel has gravimetric and volumetric energy density of 12,000 Wh/kg and 9,600 Wh/L, respectively, while SOA Li-ion technology has yet to achieve 300 Wh/kg and 1,000 Wh/L. While the efficiency of jet engines is limited, they are a mature technology, with proven performance in extreme conditions and economic feasibility in the global marketplace. Materials used in LIBs present instabilities that lead to mechanical and chemical degradation with use and time. Degradation in LIBs is a highly active area of research.

Cyclability and safety largely depend on the application and system integration. Li-ion has performed sufficiently well in these metrics to become commonplace in applications ranging from mW-scale power and Wh-scale energy to MW-scale power and GWh-scale energy. Generally, the technology is highly scalable and widely feasible. However, aircraft

are somewhat of a "last frontier" for LIB technology, due to the high impact of added weight and more stringent safety requirements.

2.1   Cell-Level Overview

Metrics such as energy density, power density, capacity, rate capability, cyclability, safety, and abuse tolerance are generally referenced to assess the performance of battery cells [43]. For a given cell, removable energy and capacity can vary depending on rate, temperature, and state of health (SOH), while power capability can vary by mode (charge/discharge), state of charge (SOC), temperature, and SOH. SOC is an estimate of the ratio of charge stored in the battery, and SOH is an estimate of the ratio of performance remaining in the battery; generally, charge can be restored but performance cannot. For a given cell, SOH depends both on cycling and calendar aging, the former depending on the characteristics and frequency of discharge/charge cycles and the latter depending on storage conditions, primarily duration, SOC, and temperature [44]. Cyclability is a qualitative measure of the cell's tolerance for high-rate charge and discharge and for wide-ranging SOC and temperature. The SOH is also impacted by instances of abuse and tolerance for abuse. Mechanical abuse includes vibration, impact, penetration, and water immersion; thermal abuse includes operation at extreme temperatures, high and low; and electrical abuse includes elevated rates, short circuit, over-charge, and over-discharge.

A Li-ion cell consists of a cathode (positive electrode), anode (negative electrode), separator (porous membrane), and liquid electrolyte. The separator prevents the electrodes from physically contacting but must be porous such that lithium ions can be exchanged between the electrodes through the electrolyte. In discharge, electrons move from the anode

to cathode through an external circuit (load), while lithium ions move from the anode to cathode via the electrolyte (Figure 2.1), and vice-versa in charge.
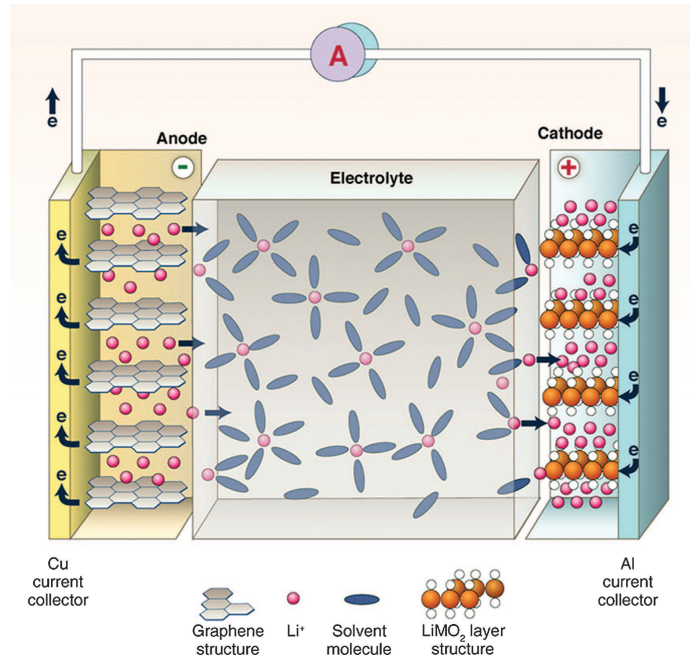
Figure 2.1: Schematic of a lithium-ion battery in discharge (no separator shown) [11]

The energy storage capability of a LIB is dependent on its charge acceptance and potential, which are related to crystalline structure and Gibbs free energy, respectively, of the active material. Figure 2.2 compares these values for all common electrode materials. SOA LIBs feature intercalation cathodes (Figure 2.2a and anodes (graphite and LTO, Figure 2.2c). An intercalation electrode is a solid host network into and from which guest ions can be inserted (lithiation) and removed (delithiation) reversibly, whereas, in conversion electrodes, the crystalline structure physically changes during lithiation and delithiation [12]. Conversion cathodes and anodes are a highly active area of research for their high

theoretical capacity; however, several practical issues related to cyclability and aging are currently delaying their commercial deployment.

(a) Intercalation cathodes (b) Conversion cathodes

(c) All anode types (d) All electrode types
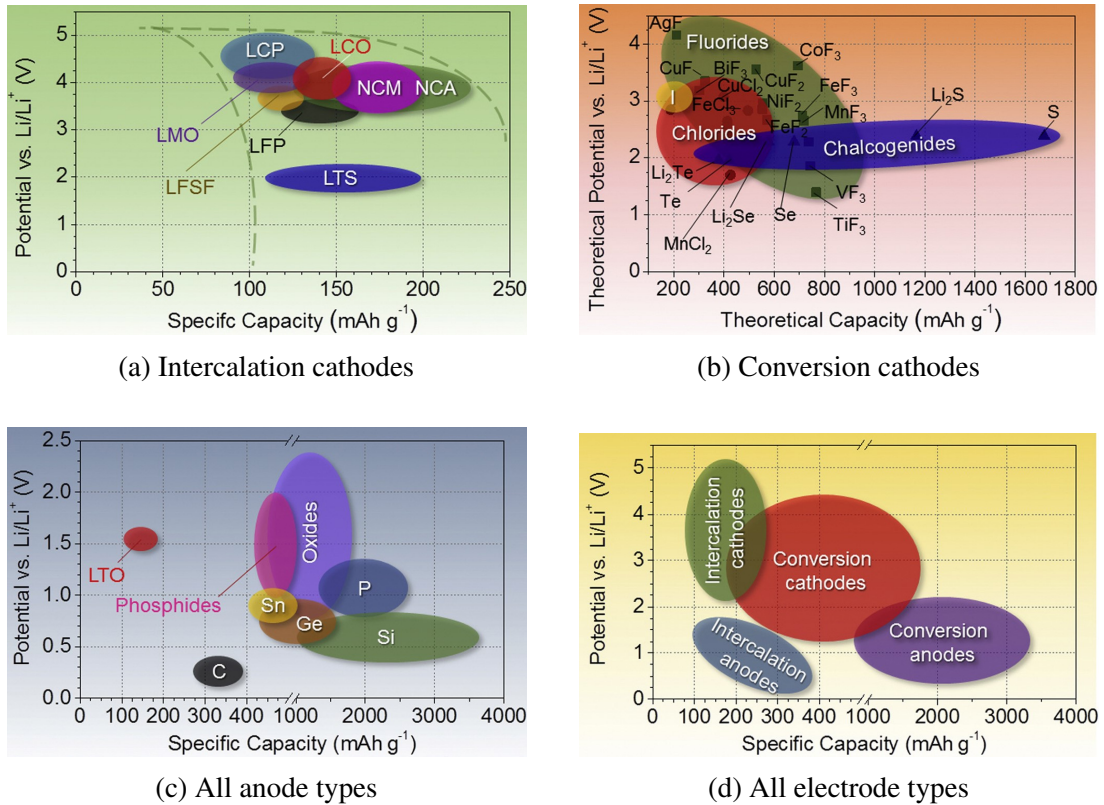
Figure 2.2: Approximate range of average discharge potentials and specific capacity of common electrode materials [12]

2.1.1 Materials

The most common cathode materials are based on lithiated transition metal oxides and include $LiCoO_2$ (LCO), $LiMn_2O_4$ (LMO) $LiNiCoAlO_2$ (NCA), and $LiNiMnCoO_2$ (NMC), and $LiFePO_4$ (LFP). LCO and LFP are most widely used in commercial Li-ion batteries.

LCO was used in the first commercialized LIB (1991) and, thus, offers the greatest technological maturity. It features moderate specific capacity (140 mAh/g), moderate power capability, and moderate cyclability (500-1000 cycles) but is limited by low thermal stability and high cobalt content [12, 42, 45]. Regarding lithium metal oxides, thermal stability indicates the relative temperature at which oxygen is released exothermically, which can lead to a thermal runaway reaction and explosion. LCO has the lowest thermal stability of any commercial cathode material and can experience thermal runaway at temperatures as low as 150 °C [12]. Cobalt is highly toxic, presenting concerns at beginning- and end-of-life processes, and cobalt reserves are relatively limited.

LMO was first used in a commercial LIB in 1996. Its specific capacity is lower (120 mAh/g) but specific power is higher compared to LCO. Manganese is more abundant and less toxic than cobalt, and manganese oxide has high thermal stability, with thermal runaway occurring around 250 °C [45]. LMO is not widely used because of its poor cyclability (300-700 cycles). In "typical" charging conditions but especially at elevated temperature (40-70 °C), the cathode structure degrades and active material is lost, causing capacity and power fade [12].

LFP was also first commercialized in 1999. LFP offers the highest power density but moderate specific capacity (135 Ah/g). Its energy storage capability suffers further from a relatively low potential, resulting in the one of the lowest energy densities of LIBs. Though the potential is low, LFP batteries feature a relatively flat (constant voltage) discharge curve, which enables consistent performance across a wide SOC range (15-100%). LFP batteries have low cost and toxicity, high power capability, high cycle life (>2000 cycles), and high thermal stability (thermal runaway around 270 °C) [45].

NCA was commercialized in 1999, as a replacement of LCO. Nickel was initially considered as a substitute for cobalt, i.e. $LiNiO_2$, but the addition of cobalt and aluminum was required to improve performance [12]. Still, the cost share of cobalt was significantly reduced to 3-6% in NCA (and NCM), compared to 21% in LCO cells [45]. NCA offers high specific capacity (200 mAh/g), moderate-to-high specific power, and high cycle (1000-1500 cycles) and calendar life but has similar thermal stability to LCO [12, 45].

Though NMC was commercialized most recently, in 2004, it is the most common chemistry used in HEVs and EVs. Generally, NMC has lower specific capacity (175 mAh/g) and higher cycle life (1000-2000 cycles) than NCA, but the proportions of nickel, manganese, and cobalt can be varied to achieve desired performance attributes. Nickel increases lithium extraction capacity and specific energy, manganese increases power capability and thermal stability, and cobalt increases the structural stability and cyclability [12, 45].

When examining next-generation cathode technologies, sulfur is a conversion material that appears the most promising for early commercialization and deployment. It has the highest theoretical capacity (1675 mAh/g) of known cathode materials and is cheap, abundant, and non-toxic. However, it is inhibited by low electronic conductivity, low theoretical potential, high volume expansion (80%), non-monotonic discharge curve, high voltage hysteresis, and high solubility in traditional electrolytes [12]. The low theoretical potential requires that a highly electronegative compound be used as the anode such that energy storage capability is not sacrificed. The high volume expansion can destroy electrical contact within the cell and induce significant mechanical stress. The non-monotonic discharge curve and high voltage hysteresis present challenges for conventional SOC estimation techniques. Sulfur cathodes have low rates of calendar aging but suffer from poor cycling aging. Cathode active material, in the form of intermediate reaction products (polysulfides), is continuously

dissolved and lost in cycling; the loss is irreversible when a highly electronegative element (or compound) such as metallic lithium serves as the anode [12, 46, 47]. Further loss of active material, along with decreases in surface conductivity, are attributed to growth of a passivation layer comprised of final discharge products Li_2S_2/Li_2S [46, 47].

Cyclability, charging rate, and energy density are most significantly influenced by the anode composition. Most LIBs feature a graphitic (layered-structure) carbon anode because of its low cost, high reversibility of lithiation and delithiation, and small volume variation (10%) [42]. Because the theoretical capacity (372 mAh/g) of graphitic carbon is being approached, non-graphitic and non-carbon anode compounds are required to meet demand for improved performance. Non-graphitic carbon exhibits nearly double the theoretical specific capacity but suffers from high early-cycle irreversible capacity loss [12, 42].

Silicon is considered to be one of the most promising non-carbon anode materials. Similar to sulfur, silicon exhibits high specific capacity (up to 4200 mAh/g), low cost, high abundance, and low toxicity. Silicon is capable of reversibly alloying and de-alloying with lithium at room temperature; however, the alloying/de-alloying process causes huge volumetric expansion (up to 300%) [12, 42, 46]. This process also occurs at low potential, which is ideal for the overall cell potential but also for solid-electrolyte interphase layer formation. During cycling, the large volume change destroys the SEI layer and results in continuous electrolyte decomposition, loss of lithium, and increasing impedance [12]. Cyclability of cells with silicon anodes is limited at present, when compared against commercial, graphite-based anodes.

2.2 Modeling Methods

An accurate battery model is the basis for the sizing and design of a battery energy storage system, for definition of optimal control policies. There are two common categories of models: electrochemical models and equivalent circuit models (ECMs). Figure 2.3 shows a notional voltage response to a current pulse and indicates the influence of model-specific parameters.
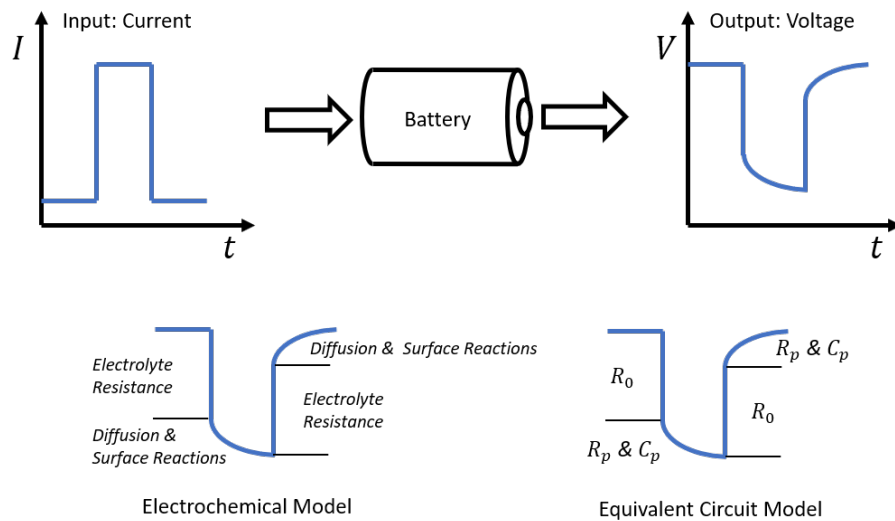
Figure 2.3: Influence of model-specific parameters on voltage response to discharge current pulse [13]

Electrochemical models rely on "first principles," e.g. Fick's law of diffusion for lithium concentrations and Ohm's law for potentials, to describe the transport, thermodynamic, and kinetic phenomena throughout the cell, resulting in a set of coupled, non-linear partial differential equations [13, 14]. Electrochemical models can be used to observe internal states that are otherwise unmeasurable, to evaluate sensitivity to design parameters in simulation,

and to test the accuracy of ROMs [13]. However, memory and computing requirements are large, not only for model evaluation but typically also for parameter identification. Thus, these models are impractical for high-dimensional design and control optimization problems and in real-time state estimation applications.

Based on Thevenin's theorem, ECMs model batteries as a voltage source and network of resistors and capacitors. This modeling technique reflects battery performance macroscopically and, therefore, is highly adaptable. The same model structure can be used to represent different batteries and types with the same accuracy using appropriate parameter values. Further, the same parameters can have added dependencies to capture environmental and aging effects [48]. Complexity can easily be added to the model structure to more accurately replicate battery performance, with increased computational cost but perhaps better suited to a specific application.

2.2.1 Equivalent Circuit Models

ECMs are particularly attractive due to their simplicity, computational speed, and flexibility in capturing voltage dynamics, heat generation, and aging characteristics [49]. A source or load prescribes the overall current into or out of the battery. The voltage source is considered as the OCV of the battery. The OCV and nominal capacity of the cell comprise the static part of the model. At a minimum, a single resistor in series represents the model dynamics but additional parallel networks of resistors and capacitors are commonly included to better capture the transport, thermodynamic, and kinetic aspects [50].

Figure 2.4 shows the circuit diagrams for the most common variations of an ECM. There is no limit on the number of RC networks, or order of the model, but no more than two are

(a) Rint (zeroth order)   (b) Thevenin (first order)   (c) Dual polarization (second order)
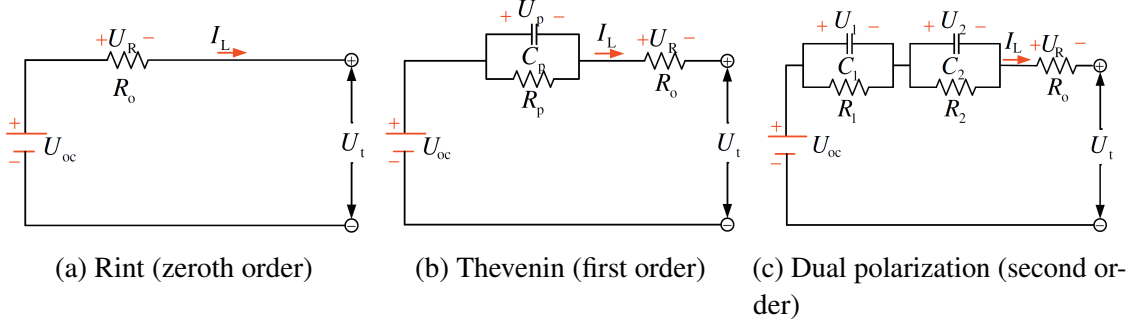
Figure 2.4: Schematic diagram of equivalent battery circuit models [14]

typically necessary to accurately capture the polarization characteristics, i.e. the nonlinear regions in Figure 2.3. The model equations for each circuit shown can be written as

$$\text{Zeroth-order:} \quad U_t = U_{oc} - I_L R_0 \tag{2.1}$$

$$\text{First-order:} \quad \dot{U}_p = \frac{I_L}{C_p} - \frac{U_p}{R_p C_p} \tag{2.2}$$

$$U_t = U_{oc} - U_p - I_L R_0$$

$$\text{Second-order:} \quad \dot{U}_1 = \frac{I_L}{C_1} - \frac{U_1}{R_1 C_1}$$

$$\dot{U}_2 = \frac{I_L}{C_2} - \frac{U_2}{R_2 C_2} \tag{2.3}$$

$$U_t = U_{oc} - U_1 - U_2 - I_L R_0$$

where U_t is the terminal voltage, I_L is the load current, R_0 is the ohmic resistance, U_{oc} is the open-circuit voltage, and $R_{p,1,2,...}$ and $C_{p,1,2,...}$ are the effective resistance and capacitance values, respectively, used to model the polarization characteristic [14].

This approach is relatively simple mathematically and numerically such that complicated and intensive computation is minimized or even avoided [50]. Further, cell performance is commonly extrapolated to the pack level for system simulation, design, and control applications. It is assumed that the cells are equal and that there is no temperature gradient

32

between them that could induce significant cell-to-cell imbalances in voltage or charge such that the battery pack behavior can be scaled from that predicted by a model for an individual cell [51].

In [14, 48], the performance of different order ECMs was compared. Accuracy of ECMs generally improves with increasing model order, but model performance ultimately depends on the parameter identification process. If the experimental data is overfit, the model will perform increasingly poorly as cycle characteristics increasingly differ from those of the data used for parameter identification.

2.2.2   Parameter Identification

ECMs are typically developed starting from test data, as model parameters do not explicitly depend on the cell's physical design or states. An identification procedure contains three main parts: (1) model structure selection, (2) experimental tests design and, (3) fitness criterion and identification error minimization algorithm selection.

Model parameters are identified from experimental test data during which a battery cell is generally kept in a thermal chamber and connected to a cell cycler (programmable load/-supply). The thermal chamber maintains a constant temperature, and current measurements from the cycler enable couloumb counting for accurate evaluation of the battery SOC, both of which are necessary because parameters are highly SOC- and temperature-dependent.

SOC is evaluated from the capacity added to or removed from the cell and the cell's real capacity. Thus, typically, testing begins with an individual capacity test or series of them. The capacity is highly dependent on the rate, as well as the temperature, and it even varies between samples of the same cell model. Capacity is measured using coulomb counting in a constant rate discharge and/or charge test. Low-rate ($<=C/3$) is used to measure the fully

33

usable capacity, but the reference nominal capacity used in the model can vary by application being studied. Low-rate, constant-current cycles can be also be used to approximate the OCV of the cell; more often, the OCV is measured at the end of long rest periods in dynamic tests.

A standard dynamic test is the HPPC test, shown in Figure 2.5. The parameters introduced in Section 2.2.1 are calibrated considering the experimental data from a HPPC test, or similar dynamic profile. Pulse power tests are segmented by incremental changes in SOC. High-power, short-duration pulses enable the assumption of constant SOC, and consequently constant parameters, while also generating sufficient dynamic behavior from which to estimate parameter values, both in charge and discharge. A short rest period intercedes discharge and charge pulses. A long rest between SOC steps enables the battery to reach electrochemical and thermal equilibrium, at which the OCV can be measured. Generally, these parameters are not considered to be highly influenced by the pulse rate. Standards for static and dynamic tests are outlined in [52].

In the last part of the identification process, the model's parameters are determined, generally with the objective of reducing error between experimental data and model output and with care to not overfit the data. Given the nominal capacity from a capacity test, the SOC is tracked via coulomb counting and updated at time index $t + \Delta t$ from

$$\text{SOC}(t + \Delta t) = \text{SOC}(t) - \frac{I_L(t)}{C_{nom}} \tag{2.4}$$

where C_{nom} is the nominal capacity. With the battery fully charged and then at each SOC increment k, when the battery has reached equilibrium (after a long rest, 30+ min.) and while under no load, the terminal voltage is closely representative of the OCV:
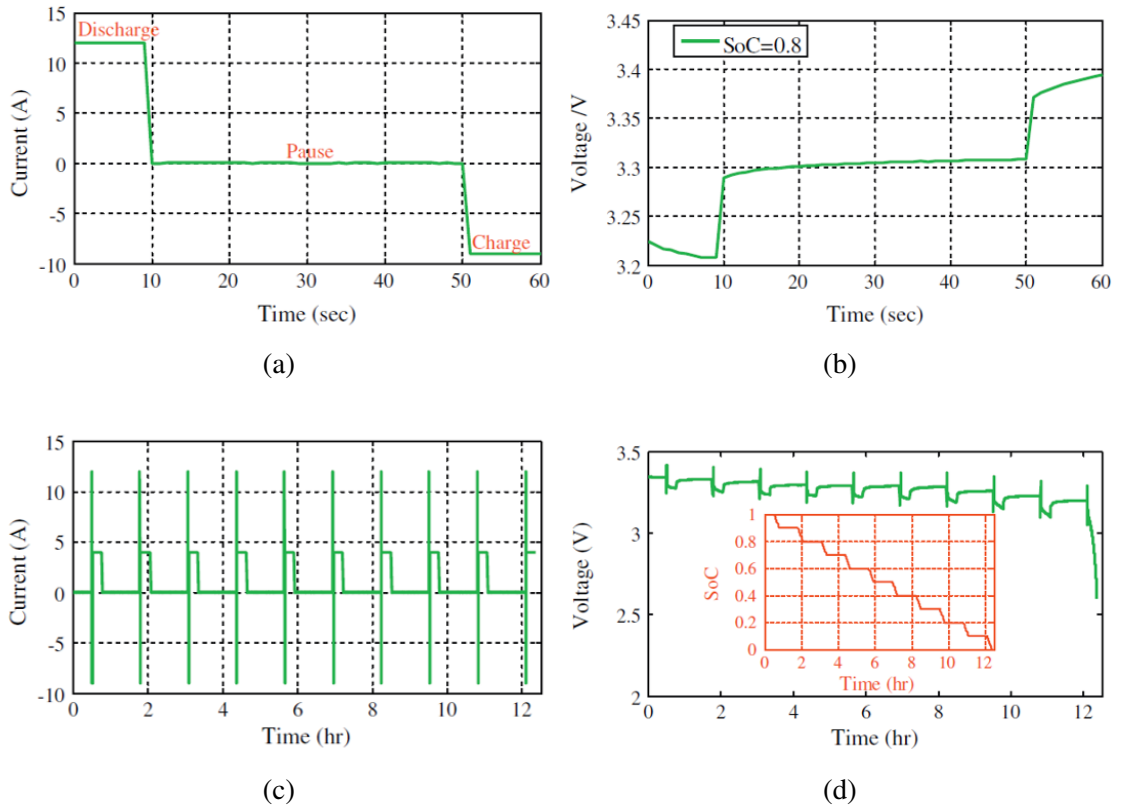
Figure 2.5: (a) The pulse profile and (b) the cell's voltage response at 80% SOC, (c) the full HPPC test cycle and (d) the cell's voltage response and SOC [14]

$$U_{oc}(\text{SOC}_k) = U_t(t) \tag{2.5}$$

The ohmic resistance is calculated from the immediate voltage change before and after the start of a discharge or charge pulse is applied. If using the zeroth-order model, this estimate of terminal voltage will be optimistic because current is applied for some duration greater than the datalogging frequency. A more conservative model can reference the terminal voltage at the end of the pulse, underestimating terminal voltage in pulses with duration less than that of the test and overestimating terminal voltage otherwise. Consider that the pulse is applied at time $t + \Delta t$ and ended at T, the ohmic resistance can be computed generally from

$$R_0(\text{SOC}_k) = \frac{U_t(t) \pm U_t(t + \Delta t, ..., T)}{I_L(t + \Delta t, ..., T)} \tag{2.6}$$

Referencing the terminal voltage at time past $t + \Delta t$ results in a higher estimate of ohmic resistance; however, in ECMs with RC networks, time $t + \Delta t$ is always used to define the ohmic resistance. A minimization algorithm is typically employed to determine the values of the equivalent resistance and capacitance of the RC networks that maximize accuracy, or minimize root mean square error (RMSE). More specifically, the time constant of the network is identified, where $\tau_i = R_i \dot{C}_i \; \forall i = 1, 2, ..., n$, and the parameter values are determined through regression [13, 53, 54, 55]. Initial estimates of the parameters are widely available in literature.

At a minimum, battery voltage, current, power, and SOC limits must be enforced. Voltage and current limits are reported by cell manufacturers. SOC is defined as having limits between 100-0%, but that window can be narrowed depending on the desired performance.

To some extent, current limits can be manipulated as well. Then, there are a few methods for defining peak power limits: PNGV HPPC, SOC-limited, and voltage-limited methods.

The PNGV HPPC method developed by Idaho National Engineering and Environmental Laboratory estimates the peak power of a battery based on the zeroth-order model [52]. The peak charge and discharge current are limited by the design limits of the cell. This method can be used for calculating the absolute available peak power of the battery. It is both advantaged and disadvantaged by the ability to compute the power limits *a priori*. It reduces model complexity and computational cost, but it is not suitable for estimating the continuous available peak power with knowledge of the time step. This method provides the best compromise between complexity and accuracy.

All testing generally involves a test matrix including multiple samples, rates, and temperatures. The end-user should consider the application to determine which rate and temperature is most appropriate or if multiple need to be evaluated. At a minimum, parameters are solely functions of SOC. The most complex ECMs consider each parameter to be dependent on SOC, temperature, current, and SOH. The parameters are often stored in lookup tables and interpolated and extrapolated linearly. Note that, while each of these values may be known exactly in a modeling environment, it is infeasible to have measures of each in a practical application. In fact, all of these parameters must be estimated in a real battery system.

2.3 System Integration

In the context of system integration of energy storage devices, batteries are often referred to as cells, modules, and packs. Cells are connected in series, parallel, and mixed configurations to form a module. Connection in series increases the module voltage, and connection in parallel increases the module capacity. The number of connections and configuration of

the module can be limited by mass, volume, voltage, or monitoring capability. Typically each module includes components of the battery management system (BMS) and thermal management system (TMS) but full functionality requires assembly of the entire battery pack. The battery pack encompasses all modules, connected in series and/or parallel, and their interconnections, low-voltage electrical, high-voltage electrical, and thermal. The battery pack configuration is still limited by mass, volume, voltage, and monitoring capability, but also is additionally constrained by the prescribed module design.

Cell formats common in HEVs and EVs include cylindrical with spirally-wound active material, prismatic with elliptically-wound active material, and pouch with stacked plates of active material, as shown in Figure 2.6. Aluminum and stainless steel are usually used for cylindrical or prismatic cell casing, which adds mechanical strength, while the pouch cell uses soft packaging, which is usually a metallized film. The cylindrical cells are named in accordance to their diameter and height, e.g. 18650 implies 18 mm diameter and 65.0 mm height. Similarly, names of prismatic and pouch cells often include their length, width and height. The cell form factor, which includes its size, directly influences both the packaging density and cooling configuration.

Small and large size cells exist in all formats. The voltage cannot be scaled at the cell level, but the capacity increases with increasing active material area. Cylindrical cells are most often low capacity and small size, i.e. < 4 Ah and 40 cm^3, while prismatic and pouch cells are commonly high capacity and large size, i.e. > 10 Ah and 100 cm^3. While larger format cells of the same chemistry typically offer greater energy and power density, as cell size increases, flexibility in module and pack design decreases. Manufacturing of small cells is more consistent and lower cost [56]. For the same energy and power capability using small cells, more cells and, consequently, more electrical connections are required.
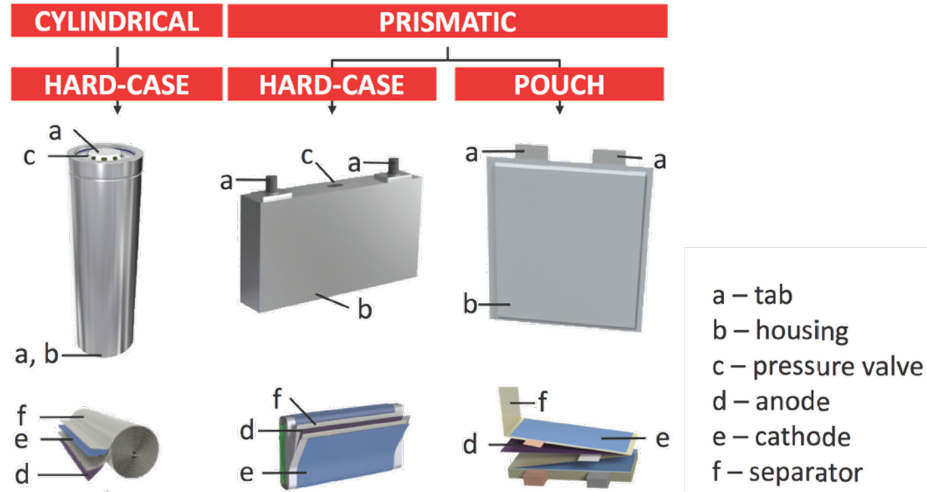
Figure 2.6: Common cell formats in HEV applications [15]

Welded connections are preferred for lower contact resistance, lower weight, and better heat dissipation but significantly reduce serviceability. Larger cells can be used to reduce part count and assembly costs, but more localized energy content and less redundancy increases the risks associated with failure of an individual part, whether a cell, interconnect, monitoring device, etc.

The ideal operating temperature of Li-ion battery is between 15-35 °C. The three processes that determine the temperature of the cell are heat generation, heat transport, and heat dissipation. Irreversible heat generation, i.e. joule heating, is responsible for the majority (>90%) of internal heat generation in LIBs, and there is local heating near tabs due to electrical contact resistance and current concentration [57]. Localized heating and resulting temperature gradients are exacerbated by low thermal conductivity of battery materials. Heat dissipation is heavily influenced by the form factor of the cell.

The heat exchange surface area to volume ratio determines the heat dissipation rate; the higher the ratio, the higher the heat transfer ability [56, 57]. A cylindrical (D: 38 mm, H:

120 mm), prismatic (W: 65 mm, H: 140 mm, T: 18 mm), and pouch (W: 73 mm, H: 163 mm, T: 11 mm) were characterized as having heat exchange surface area to volume ratios of 105 m^{-1}, 156 m^{-1}, and 228 m^{-1}, respectively [56]. A large base area and controllable thickness is preferred to minimize thermal resistance, as thermal conductivity is typically an order of magnitude greater in the direction parallel to the active material layers [56, 57].

Temperature variation within a cell should be kept between 5-10 °C. Figure 2.7 shows the temperature gradient of a 35 Ah, NMC, pouch cell (W: 169 mm, H: 179 mm, T: 14 mm), resulting from two different cooling techniques [16]. While there is local heating at the tabs, the tabs also serve as an effective thermal pathway, particularly that of the anode (bottom) which is made of copper. The comparison of two cooling methods highlights that enhancing thermal boundary conditions can lower the average battery temperature but also enlarge temperature gradients [57].

Consider next that the same cooling fluid used to cool the cell pictured in Figure 2.7 has a temperature gradient itself and does not absorb heat equally throughout the module or pack. Large temperature gradients result in varied cell performance and cell imbalance, and these differences persist due to different rates of aging. Without accurate thermal modeling and SOH estimation, temperature gradients could cause pre-mature aging and unexpected failure of a cell. The variation of temperature across the battery pack should be kept within 3-5 °C [56].

The safety issues associated with LIBs typically arise under abnormal abuse conditions. These abuse conditions include mechanical abuse behaviors (crush, nail penetration, drop, and vibration), electrochemical abuse behaviors (overcharge, over-discharge, short circuit, and gas generation) and thermal abuse (external heating). Generally, the safety issues mentioned above often occur synchronously. For example, overcharge is usually associated
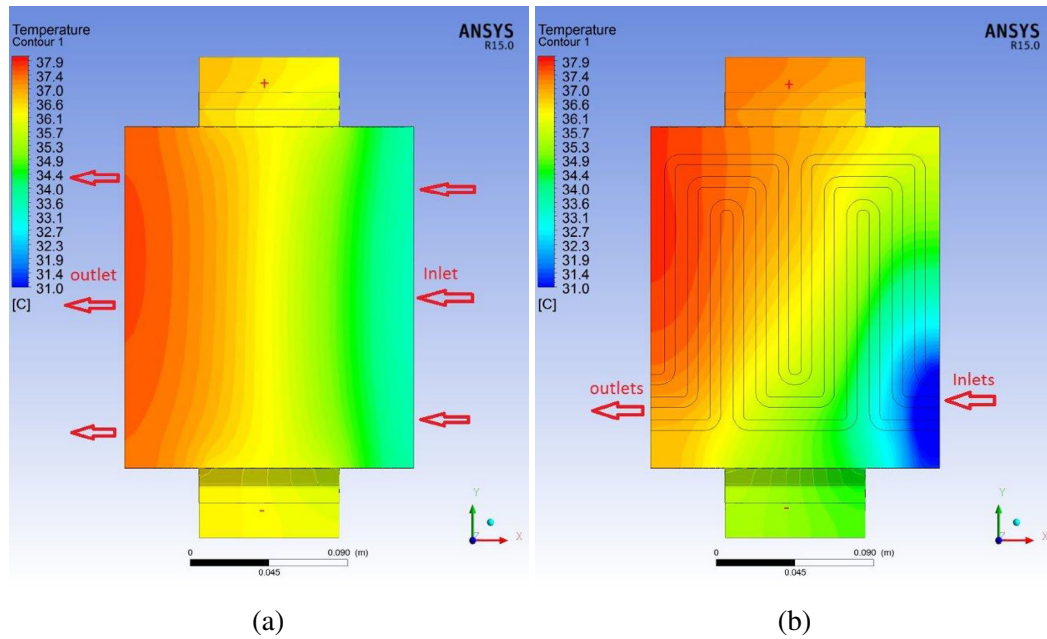
Figure 2.7: Temperature distribution across pouch cell surface using (a) forced air and (b) liquid cooling jacket [16]

with thermal runaway (high temperature), gas generation (high pressure), and short circuits (high current) [11]. Safety can be addressed at three levels: materials, cell, and system.

The first depends on the inherent safety of battery materials, including the active material, discussed in Section 2.1, and the separator and electrolyte compositions [42, 45]. At the cell level, safety elements and features can be integrated. Cylindrical and prismatic cells have a structural casing that is somewhat resistant to mechanical abuse and able to withstand pressure buildup and also feature a vent extreme pressure [45, 56]. Pouch cells are vulnerable to these risks, and, in fact, compressive forces must be applied to a pouch cell through an external structure to maintain performance in standard operation [56]. Most cells are equipped with a separator that has a "shut down" function. Lastly, the main purpose of the BMS is to ensure safe operation of the battery.

41

The BMS protects the cell against electrochemical and thermal abuse. More specifically, it fulfills the following functions:

- Charge and discharge control

- Charge balancing (equalization)

- Current and voltage monitoring

- Temperature monitoring and control

- Fault diagnosis and system configuration control

Charge and discharge control prevents overcharge and over-discharge and, ideally, optimizes the energy management strategy for a single or group of objective(s) such as minimizing fuel consumption and emissions, minimizing degradation, and/or maximizing vehicle range, etc. Charge balancing (Figure 2.8) is the process of continuously maintenance of and/or periodically restoration to equal charge in all cells to maximize performance. Even slight differences in internal resistance and capacity, which are inevitable, create imbalance, which increases degradation of the weakest cell(s). A balanced pack has cells with equivalent capacity stored and minimal voltage variation (<=50 mV), with capacity limited by the weakest cell and with the weakest cell generally exhibiting the lowest voltage [56].

Current, voltage, and temperature monitoring are necessary for charge and discharge control, fault diagnosis, and state estimation. Fault diagnosis could pertain to a failure mode of the cell such as short circuit, which can only be identified through measurement, or failure of another sensor, assuming there is sufficient redundancy in the datalogging system. Battery states cannot be measured and, consequently, must be estimated using current, voltage, and temperature measurements. Typically, measuring each of these values for every individual
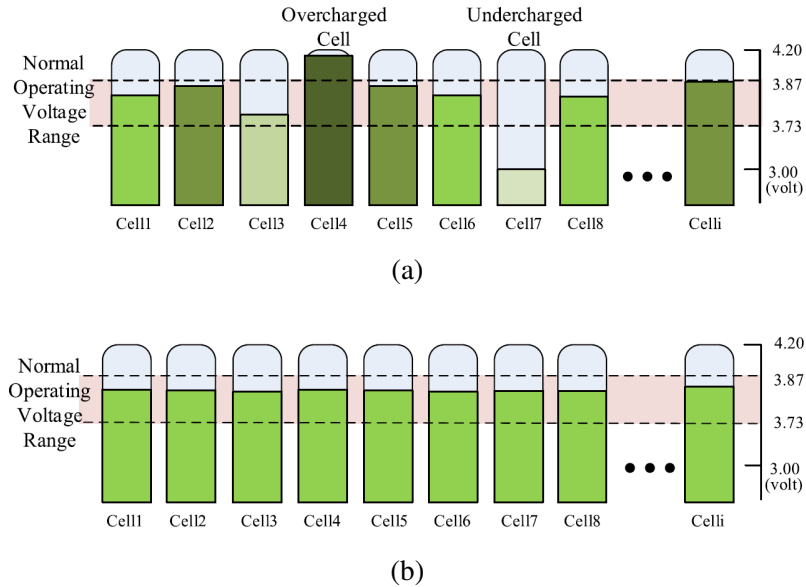
Figure 2.8: Notional example of charge (a) imbalance and (b) balance within a module or pack [17]

cell is cost prohibitive, further increasing the complexity of state estimation [17]. The BMS communicates with the TMS to control battery temperature and generally avoid operation at extreme temperatures. Charging at high SOC, high rate, and low temperature (<10 °C) causes lithium plating on the anode, which can form lithium dendrites that puncture the separator and short circuit the cell. Prolonged periods of time spent at high SOC and high temperature (>60°C) can lead to thermal runaway [56].

Two failure events of non-critical battery systems on-board the Boeing 787 Dreamliner resulted in the indefinite grounding of all 787 aircraft and huge financial losses for Boeing and its suppliers, but the root-cause was never determined [58]. The NASA X-57 Maxwell project highlights the focus on safety with respect to LIBs in aerospace applications. Aerospace demands high gravimetric energy density, but the use of lighter, more energetic cells also carries greater risk. Containment of gases and particulates requires a closed system

and increased packaging weight, e.g. the target for eVTOL application is 30% packaging overhead. The X-57 battery module, shown in Figure 2.9, uses an aluminum honeycomb structure such that large mechanical and thermal stresses in failure events can be absorbed by the packaging and not propagated to neighboring cells. It also features are large central cavity used to contain and exhaust gases and particulates released in a failure event. Without active cooling and with electrically-insulating materials separating the aluminum and cell body, cell temperature did not exceed 60 °C and maximum cell-to-cell variation was 7 °C, when subjected to its expected power profile. The module design was also successful at preventing failure propagation in a thermal runaway test (Figure 2.10).
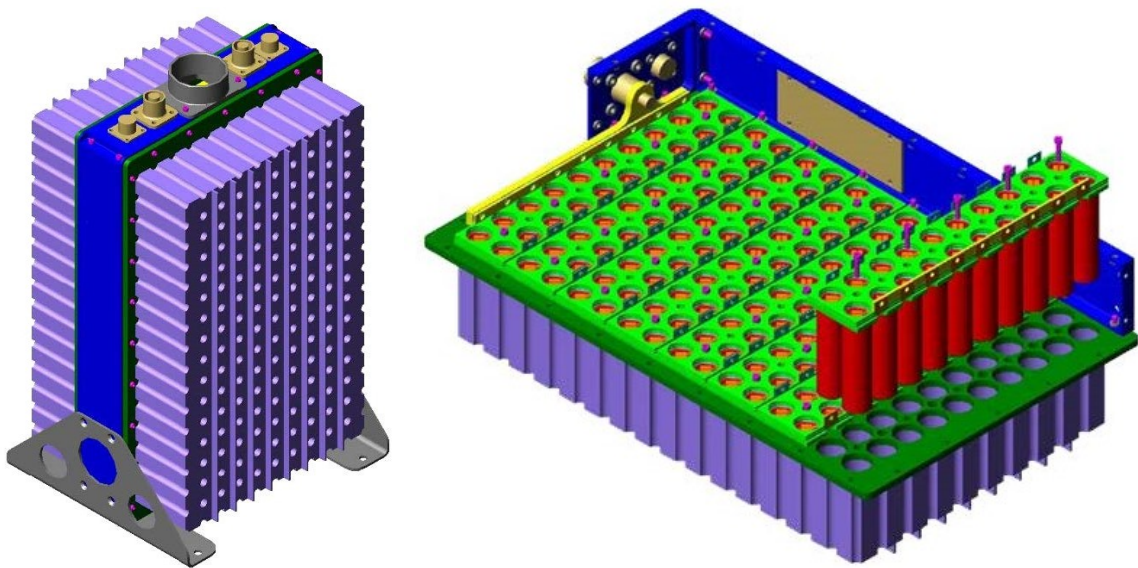
Figure 2.9: Assembly and cutaway views of the NASA X-57 Maxwell battery module [18]
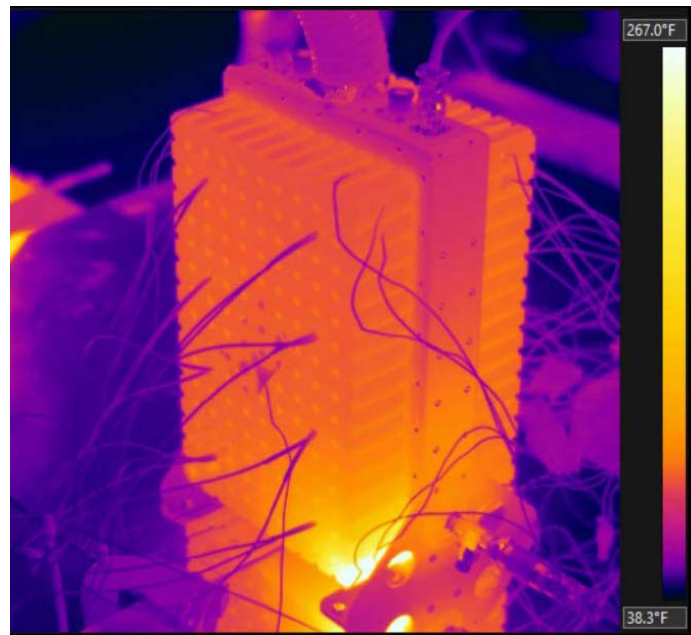
Figure 2.10: NASA X-57 Maxwell battery module successfully distributing heat generated from triggered failure [18]

Chapter 3: Aircraft System Modeling Framework

3.1 System Architecture

The conceptualized propulsion system consists of one wingtip-mounted turbogenerator (TG) and four fan assemblies (FAs) per wing with a centrally-located BESS and electrical distribution system (EDS). The airframe is a traditional tube-and-wing design with two back-swept wings (Figure 3.1). The TGs are turboshaft engines with one or more electric generators mechanically-coupled to the free power turbine and a rectifier electrically-coupled to each generator. The turboshaft engine converts chemical energy (jet fuel) to fluid power in the core of the engine, fluid power to mechanical power at the free turbine, and mechanical power to electrical power at the generator. Additionally, it generates a small amount of "residual" thrust at the nozzle if sufficient energy remains in the fluid when exhausted. The BESS is made up of one or more battery packs, DC-to-DC converters, a BMS, and a TMS. The battery pack (BP) is a bi-directional power source and sink capable of converting stored chemical energy to electrical power and vice-versa. Because of large fluctuations in BP voltage, a DC-to-DC converter is used to regulate the DC link voltage and increase the stability of the DC distribution. The TGs and BESS are used to power the FAs, ducted fans with one or more electric motors mechanically-coupled to the fan shaft through a gearbox and an inverter electrically-coupled to each motor. The motor and inverters are integrated as a single assembly and referred to as an integrated motor drive (IMD). The

46

electric distribution system (EDS) connects the TGs, BESS, and FAs through a network of high-current and high-voltage cabling and electro-mechanical switches.
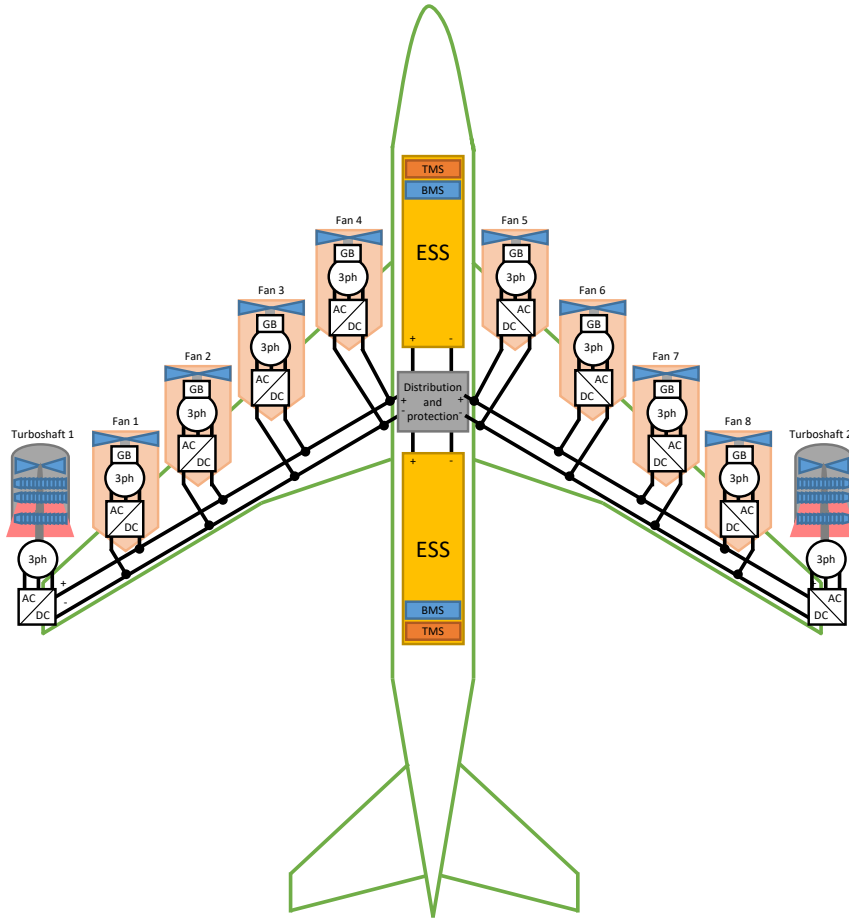
Figure 3.1: Illustration of the system architecture

Locating the TGs at the wingtips may reduce lift-induced drag, but this was not exploited in these studies. The engine has low- and high-pressure spools and a combustor responsible for converting chemical energy to fluid power and bleeds to provide pneumatic power to traditional, non-propulsive systems such as the ECS and AWI system (Figure 3.5).

The generator and rectifier are shown behind the engine for clarity, but, to reduce TMS requirements, would likely be fitted at the front of the engine and connected to the free turbine through a third concentric shaft, making it a triple spool configuration. Any adverse effect this may have on engine inlet flow conditions were not considered. Further, the concept employs two generators and rectifiers for redundancy.

DC power is distributed throughout the aircraft using a "multi-bus, multi-feeder" redundancy strategy (Figure 3.2). The strategy enables power distribution to all FAs in the event of failure of any two generators/rectifiers or one engine. Each generator/rectifier on a given wing is capable of powering all four FAs on that wing, while one generator/rectifier on each wing is linked to the distribution system on the other wing.
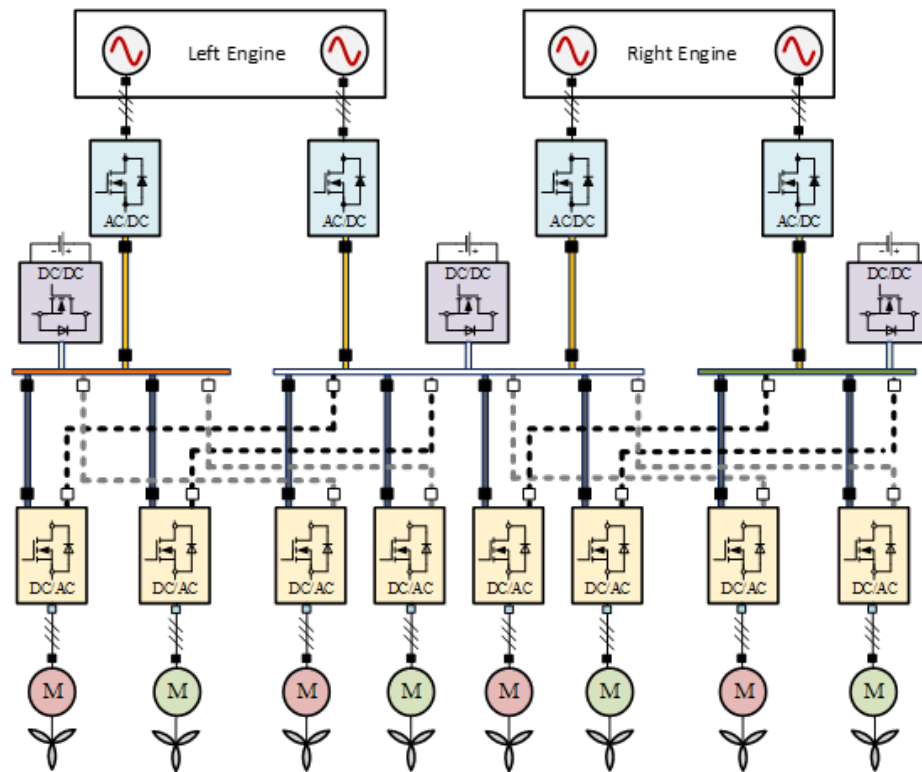
Figure 3.2: The multi-bus, multi-feeder electrical distribution system design (Figure courtesy of OSU-CHPPE)

48

The FAs are distributed span-wise along the leading edge and underside of the wings. This serves primarily to increase the eBPR, as there is minimal aerodynamic coupling between the fans and airframe, but also to provide redundancy. Each fan is driven by a permanent-magnet machine that is excited by a full-bridge inverter with SiC switches (Figure 3.9) [59].

The motors and inverters are cooled by an air-cooled oil cooling system, while the ECS is oversized to accommodate the cooling requirements of the BESS, located in the floor of the fuselage. Additional details regarding the TMS and EDS are provided by [60]. The design and control of the BESS are the main variables explored in this research. With the exception of engine bleeds, non-propulsive power sinks and sources are not evaluated; thus, the BESS is only considered to supplement propulsive power. Sizing of each subsystem is discussed in Section 3.3. Within the scope of this work, further detailed design of the system was not investigated.

3.2   Model Architecture

The Map-based Aircraft Propulsion Simulator (tMAPS), a MATLAB-based tool, was developed for the purpose of co-optimizing the energy storage system design and energy management control. tMAPS houses an energy-based aircraft propulsion model coupled to the DP function developed by [61]. Reduced-order, quasi-static subsystem models were used to capture the behavior of the HEDP system. The model was developed with the purpose of solving optimal control problems via DP. In the context of energy management, reduced order models are well-known to be sufficient for accurate energy estimation. Application of DP necessitated the use of reduced-order models but also enables objective comparison of design variations.

The model includes steady-state maps to simulate turbomachinery performance (accounting for operational limits) and total drag. The steady-state maps are derived from higher fidelity models such as Numerical Propulsion System Simulation (NPSS) and Flight Optimization System (FLOPS). The battery pack performance is predicted using an ECM with dependence SOC and directionality (discharge/charge). The remainder of the electric powertrain is modeled using either a constant efficiency or efficiency maps. Torque and speed are matched at mechanical connections, while only power is matched at electrical connections.

The model is structured in order to represent the backward flow of power in the system, i.e. the propulsive power is back-calculated from a prescribed aircraft speed and altitude. This modeling approach is desirable for quick and objective comparisons of system design variations. The aircraft mission profile is given as an input to the model, and the model works backwards to determine the engine fuel consumption and battery power request. The model architecture is shown in Figure 3.3. The following sections detail the model equations in the order in which they are solved. As a general note, all components are considered to perform and be operated equally to their counterparts.

3.2.1 Equations of Motion

The model requires the following mission data: time t, distance x, altitude z, and velocity v, which is non-dimensionalized as Mach number (MN). These are differentiated in time to determine inertial velocities $\dot{x}$ and $\dot{z}$ and acceleration $\dot{v}$. The flight path angle γ results from a trigonometric relationship between inertial velocities. The aircraft is considered to be a point mass with total mass m_{tot}, and motion is simplified to two dimensions; thus, the lift
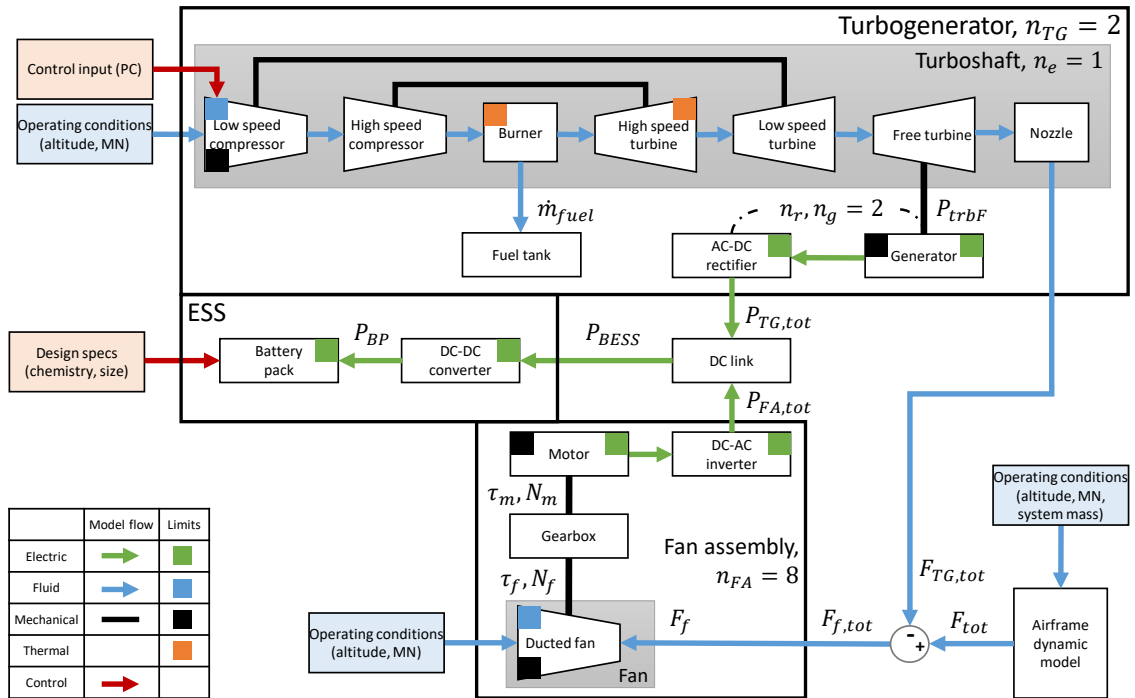
Figure 3.3: Backwards model architecture for the HEDP system
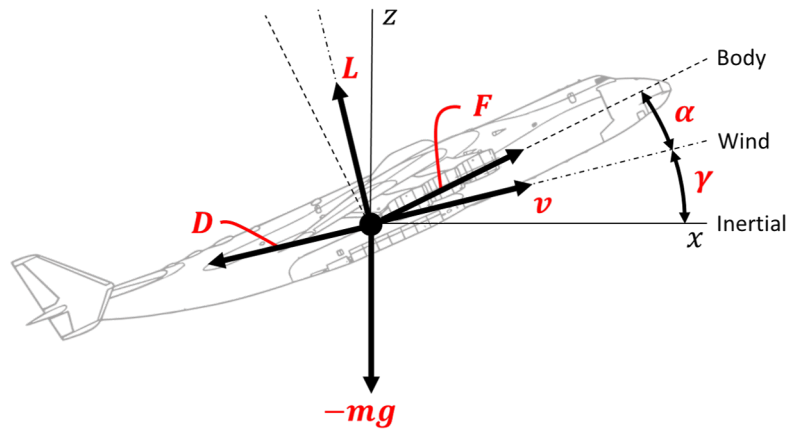
Figure 3.4: Components of two-dimensional equations of motion

force L is given by

$$L = m_{tot} v \dot{\gamma} + m_{tot} g \cos \gamma - F_{tot} \sin \alpha \tag{3.1}$$

where g is the acceleration of gravity. Assuming the angle of attack α is sufficiently small, this reduces to

$$L = m_{tot} v \dot{\gamma} + m_{tot} g \cos \gamma \tag{3.2}$$

Further, lift is related to the lift coefficient C_L by the following:

$$L = \frac{1}{2} C_L S \rho_\infty v^2 \implies C_L = \frac{2(m_{tot} v \dot{\gamma} + m_{tot} g \cos \gamma)}{S \rho_\infty v^2} \tag{3.3}$$

where S is the lift/drag reference area and ρ_∞ is the ambient air density. The total system mass is equal to the sum of the operating empty weight (OEW), payload mass (m_{pay}), BESS mass (m_{BESS}), and fuel mass (m_{fuel}) as defined here:

$$m_{tot} = \text{OEW} + m_{pay} + m_{BESS} + m_{fuel} \tag{3.4}$$

The zero-lift and lift-dependent drag coefficients $C_{D,0}$ and $C_{D,i}$, respectively, are mapped as is a function of the MN and lift coefficient.

$$C_{D,0} = f(\text{MN}, z) \tag{3.5}$$

$$C_{D,i} = f(\text{MN}, C_L) \tag{3.6}$$

The drag force D is computed using

$$D = \frac{1}{2} (C_{D,0} + C_{D,i}) S \rho_\infty v^2 \tag{3.7}$$

The total system thrust F_{tot}, such that the mission profile is followed, must be equal to

$$F_{tot} = m_{tot} \dot{v} + m_{tot} g \sin \gamma + D \tag{3.8}$$

Note that the small angle approximation is valid for $\alpha \leq |\pm 15$. Error in the actual trigono-metric functions is less than 1% within this range, and, for this application, the angle of attack is expected to be within this range.

3.2.2 Turbogenerators

The TGs are the primary source of electrical power, and the low-pressure compressor corrected speed ratio, or "speed ratio" r_N, is the control input for regulating the power and thrust generated by the TG, and, consequently, the electrical power and thrust split of the system. The control input must be known *a priori*. The speed ratio ranges between minimum and maximum values of $r_N^m = 0.45$ and $r_N^M = 1.00$, respectively. The fuel mass flow rate $\dot{m}_{fuel}$, the free turbine power P_{trbF}, and net thrust F_{TG} are mapped as

$$\dot{m}_{fuel}, P_{trbF}, F_{TG} = f(\mathrm{MN}, z, r_N) \tag{3.9}$$

The fuel mass carried by the aircraft changes at each time step Δt due to the fuel burn and is updated as follows:

$$m_{fuel}(t + \Delta t) = m_{fuel}(t) - \dot{m}_{fuel}\Delta t \tag{3.10}$$

It is assumed the electric generators are directly driven by the free turbine with no mechanical losses. The generator electrical output power is a function of its efficiency η_g, considered constant. Rectifiers are required to convert AC to DC power; the cabling between the generator and rectifier is considered to have negligible losses. The rectifier output and input power are also related by an efficiency η_r, considered constant. Then, there are transmission losses represented with a transmission efficiency η_t, considered constant. The total TG power input at the DC link is

$$P_{TG,tot} = n_{TG}\eta_t\eta_r\eta_g P_{trbF} \tag{3.11}$$

3.2.3 Fan Array

The primary propulsion system is an array of ducted fans mounted on the wings of the aircraft, while the net thrust of the TGs can be supplemental or detrimental. The individual fan thrust F_f is a fraction of the difference between total system thrust required and the net thrust produced by each TG, written as

$$F_f = \frac{F_{tot} - n_{TG}F_{TG}}{n_f} \tag{3.12}$$

The fan torque τ_f and speed N_f are mapped as

$$\tau_f, N_f = f(\text{MN}, z, F_f) \tag{3.13}$$

The fan and its driving motor are mechanically coupled through a gearbox, assumed to be a single-reduction gearbox, with a gear ratio r_{GB}. Then, considering the efficiency of the gearbox (η_{GB}) to be constant, the motor torque τ_m and speed N_m follow kinematic relationships such that

$$N_m = r_{GB}N_f \tag{3.14}$$

$$\tau_m = \frac{1}{\eta_{GB}} \frac{\tau_f}{r_{GB}} \tag{3.15}$$

The mechanical output power and electrical input power are related by the motor efficiency η_m, considered constant. The power input to the motor is supplied by an inverter, converting DC to AC power. The cabling between the motor and inverter is typically very short; thus, transmission losses are neglected and the motor input power is equal to the inverter power output. The inverter output and input power are also related by its efficiency η_i, considered constant. Further, there are transmission losses between the inverters and DC link. Then, the power output from the DC link to the FAs must be

$$P_{FA,tot} = \frac{1}{\eta_t \eta_i \eta_m \eta_{GB}} n_f P_f \tag{3.16}$$

54

Note that, at each time step, the propulsion system power must be supplied by the TGs $P_{TG,tot}$ and/or the BESS P_{BESS}. DP is used to optimize the control policy at each instance of time over the mission.

3.2.4 DC Link

The TGs, FAs, and BESS are linked through a distribution box connecting primary and secondary cable lines to electro-mechanical switches and other protection and sense equipment. The distribution box is bi-directional with losses captured by considering a lumped, constant efficiency η_d. The BESS is the only subsystem considered to act as both a source and sink such that

$$\Delta P = P_{FA,tot} - \eta_d P_{TG,tot} \tag{3.17}$$

$$P_{BESS} = \begin{cases} \frac{1}{\eta_d} \Delta P & \Delta P \geq 0 \implies \text{Discharging} \\ \eta_d \Delta P & \Delta P < 0 \implies \text{Charging} \end{cases} \tag{3.18}$$

3.2.5 Battery Energy Storage System

With the TG power given by the control input and the FA power constrained by the thrust balance, the BESS power is constrained by the power balance given in Equation (3.18). Transmission losses are neglected considering the proximity of the BESS to the DC link. The DC-to-DC converter introduces additional losses modeled using a constant efficiency η_c, which results in battery pack power P_{BP} of

$$P_{BP} = \begin{cases} \frac{1}{\eta_c} P_{BESS} & P_{BESS} \geq 0 \\ \eta_c P_{BESS} & P_{BESS} < 0 \end{cases} \tag{3.19}$$

The battery pack contains cells connected in series n_s and parallel n_p. The power requested from a single cell is

$$P_{cell} = \frac{1}{n_s n_p} P_{BP} \tag{3.20}$$

Cell open circuit voltage (OCV), internal resistance R_{cell}, and power limits P_{cell}^M are mapped as

$$\text{OCV}, R_{cell}, P_{cell}^M = f(\text{SOC}, \text{sgn}(I_{cell})) \tag{3.21}$$

A zeroth order ECM has been adopted based on Equations (3.22)-(3.24). The cell current I_{cell}, terminal voltage V_{cell}, and SOC can be derived from the OCV, internal resistance, and nominal capacity C_{nom} as function of the power request:

$$I_{cell} = \frac{\text{OCV} - \sqrt{\text{OCV}^2 - 4R_{cell}P_{cell}}}{2R_{cell}} \tag{3.22}$$

$$V_{cell} = \text{OCV} - R_{cell}I_{cell} \tag{3.23}$$

$$\text{SOC}(t + \Delta t) = \text{SOC}(t) - \frac{I_{cell}}{C_{nom}}\Delta t \tag{3.24}$$

The battery management system (BMS) is largely responsible for enforcing operability limits such as

$$P_{cell} \in \left[P_{cell}^{M-}, P_{cell}^{M+} \right] \tag{3.25}$$

$$I_{cell} \in \left[I_{cell}^{M-}, I_{cell}^{M+} \right] \tag{3.26}$$

$$V_{cell} \in \left[V_{cell}^{m}, V_{cell}^{M} \right] \tag{3.27}$$

$$\text{SOC} \in \left[\text{SOC}^m, \text{SOC}^M \right] \tag{3.28}$$

as well as temperature limits, which are neglected here. The superscripts m, M, $-$, and $+$ indicate minimum and maximum limits in charge and discharge, respectively. Note the sign convention is power and current in charge are negative. The power, current, and voltage of the battery pack P_{BP}, I_{BP}, and V_{BP}, respectively, which respect limits, are scaled from the

cell model, again considering the pack architecture:

$$P_{BP} = n_s n_p P_{cell} \qquad (3.29)$$

$$I_{BP} = n_p I_{cell} \qquad (3.30)$$

$$V_{BP} = n_s V_{BP} \qquad (3.31)$$

If the propulsive power is provided solely by the TGs, e.g. the TEDP architecture, the system is fully determined. A forward simulation can be performed if the system is fully determined or if the control input is known *a priori*. Otherwise, various control inputs can be evaluated at each time step, e.g. in DP, and the system can be determined via some objective function.

3.3 Model Calibration

The concept aircraft is based on a CRJ-900 regional jet aircraft with turbomachinery and airframe improvements expected of an aircraft entering service in 2030. The concept matches the CRJ-900's maximum payload design range of 3700 km carrying 86 passengers and luggage, totaling a payload of 8.2 mt; however, it was found that adding a BESS to the system offers negligible benefit, oftentimes being detrimental, to fuel consumption at the design range. Two propulsion system configurations will be compared throughout this work. The "reference" configuration is a (TEDP) configuration, which is necessary to meet the maximum payload design range goals, considering current limitations of battery technology. The two configurations were then compared over a subset of three missions with sub-2000-km range and a payload of 3.7 mt.

3.3.1 Airframe and Turbomachinery

Detailed modeling of the propulsion system was performed in NPSS and GT-HEAT. In "on-design" analysis, NPSS iteratively updates the component design until user-specified propulsion system design parameters are met at design points. Once complete, the "off-design" propulsion system model and user-specified airframe design parameters are used by FLOPS to size the airframe and estimate aerodynamic performance. Given the airframe design, the turboshaft engine and ducted fan models were decoupled from the propulsion system to simplify the process of further design refinement and performance map generation [62]. This was only possible because the aircraft is not designed to take advantage of the synergies between the propulsion system and airframe that are capable of improving propulsive efficiency, as discussed in Section 1.1. Assuming performance is improved, further refinement of other subsystems would simply imply conservative sizing and performance of the airframe.

The engine was modeled after the General Electric CF34 engine, original to the CRJ-900, but fitted with a downstream free power turbine and different nozzle (Figure 3.5). Technology improvements include -20% low-pressure compressor (LPC) mass, +0.1% LPC efficiency, -5% high-pressure compressor (HPC) mass, +0.47% HPC effiency, +5% HPC stage loading, +83°C high-pressure turbine (HPT) temperature limit, and -13% low-pressure turbine (LPT) mass. The ducted fans are modeled via a single stage compressor and nozzle in NPSS. These models were provided by Georgia Tech's (GT) Aerospace Design Laboratory (ASDL).

Off-design simulations of the decoupled engine and fan models were conducted at every combination of MN and altitude in the operational envelope (Figure 3.6). The operational envelope was built considering limitations of the turbomachines and airframe. Missions A,
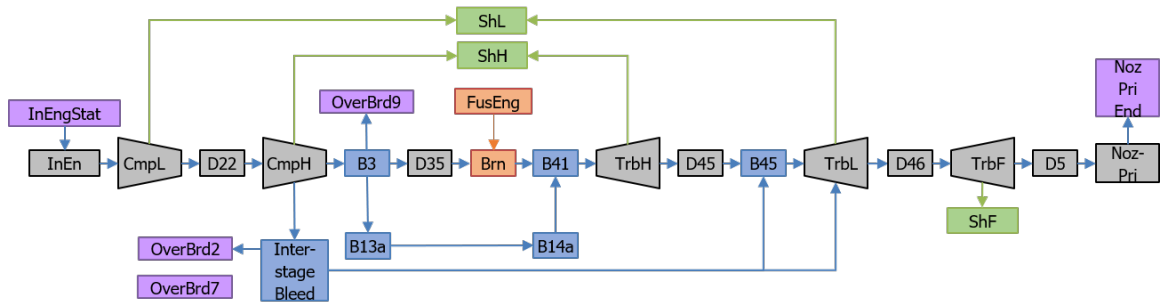
Figure 3.5: Detailed block diagram of the turboshaft to highlight components and interfaces (orange for fuel, blue for air, and green for mechanical)

B, and C and the reserve mission all fall within its bounds. MN and altitude serve as two of the independent variables influencing turbomachine performance. Mission B is overlaid on the operating envelope to highlight the scheduled MN and altitude combinations.

The LPC corrected speed was varied to encapsulate every feasible operating point of the engine. The upper bound of the compressor corrected speed is limited to 100% of the design corrected speed or the maximum turbine inlet temperature (2028 K for vehicle speeds equal to or below 0.05 Mach and 1939 K for any other speed), depending on which condition is met first. The speed is iteratively decreased until stall occurs, i.e. the solver does not converge. Similarly, maximum fan torque is limited at 100% corrected fan speed and is iteratively decreased until stall occurs. Figure 3.7 provides some insight into turboshaft and fan performance at MN and altitude combinations common to the mission profiles.

The airframe technology improvements include a -10% structural mass, -10% zero-lift drag, and -10% lift-induced drag. The fuselage dimensions were kept the same as the CRJ-900, but the wing and tail surfaces were slightly resized ($S \approx 69.9m^2$). While maps are generated for the drag coefficients per Equations 3.5-3.6, Figure 3.7 shows the relationship
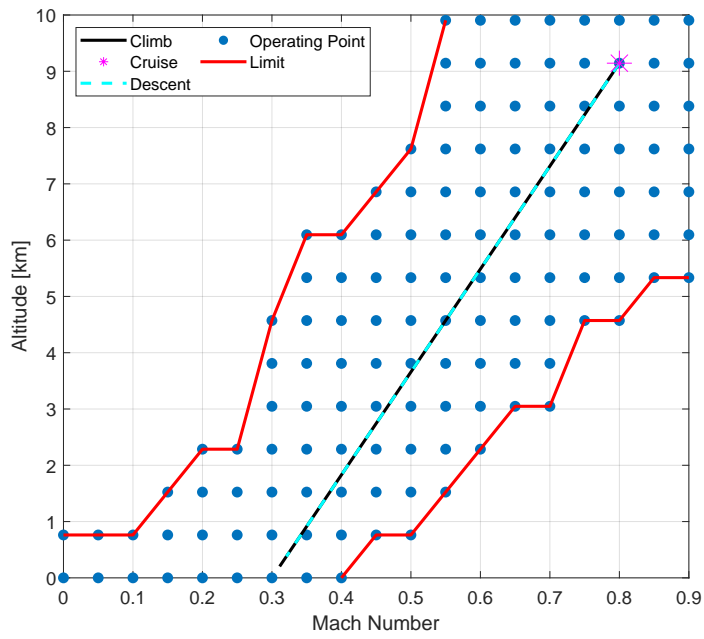
Figure 3.6: Operational envelope of the propulsion system and airframe indicating operating points used for off-design map generation
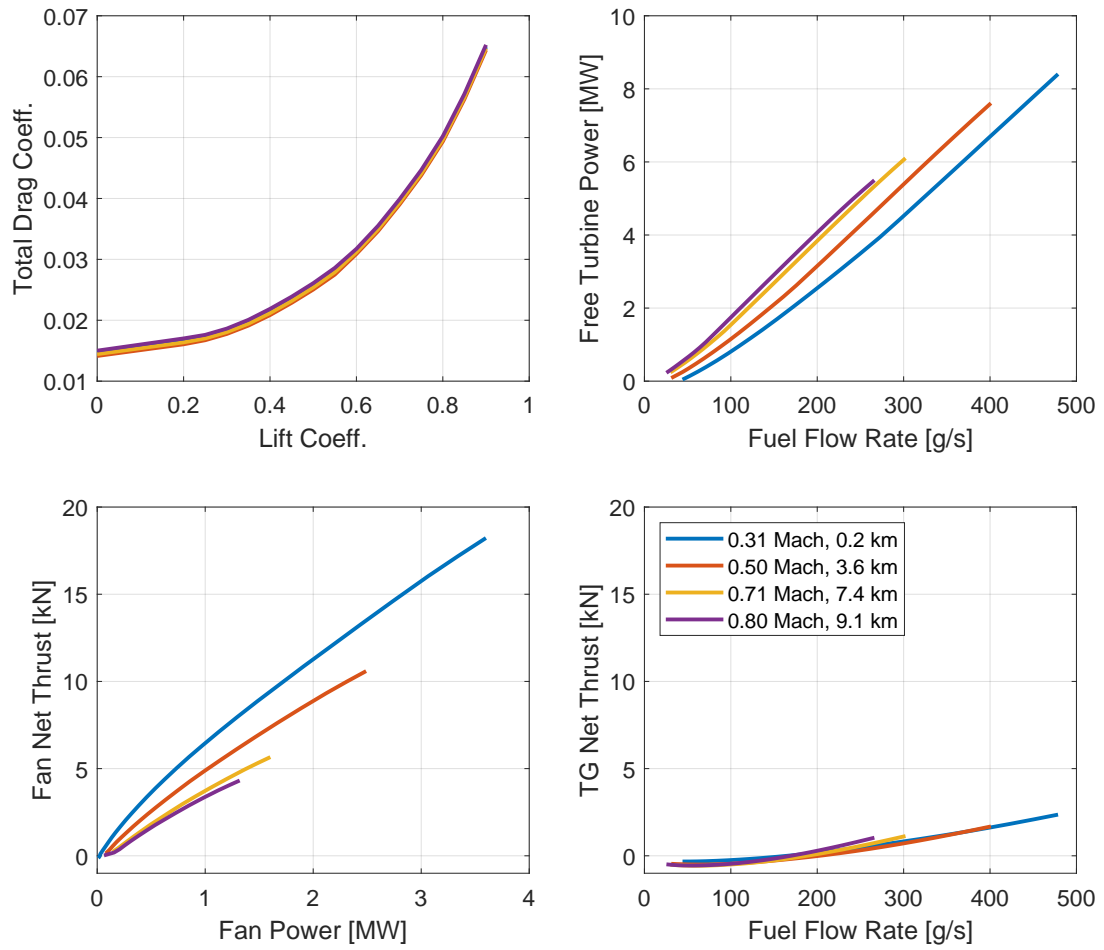
Figure 3.7: Select operating points from Mission B at which aerodynamic and turbomachinery performance maps are sampled

between the lift coefficient and total drag coefficient throughout a typical mission profile. The airframe, engine, and fan masses are tabulated in Section 3.3.3.

3.3.2   Electric Powertrain

The power electronics, AC-to-DC rectifiers, DC-to-AC inverters, and DC-to-DC converters; electric machines, motors and generators; and the EDS are all part of the electric powertrain. University of Wisconsin's (UW) Electric Machines and Power Electronics Consortium (EMPEC) and The Ohio State University's (OSU) Center for High Performance Power Electronics (CHPPE) are responsible for the design of the integrated fan motor and inverter. High-level specifications of the turbine generator and rectifer and DC-to-DC converter reference specifications provided for the motor and inverter. GT-ASDL is responsible for the design of the EDS.

The motor is targeted to produce 2.1 MW of maximum continuous power at a power density of 15 kW/kg. An inner rotor surface permament magnet (IRSPM) topology was chosen for the motor [59]. 2D FEA was used to evaluate the electromagnetic performance and 3D FEA was used to evaluate mechanical stresses as the machine sizing and structural design were iterated until requirements were met. Design and analysis of a 1 MW machine with the same topology and materials estimates an efficiency of 96.9% at 1 MW of continuous power output, considering losses in the core, winding, and sleeve. The active mass power density reported is 23.6 kW/kg; however, this includes only the stator core, windings, and sleeve and rotor core, magnets, and sleeve. It is assumed that addition of the shaft, hub, bearings, cooling jacket, and endbells will reduce the power density to the targeted 15 kW/kg (Figure 3.8).
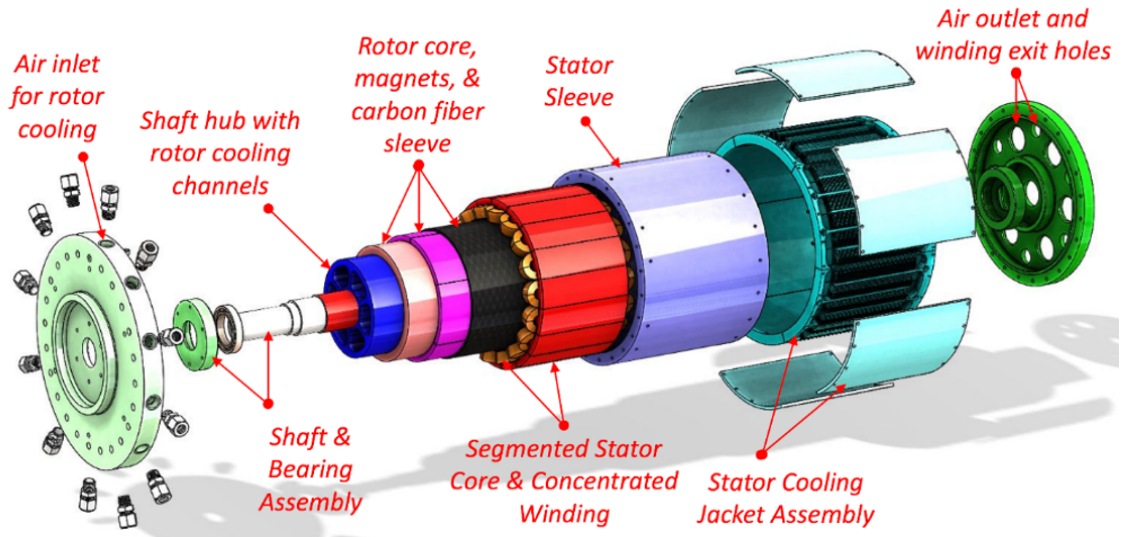
Figure 3.8: Exploded view of a 200 kW machine of the same topology and materials intended for the 2.1 MW design (Figure courtesy of UW-EMPEC)

The 1 MW, 2000 V inverter design incorporates SiC half-bridge power modules. Each half-bridge module has its own capacitor bank and gate drive in a sub-assembly. Two half-bridge module sub-assemblies are connected to form a full-bridge, or H-bridge, controlled using a master gate drive, and three full-bridge assemblies are connected in series to distribute the full DC link voltage; thus, each phase requires six power modules each, and the inverter requires 18 module sub-assemblies in total. Half-bridge power modules enable the inverter to be easily integrated into the motor assembly. Switching and conduction losses are estimated for each power module referencing specifications from [63]. The switching losses are a function of module voltage, current, switching frequency, while the conduction losses are a function of module current and MOSFET on-resistance.

The final IMD design must be capable of 2.1 MW of power output. It is assumed that two IMDs can be coupled to double the power output, which would practically double the

63
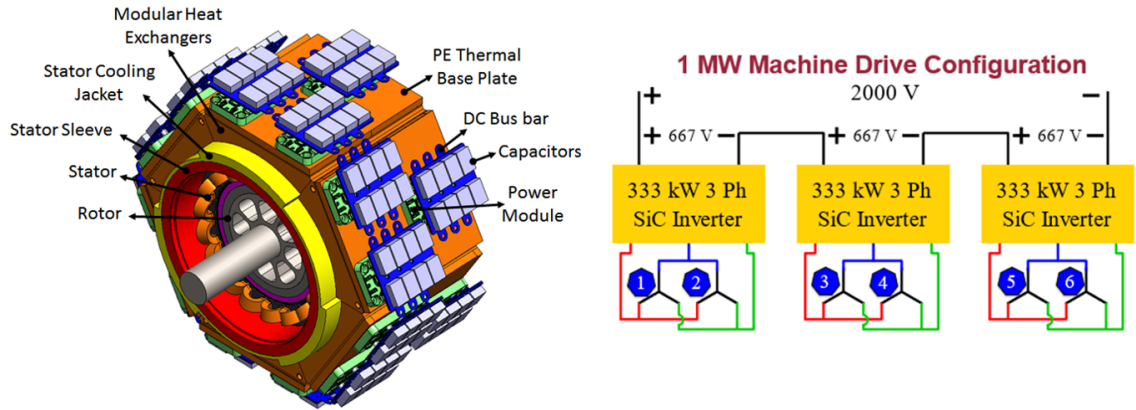
Figure 3.9: The 1 MW "integrated motor drive" machine assembly rendering and drive configuration (Figure courtesy of UW-EMPEC and OSU-CHPPE)

losses. In this case, the scaling factor is actually 2.1. Inverter efficiency as a function of power output, assuming constant DC link voltage, and motor efficiency as a function of torque and speed, both for the 1 MW machines, were provided. Losses and power/torque, at which they originally occurred, were increased by the scaling factor to obtain the efficiency map/curve shown in Figure 3.10.

The motor torque and speed and inverter power shown are for select missions, which highlight both extremes of climb rate and gross takeoff weight (GTOW). The gear ratio of 4.36 was determined by dividing the maximum speed of the motor by that of the fan (across all missions shown) and results in the operating curves shown. From these results, it was determined it is appropriate to assume a constant efficiency of 97.5% and 98.3% for the motor and inverter, respectively. Any major variation from these values results at relatively low power as the motors are throttled back to idle power in descent.

The 4.5 MW generators and rectifiers are assumed to match the motors and inverters in performance with power densities of 15 kW/kg and 25 kW/kg and constant efficiencies of
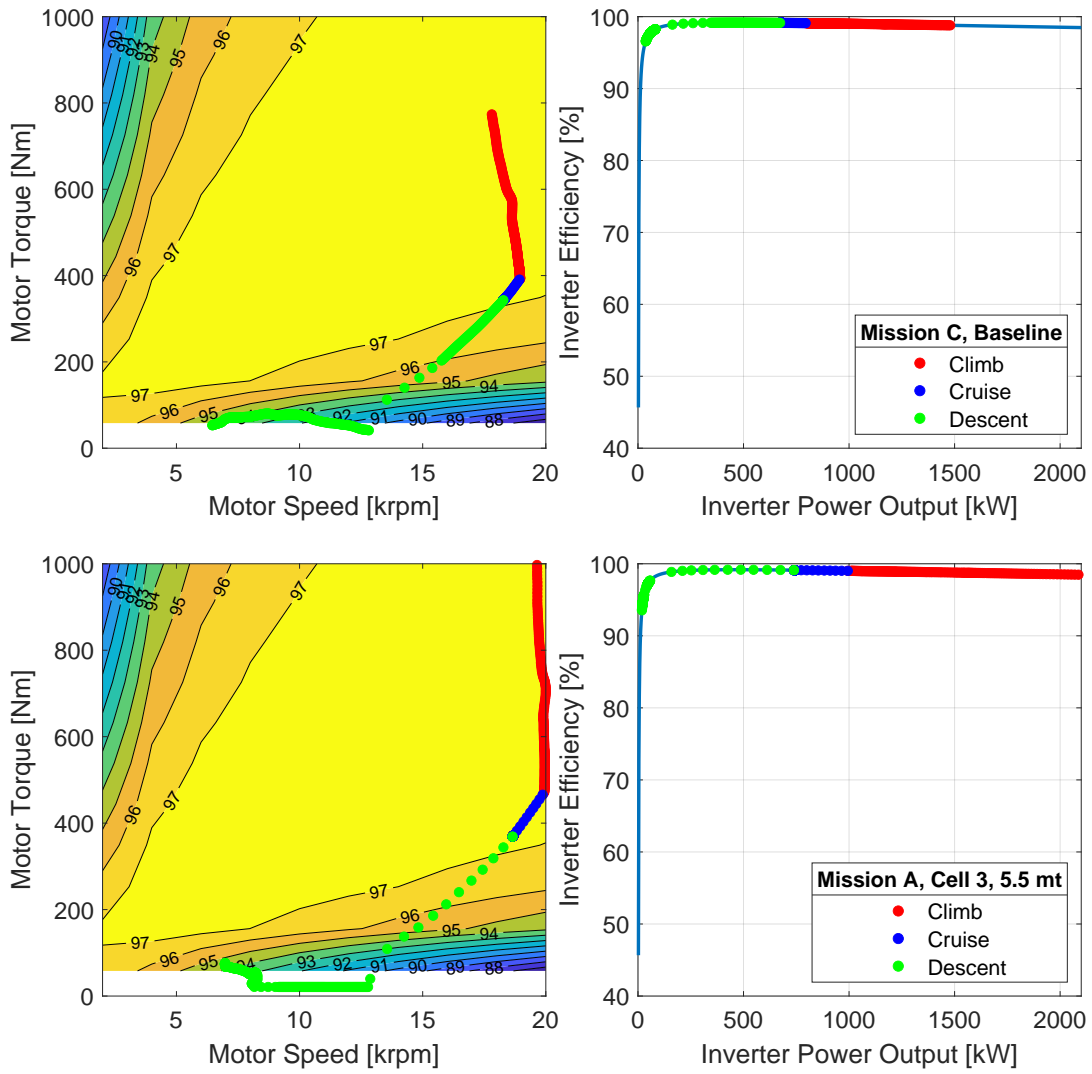
Figure 3.10: Scaled efficiency maps for 2.1 MW electric machine and power inverter

97.5% and 98.3%, respectively. While design and integration of the generators and rectifiers was not evaluated, these can be considered conservative estimates because typically these figures improve for components of the same topology with increased power. Similarly, the DC-to-DC converter is assigned a constant efficiency of 98.3%, but its power density is assumed to be lower at 20 kW/kg because of its relatively large number of reactive components. The sizing of the DC-to-DC converter is battery pack specific. Lastly, losses are neglected in the EDS, except the distribution box is 98% efficient. Masses are tabulated in Section 3.3.3

3.3.3 Battery Energy Storage System

The candidate cells are the Sony US18650VTC6, Kokam SLPB065070180, Efest IMR18650 (3.5 Ah), OXIS POA000343, Zenlabs Glide, and OXIS POA000412, referred to as Cell 1-6, respectively. Cells 1-3 are commercially available and have all been characterized by OSU's Center for Automotive Research (CAR). These were down-selected from a larger sampling of cells, which also included NMC and NCA chemistries. Cells 4-6 are low Technology Readiness Level (TRL) and only available as prototypes; Cell 5 was characterized by OSU-CAR, and Cells 4 and 6 are modeled using only supplier specifications.

The commercially-available candidates were chosen based on performance of multiple samples subjected to room-temperature, multi-rate static and dynamic tests such as capacity, HPPC, and RCID tests. Cells 1-3 were proven to offer the best balance between energy and power density and the least cell-to-cell variation. These cells were then put through the same tests at multiple temperatures to complete the characterization process. Being low TRL, Cell 5 was limited to room-temperature, relatively low C-rate static and dynamic tests. tMAPS

Table 3.1: Summary of cell manufacturer specifications and characterization data

		Cell					
		1 [64]	2 [65]	3 [66]	4 [67]	5 [68]	6 [69]
Manufacturer		Sony	Kokam	Efest	OXIS	Zenlabs	OXIS
Format		Cyl.	Pouch	Cyl.		Pouch	
Chemistry		NMC	H-NMC	LMO	Li-S	Si	Li-S
Mass	g	47	173	47	140	131	85
Volume	cm^3	17	91	18	191	68	113
Nominal capacity	Ah	3.0	12.0	3.5	19.5	12.7	16.0
Nominal voltage	V	3.6	3.7	3.7	2.15	3.7	2.15
Maximum voltage	V	4.2	4.2	4.2	2.6	4.47	2.6
Minimum voltage	V	2.5	2.7	2.5	1.9	2.5	1.9
Cont. dch. rate	C-rate	5	2	2.85	3	1	1
Pulse dch. rate	C-rate	10	4	5.71	-	3	-
Cont. ch. rate	C-rate	1	1	1.14	0.2	1	0.2
Energy density*	**Wh/kg**	**232**	**257**	**278**	**299**	**359**	**405**
Energy density*	Wh/L	628	487	739	220	695	304
Power density*	**W/kg**	**1159**	**513**	**794**	**898**	**359**	**405**
Power density*	W/L	3141	973	2111	660	695	304
Internal dch. res.[†]	mΩ	35	10	51	4[‡]	42	6[‡]
Internal ch. res.[†]	mΩ	34	8	44	4[‡]	42	6[‡]
Pulse dch. power[†]	W	91	278	60	93[‡]	76	50[‡]
Pulse ch. power[†]	W	55	256	49	242[‡]	74	137[‡]

*Based on nominal capacity and voltage and continuous discharge rate
[†]At 23°C and 50% SOC, HPPC at max C-rate or RCID averaged across all pulses, 30 second pulse
[‡]From datasheet, note that these cells have a drastically different OCV profile

does not include a thermal or aging model; thus, a small subset of the full characterization data set was utilized. More detail regarding this will be discussed in Chapter 5.

For each cell, a zeroth-order, SOC- and mode-dependent ECM was developed per Section 2.2.1 and employed in tMAPS. The mass and maximum voltage are used for BESS sizing; the nominal capacity and internal resistance are used in the ECM; and the voltage limits, continuous rate limits, and power limits are used to define infeasibilities (Section 4.1). This information is summarized in Table 3.1, and the full characterization of Cell 3 is shown in Figure 3.11.
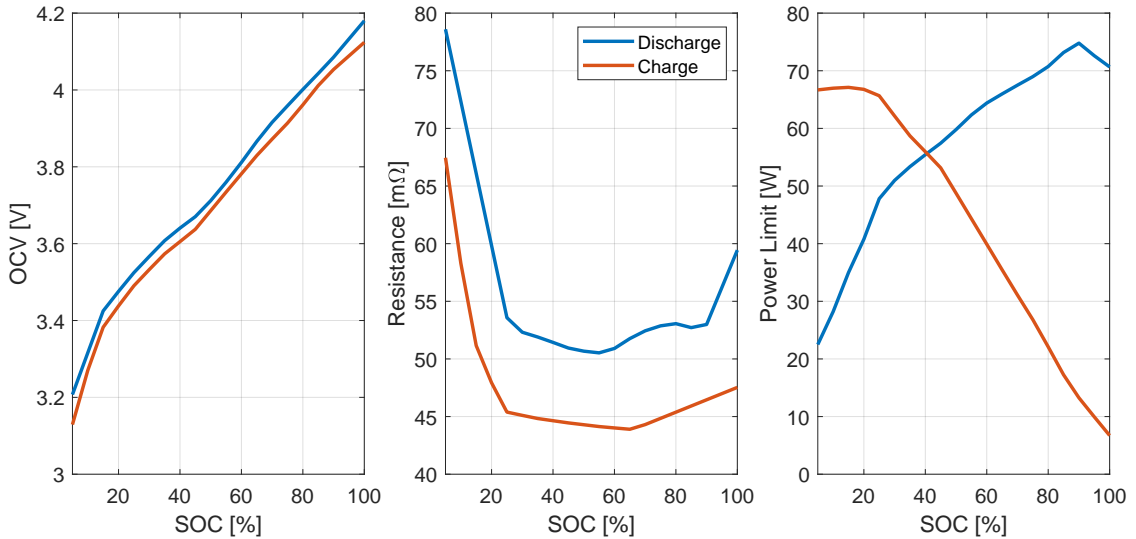
Figure 3.11: SOC- and mode-dependent parameters of Cell 3

The sizing of the BESS is an iterative process. The maximum BP mass m_{BP}^M is initially assumed to be equal to the target BESS mass m_{BESS}^*. The maximum total cell mass $m_{cell,tot}^M$ depends on the mass ratio of cells in the BP r_{cell}. The number of cells in series n_s is constrained by either the maximum system voltage V^M or $m_{cell,tot}^M$. If n_s is mass limited,

the number of cells in parallel n_p is equal to 1, and, if not, the n_p is equal to the maximum allowable by the mass constraint, as described by the following:

$$n_s = \left\lfloor \min\left(\frac{V^M}{V^M_{cell}}, \frac{r_{cell} \cdot m^M_{BP}}{m_{cell}}\right) \right\rfloor \tag{3.32}$$

$$n_p = \left\lfloor \max\left(1, \frac{r_{cell} \cdot m^M_{BP}}{n_s \cdot m_{cell}}\right) \right\rfloor \tag{3.33}$$

The actual BP mass is computed:

$$m_{BP} = \frac{1}{r_{cell}} n_s n_p m_{cell} \tag{3.34}$$

The maximum BP power is determined based on the specific cell selection and BP sizing:

$$P^M_{BP} = n_s n_p \left(\max\left(P^{M-}_{cell}, P^{M+}_{cell}\right)\right) \tag{3.35}$$

The DC-to-DC converter is then sized based on its power density GPD_c and P^M_{BP}:

$$m_c = \text{GPD}_c \cdot P^M_{BP} \tag{3.36}$$

The summation of m_{BP} and m_c is then compared to m^*_{BESS}, and the BP and converter sizing are updated until they agree. The BESS size is limited by the maximum takeoff weight (MTOW) of the aircraft.

The mass breakdown of the aircraft is given in Table 3.2. The power density of the gearbox is roughly estimated at 82 kW/kg; the Pratt & Whitney PW8000 gearbox developed in the 1990s is reported to have a power density between 82 kW/kg [70] and 108 kW/kg [71], while a more recent patent filing suggests development of a turbofan gearbox with power density ranging between 82 to 123 kW/kg [72]. All masses are fixed except those of the fuel and BESS, which combined are limited to 7.1 mt. Payload and BESS mass are free to be traded, and this will of course impact the fuel mass and flight revenue, but the payload listed was used for all studies presented in this work.

Table 3.2: Sizing summary and mass breakdown of HEDP aircraft concept

	Rated Power [MW]	GPD [kW/kg]	Qty.	Total Mass [mt]
MTOW	-	-	-	**34.0**
Structure, systems, and equipment	-	-	-	14.1
Engines	-	-	2	0.7
Generators	4.5	15	4	1.2
Rectifiers	4.5	25	4	0.7
Electric distribution system	-	-	-	2.2
Inverters	2.1	25	8	0.7
Motors	2.1	15	8	1.1
Gearboxes	2.1	82	8	0.2
Fans	-	-	8	2.3
Payload	-	-	-	3.7
Max combined fuel and BESS	-	-	-	**7.1**

3.4 Model Validation

The system of equations and airframe and turbomachinery performance maps used in tMAPS were validated against results obtained from GT-HEAT. GT-HEAT is built on the framework of NASA's suite of conceptual aircraft design tools, which includes NPSS, FLOPS, and Weight Analysis of Turbine Engines (WATE). GT-HEAT served to add electrical and energy storage modeling capability to propulsion system models built in NPSS such that hybrid-electric propulsion concepts could be evaluated. However, running simulations in this framework has too high of computational cost to use DP.

The maps used in tMAPS were generated using the same element structure and parameters as used in GT-HEAT. To isolate the source of errors to drag and turbomachinery maps, the validation was conducted under the assumption of a constant motor efficiency of 93% and, otherwise, 100% efficiency in the electric powertrain. Additionally, an energy model

was used in place of an ECM to enable flexibility in the prescribed power split and because the battery model did not need to be validated in this context.

GT-HEAT includes an iterative process for determining fuel consumption and BP sizing based on the specified power split in climb and cruise segments. For every simulation, tMAPS was initialized with the same OEW, payload, BESS, and fuel mass. The same mission profile was used for simulations in GT-HEAT and tMAPS, but note that these mission profiles are not the same as those described in Chapter 4 and explored later. The mission profiles used for validation have a slightly more dynamic climb schedule. Both non-hybrid and hybrid missions of different lengths were simulated to fully exercise the maps. For validation, the input to tMAPS was the BESS power split, defined by mission segment as indicated in Table 3.3, and engine control was determined such that the error in power split was minimized. The target power split in descent was zero for all simulations.

The RMSE and relative (percent) RMSE for variables of interest, i.e. those evaluated using performance maps generated in NPSS and FLOPS, are presented in Table 3.3. The mean RMSE of the drag force D, total thrust output F_{tot}, fan power input P_f, engine (free power turbine) power output P_{trbF}, fuel burn, and fuel savings is 144 N, 371 N, 114 kW, 106 kW, 19 kg, and 5 kg, respectively. The corresponding mean rRMSE is 0.84%, 1.50%, 1.74%, 1.78%, 1.30%, and 0.40%. The majority of the error is introduced in the drag and thrust force estimations, with some additional error present in the implementation of the turbomachinery maps. Ultimately, tMAPS was developed for evaluating the fuel savings achieved through hybridization of the propulsion system. The fuel savings percent error is relative to the fuel burn, as is the percent fuel savings reported later, and its mean percent error indicates the model results are valid for fuel savings as low as 1.2%. However, note

71

that the error increases with increasing BESS power in climb, with percent error as high as 1.08% error, and vice-versa, with percent error as low as 0.03%.

The reported error does not include error present in the descent segment. Figure 3.12 shows a sample of the model behavior and how it compares to the results of GT-HEAT for a 550 km range mission with no battery pack supplement; these results are representative of the full validation set. The models match very well in all phases, except for descent. In GT-HEAT, while the system was assumed to produce zero net thrust in descent, the FAs were constrained to consume as much power as the TGs produced because the BP was not allowed to be charged. The maps developed for tMAPS utilized a decoupled model of the propulsion system components, and the lower bound of operation of each component was shifted. Thus, idle power output and input of the TGs and FAs, respectively, were reduced. Further, charging is allowed in tMAPS, which enables independent control of the TGs and FAs in descent, subject to the operating limits of the BESS.

Table 3.3: Error between GT-HEAT and tMAPS in climb and cruise of missions ranging from 550 to 2370 km and takeoff weight ranging from 27 to 34 mt; percent RMSE is normalized by the mean theoretical (GT-HEAT) value of the same variable, except percent error in fuel savings is relative to the fuel consumption

| | BESS Power | | | | Root Mean Square Error | | | | | | | | Absolute Error | | | |
| | Climb | Cruise | D | | F_{tot} | | P_f | | P_{trbF} | | Fuel Burn | | Fuel Savings | |
Range [km]	[%]	[%]	[N]	[%]	[N]	[%]	[kW]	[%]	[kW]	[%]	[kg]	[%]	[kg]	[%]
550	0	0	125	0.81	422	1.58	130	1.96	139	1.94	9	1.49	-	-
550	15	0	173	1.09	489	1.75	143	2.03	134	1.95	8	1.35	1	0.25
550	30	0	232	1.44	594	2.05	165	2.20	137	2.04	6	1.12	3	0.58
550	0	15	129	0.83	430	1.59	131	1.95	139	2.00	9	1.50	0	0.03
550	15	15	178	1.11	497	1.75	143	1.99	130	1.98	7	1.30	2	0.36
550	30	15	240	1.47	596	2.01	162	2.12	131	2.09	5	0.99	4	0.80
550	0	30	136	0.86	443	1.62	133	1.96	139	2.08	9	1.47	1	0.09
550	15	30	184	1.14	502	1.74	142	1.95	127	2.04	6	1.18	3	0.55
550	30	30	243	1.47	598	1.98	161	2.06	128	2.17	5	0.91	5	0.98
550	0	45	138	0.87	444	1.61	133	1.94	140	2.15	9	1.50	1	0.11
550	15	45	191	1.17	510	1.74	142	1.91	128	2.16	6	1.15	3	0.65
550	30	45	249	1.48	613	1.99	164	2.06	129	2.36	4	0.91	5	1.08
1100	0	0	96	0.60	288	1.35	105	1.80	112	1.79	20	1.60	-	-
1100	15	0	133	0.81	326	1.49	110	1.83	106	1.72	18	1.48	2	0.17
1100	30	0	178	1.07	384	1.71	117	1.89	102	1.68	15	1.29	5	0.41
1100	0	15	107	0.64	296	1.33	100	1.67	102	1.74	18	1.47	2	0.21
1100	15	15	140	0.82	339	1.47	104	1.65	94	1.63	15	1.27	5	0.48
1100	30	15	196	1.12	424	1.79	122	1.86	98	1.74	13	1.16	7	0.64
1100	0	30	108	0.63	307	1.33	99	1.60	101	1.82	16	1.41	4	0.33
1100	15	30	148	0.83	369	1.53	109	1.65	96	1.80	14	1.25	6	0.59
1100	30	30	201	1.09	445	1.77	121	1.74	96	1.83	10	0.98	10	0.93
1100	0	45	112	0.63	331	1.39	105	1.64	107	2.03	16	1.47	4	0.34
1100	15	45	149	0.79	391	1.54	110	1.60	98	1.97	13	1.22	7	0.71
1850	0	0	82	0.49	224	1.14	94	1.70	100	1.67	34	1.62	-	-
1850	15	0	110	0.65	250	1.24	94	1.66	92	1.56	30	1.49	3	0.16
1850	30	0	150	0.88	298	1.46	97	1.67	87	1.47	26	1.30	8	0.37
1850	0	15	88	0.50	246	1.17	89	1.50	90	1.59	29	1.42	5	0.25
1850	15	15	119	0.65	283	1.29	90	1.46	82	1.44	24	1.20	10	0.51
1850	30	15	163	0.87	352	1.55	101	1.56	81	1.44	20	1.01	14	0.72
1850	0	30	93	0.49	274	1.21	90	1.43	92	1.67	27	1.35	7	0.35
2370	0	0	73	0.44	194	1.01	89	1.63	94	1.60	44	1.61	-	-
2370	15	0	98	0.58	217	1.11	87	1.55	85	1.45	39	1.45	5	0.18
2370	30	0	137	0.79	265	1.33	90	1.58	82	1.40	35	1.30	9	0.34
2370	0	15	80	0.43	224	1.06	82	1.36	82	1.44	35	1.29	9	0.34
2370	15	15	104	0.54	271	1.21	87	1.38	78	1.36	31	1.16	13	0.48
2370	30	15	149	0.74	334	1.44	99	1.49	80	1.37	28	1.05	16	0.60
2370	0	30	82	0.42	260	1.16	93	1.47	94	1.69	39	1.44	5	0.20
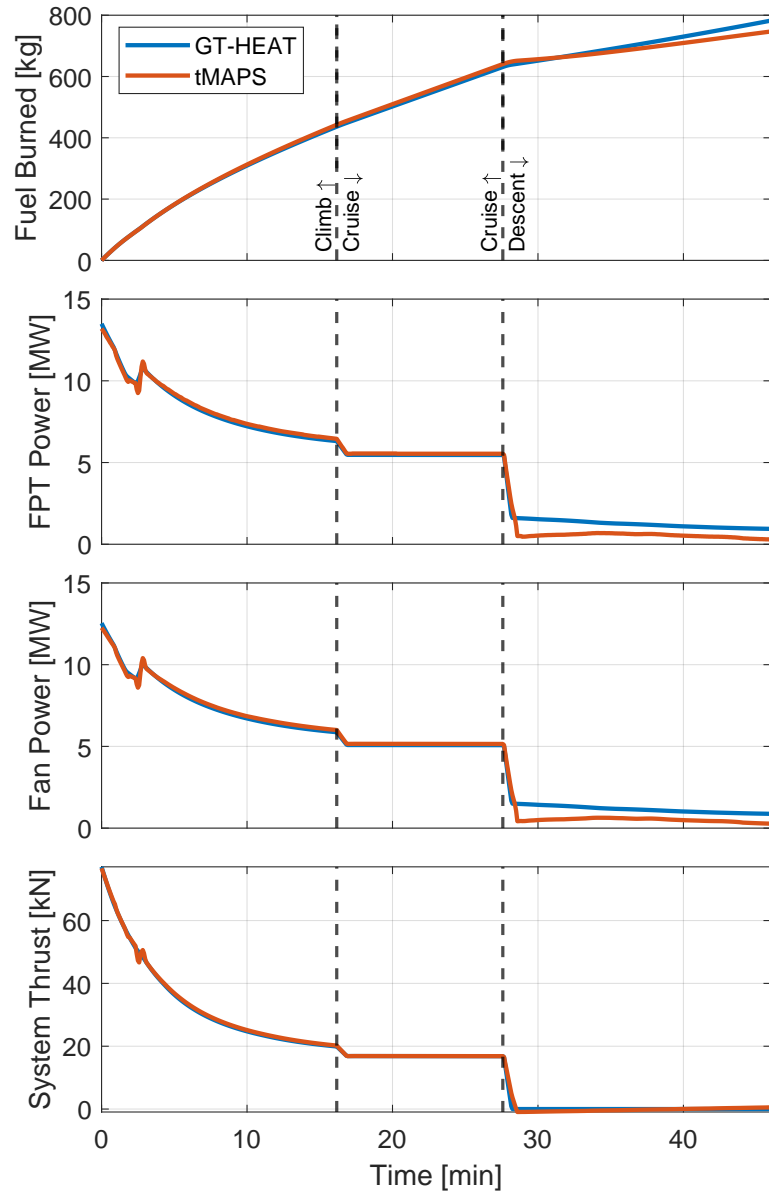
Figure 3.12: tMAPS model validation of the TEDP baseline aircraft over a 550 km mission

74

Chapter 4: Design Space Exploration

4.1 Optimization Framework

The model architecture presented was used to investigate how design factors such as cell chemistry and BESS size and external inputs, i.e. the mission profile, impact the power split, between the TGs and ESS, and the fuel consumption. In the presence of a hybrid powertrain, the design optimization problem includes two sub-problems, one in the design space and one in the control space. To objectively compare two designs for optimality, the optimal control of each design must be considered. Additionally, with variations to the inputs or disturbances, the optimal design and control must be re-evaluated. No one set of rules is sufficient to fully exploit the system's capabilities with the non-linearity introduced through simultaneous variation of its design and inputs; thus, DP is applied to the optimal control problem. The deterministic DP algorithm was developed and implemented in [61] for the purpose of solving the problem of optimal control of non-causal, non-linear, time-variant, constrained, discrete-time models, such as the one presented here, and has frequently and successfully been applied to the HEV energy management problem. Exhaustive search is sufficient to evaluate the design space because the limited number of design and input variations: six cell technologies, three mission profiles, and BESS size limited by the MTOW.

4.1.1 Optimal Control Problem

The optimal energy management for an HEV is formulated by optimizing the power split between the TGs and ESS such that the fuel consumption, described in Equation 3.9, is minimized. The power split is defined in Equation 3.18 but is controlled through the engine speed ratio (practically the engine power level) in Equation 3.9 and constrained by the prescribed mission profile (Equation 3.8) and corresponding fan power requirement (Equation 3.13). The continuous time optimal control problem is written mathematically as follows:

$$
\begin{aligned}
\min_{u(t)} \quad & J(u(t)) \\
\text{s.t.} \quad & \dot{x}(t) = f(x(t), u(t), t) \\
& x(0) = x_0 \\
& x(t_f) \in [x_f^m, x_f^M] \\
& x(t) \in X(t) \subset \mathbb{R}^p \\
& u(t) \in \mathcal{U}(t) \subset \mathbb{R}^q
\end{aligned}
\tag{4.1}
$$

where x and u are state and control variables, x_0 is an initial state value, x_f^m and x_f^M are minimum and maximum final state values, X and $\mathcal{U}$ are the admissible state and control spaces, p and q are the number of states and control variables, and

$$
J(u(t)) = G(x(t_f)) + \int_{t=0}^{t_f} H(x(t), u(t), t) \Delta t
\tag{4.2}
$$

where J is the cost functional, G is the terminal cost, and H is the cost-to-go.

To solve the problem using DP, Equation 4.1 must be discretized. DP is based on Bellman's principle of optimality: "An optimal policy has the property, that whatever the initial state and initial decisions are, the remaining decisions must constitute an optimal policy with regard to the state resulting from the first decision" [73]. The DP algorithm

76

relies on backward recursion and knowledge of future reference inputs and disturbances to evaluate and minimize the cost implied by future decisions given the initial states [61]. Practically, the time space must be discretized to constrain the number of computations. Further, the state and control space must be discretized in order to evaluate the "cost-to-go," or cost associated with a given state transition for a given control signal at a given time, without knowledge of initial decisions, as the algorithm works backwards in time [61]. While discretization of the state and control spaces impacts accuracy and computational time, only discretization of the time space impacts the problem formulation. The discrete time optimal control problem takes the form:

$$
\begin{aligned}
\min_{u^k} \quad & G(\chi^K) + \sum_{k=0}^{K-1} H(\chi^k, u^k) \\
\text{s.t.} \quad & \dot{\chi}^k = f(\chi^k, u^k) \\
& \chi^{(0)} = \chi_0 \\
& \chi^K \in [\chi_m^K, \chi_M^K] \\
& \chi^k \in X^k \subset \mathbb{R}^p \\
& u^k \in \mathcal{U}^k \subset \mathbb{R}^q
\end{aligned}
\tag{4.3}
$$

No terminal cost is used, and the cost-go-to is equal to the fuel consumed (Equation 3.9). At most, two state variables ($p = 2$) and one control variable ($q = 1$) are considered. The two state variables χ_1 and χ_2, SOC and fuel mass, respectively, vary according to Equations 3.10 and 3.24. Upper and lower SOC bounds are defined as 95% and 10%, across which cell performance is least limited, and SOC is initialized at its upper bound. Fuel mass is constrained to be between the initial fuel mass and reserve mission fuel mass requirement, both of which are estimated following the process described in Section 4.1.3. The control variable is the speed ratio, as described in Section 3.2.2. Thus, the optimal control problem

written specifically for this system is as follows:

$$\min_{u^k} \sum_{k=0}^{K-1} \dot{m}_{fuel}^k \Delta t$$

$$\text{s.t.} \quad \dot{x}_1^k = -\frac{I_{cell}^k}{C_{nom}} \qquad \dot{x}_2^k = f(\text{MN}^k, z^k, r_N^k)$$

$$x_1^{(0)} = 0.95 \qquad x_2^{(0)} = m_{fuel,init}$$

$$x_1^K \in [0.10, 0.95] \qquad x_2^K \in [m_{fuel,res}, m_{fuel,init}] \tag{4.4}$$

$$x_1^k \in [0.10, 0.95] \qquad x_2^k \in [m_{fuel,res}, m_{fuel,init}]$$

$$u^k \in \{u \in \mathbb{R} \mid 0.45 \le r_N^k \le 1.00, \ P_{cell,M-}^k \le P_{cell}^k \le P_{cell,M+}^k, \cdots$$

$$I_{cell}^{M-} \le I_{cell}^k \le I_{cell}^{M+}, \ V_{cell}^m \le V_{cell}^k \le V_{cell}^M\}$$

The engine design is fixed; thus, the speed ratio limits are fixed. The cell power, current, and voltage limits vary for every cell candidate. The power limits are also dependent on SOC and, hence, vary in time.

4.1.2 Fuel Mass Sensitivity Study

A sensitivity analysis was performed to evaluate the impact of fuel mass variation on the overall aircraft performance with the aim of further reducing the model complexity and, consequently, computational time, which is exponential in the number of states and controls. In this analysis, a set of missions was simulated with and without fuel mass as a state. With and without the fuel mass being updated, the amount of fuel consumed was compared for the TEDP architecture across multiple mission ranges in Table 4.1. Missions of the same range were initialized with the same fuel and payload mass for the variable and constant mass scenarios

The analysis determined that fuel mass tracking will have a very small impact on the estimated fuel consumption. This is a result of the fuel mass being a small percentage

Table 4.1: Model sensitivity to fuel mass variation

Mission Range	Fuel Consumption [kg]		Error	Error
[km]	Variable m_{fuel}	Constant m_{fuel}	[kg]	[%]
550	649.7	652.4	2.7	0.4
1100	1265.2	1272.8	7.6	0.6
1850	2091.6	2110.6	9.0	0.4

of the overall system mass. As the level of hybridization of the aircraft increases, the overall system mass will increase, while the amount of fuel consumed will decrease, further reducing the impact of fuel mass tracking and resulting in the vehicle mass staying relatively constant over the mission. This allows for the removal of fuel mass as a state for the future optimization analysis. The fuel mass trajectory is still book-kept and can be corrected *a posteriori*.

4.1.3 Fuel Mass Initialization and Estimation

The full mission profile consists of a primary and reserve mission profile. The reserve mission profile ensures the aircraft has enough energy on-board to react appropriately to an emergency when attempting to land. The battery pack is not considered a critical component in the propulsion system; thus, the reserve mission propulsive power is supplied solely by the TGs. The fuel mass estimation process is illustrated in Figure 4.1.

Because the system is determined when simulating the reserve mission, only Stage 1 is required to estimate the reserve fuel mass. When evaluating the fuel required for the reserve mission, the target final fuel mass is zero. Then, when evaluating the primary mission fuel requirement, the target final fuel mass is equal to the reserve fuel mass. Stage 1 simply shifts
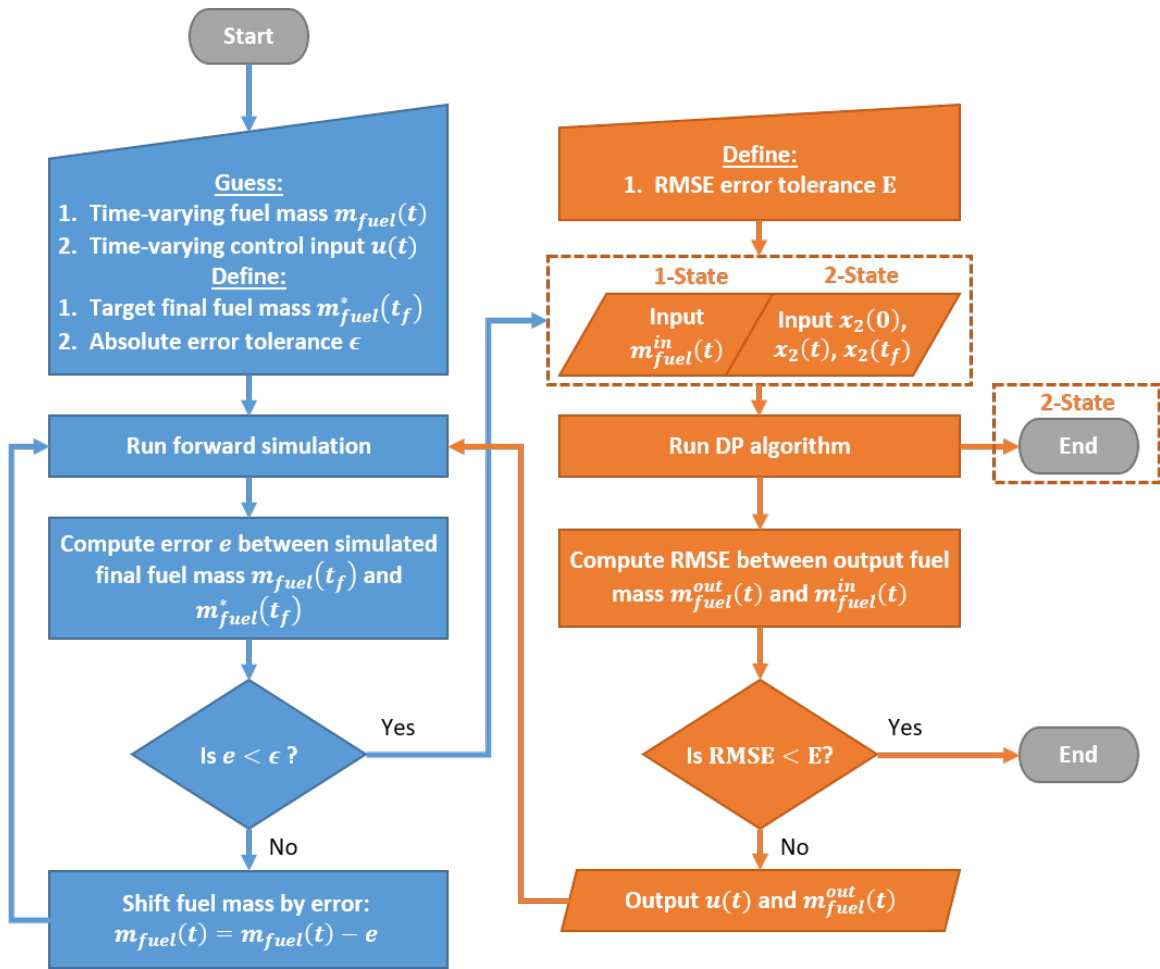
Figure 4.1: Process for estimating time-varying fuel mass with Stage 1 in blue (left) and Stage 2 in orange (right)

the fuel mass trajectory by the error between the target and final fuel mass, while Stage 2 re-evaluates the trajectory.

Both stages are required to initialize and estimate fuel consumption for the primary mission. Without knowledge of the optimal control *a priori*, the TEDP system must be used in Stage 1 to initialize the state value and limits for DP in Stage 2. Using the TEDP system simulation results to initialize the HEDP system generally ensures the state constraints are not violated because fuel consumption is reduced, while carrying the additional fuel mass has been shown to have negligible impact. When fuel mass is considered as a state, in the 2-State case, the outputs from the DP algorithm are the final results. When SOC is the only state, convergence of the fuel mass trajectory is evaluated via the root-mean-square error to ensure any impact the fuel mass trajectory has on the optimal control is captured.
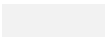
4.1.4   Convergence Study
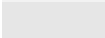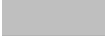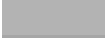
The DP algorithm only evaluates the cost-to-go on discretized points in the state space. At each instance of time, the system is "initialized" at every combination of feasible state values, every feasible control is applied to the system at these states, and the "cost-to-go" associated with the transition to the next set of states is computed. The cost-to-go is tabulated to create a cost matrix for later interpolation. The number of points evaluated, i.e. the discretization of the state and control values, directly affects the accuracy of the solution and its computation time.

A convergence study was conducted to determine the best compromise between accuracy and computation time with and without fuel mass as a state and with and without the fuel mass trajectory being updated. More explicitly, the models are described in the following:

- Model 1 - One state, SOC, and one control, speed ratio, with fuel mass held constant and equal to the reserve mission fuel plus the TEDP system primary mission fuel

- Model 2 - One state, SOC, and one control, speed ratio, with fuel mass updated per Figure 4.1

- Model 3 - Two states, SOC and fuel mass, and one control, speed ratio, with fuel mass initialized per Figure 4.1

The models were studied with grid sizes according to Table 4.2. Model 3 was studied last and the sizes of the SOC and control grids were guided by the studies performed on Models 1 and 2. Computation time limited the refinement of grids used for Model 3. Mission B and

Table 4.2: Grid sizing used in the convergence study

| Color | Models 1 and 2 | | Model 3 | | |
	x_1	u	x_1	x_2	u
	25	25	100	50	25
	25	50	100	100	25
	25	100	100	200	25
	25	200	100	400	25
	25	400	100	50	50
	25	800	100	100	50
	50	25	100	200	50
	50	50	100	400	50
	$\vdots$	$\vdots$	$\vdots$	$\vdots$	$\vdots$
	800	800	400	400	100

the reserve mission profile described in Table 4.3) were used for the convergence study. An energy model was used to model the BESS to eliminate the chance of cell characteristics

influencing the results. The BESS was sized with 200 Wh/kg energy density and 3500 kg mass. No other parameters were varied from those defined in Section 3.3.

Error in the DOD and fuel consumption and total computation time are shown as functions of each individual grid dimension in Figure 4.2. The line follows the mean error related to a particular grid dimension, while the standard deviation captures the influence of the other dimensions. The more steep the slope of the line, the greater the influence of the particular dimension. The larger the standard deviation bar, the larger the influence of the other dimensions. Convergence of both the error and standard deviation indicate strong dependence on the particular dimension. Independently refining the grid of State 1 reduces the error and standard deviation for both states. Refining State 2 neither significantly impacts the error, nor the standard deviation. The error and standard deviation are relatively weakly affected by refinement of the control, and the standard deviation is significantly larger. Error in fuel consumption is slightly improved over that of Model 1 with the inclusion of fuel mass as an external input in Model 2 at negligible cost in computation time. There is practically no difference in error when adding the second state variable; in fact, DOD error is increased because refinement of the State 1 grid is limited. Meanwhile, Model 3 performs relatively poorly considering computation time.

It is necessary to include fuel mass as an external input because it impacts the stability of the solution, as shown in Figure 4.3. While Model 1 offers comparable accuracy to estimate fuel consumption, the optimal trajectory is not truly representative of the system. The fuel mass trajectory shows little difference because it holds significantly more energy and has slower dynamics; however, clearly the SOC trajectory does not converge with grid refinement, using Model 1. Added in Model 2, iteratively updating the fuel mass input not only stabilizes the control but also results in a trajectory that closely matches that of
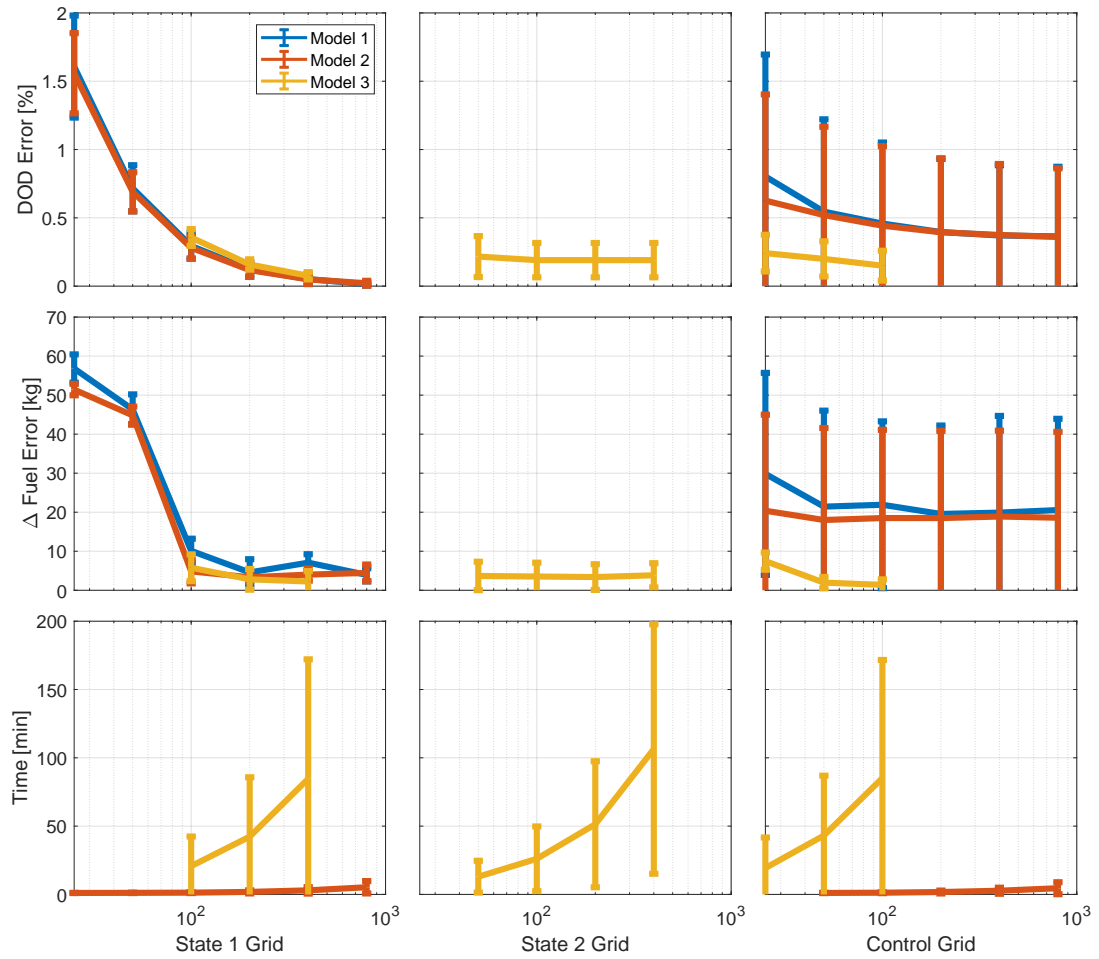
Figure 4.2: Error convergence behavior and computation time of the DP algorithm as a function of state space grid size (MATLAB R2019b, Windows 10, 2.20 GHz Intel Xeon E5-2630 v4 CPU, 16.0 GB RAM)

Model 3. The ability to re-initialize the DP algorithm actually enables Model 2 to achieve reduced fuel consumption, especially in situations when the BESS design offers potential for significant reduction in fuel consumption.
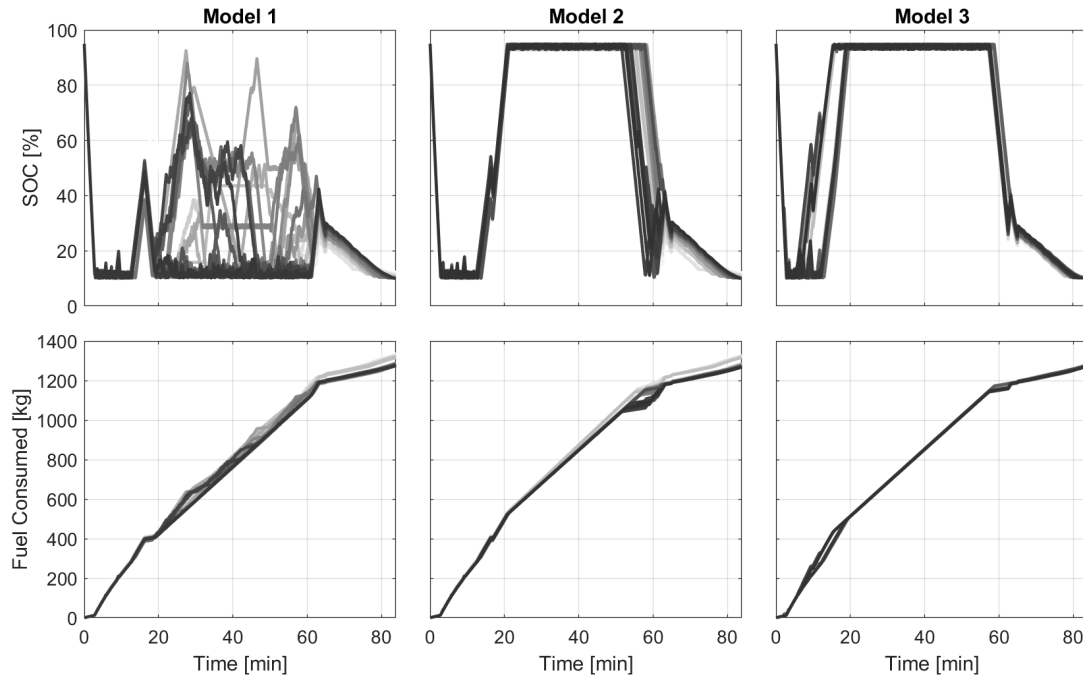
Figure 4.3: State trajectory convergence behavior as a function of state space grid size, refer to Table 4.2 as a legend

4.2 Results and Analysis

The missions evaluated in the case study include ranges of approximately 550, 1100, and 1850 km, representing missions A, B, and C, respectively, are summarized in Table 4.3 and shown in Figure 4.4. The profiles do not explicitly include takeoff or landing rolls but, rather, begin in initial climb and end in approach. The reserve mission is not considered in

the reported fuel burn and fuel savings but is used to initialize the mass of fuel in the aircraft, as described in Section 4.1.3.

Table 4.3: Summary of primary and reserve mission profiles

| | | Mission | | | |
		A	B	C	Reserve
Overall	Time [min]	45.7	83.9	134.4	27.3
	Range [km]	550	1100	1850	275
Climb	Initial Cond.	0.31 Mach, 200 m			0.30 Mach, 140 m
	Time [min]	12.8	15.3	18.0	6.5
	Range [km]	156	190	235	67
Cruise	Condition	0.80 Mach, 9.1 km			0.63 Mach, 6.1 km
	Time [min]	13.9	47.2	93.3	5.9
	Range [km]	200	705	1401	82
Descent	Final Cond.	0.32 Mach, 400 m			0.30 Mach, 140 m
	Time [min]	19.0	21.4	23.1	14.9
	Range [km]	194	205	214	126

One state and one control are used in the optimization; the problem formulation is the same as described in Equation 4.4 without x_2 and was referred to as Model 2 in Section 4.1.4. The model was calibrated according to Section 3.3, and the fuel savings reported is relative to the TEDP system. The BESS in the HEDP system is increased in size from 1.0 mt to the maximum allowable by the MTOW and fuel mass, which varies for each mission. The fuel consumed by the TEDP system was referenced to limit the BESS size. The state was discretized using 300 points, which is equivalent to 0.28% SOC, and the control was discretized using 300 points, which is equivalent to 0.18% LPC speed. The mission profile was discretized using 5 second time steps.
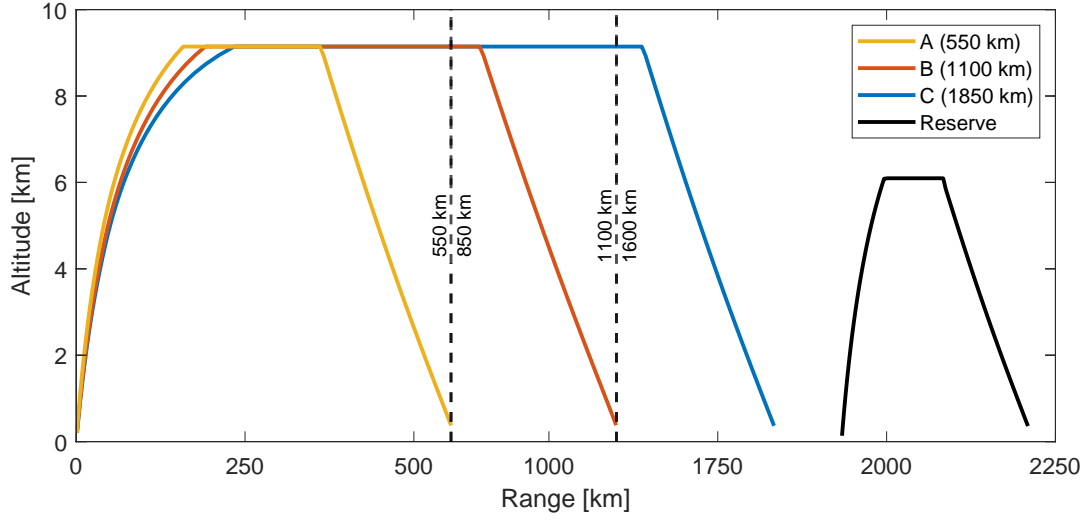
Figure 4.4: Primary and reserve mission profiles

4.2.1 Time-Domain Analysis

Here, the influence of each of the three independent variables – mission range, BESS size, and cell selection – are isolated from one another to analyze the individual impact on the power split and energy efficiency. The power split is defined as

$$
\text{PS} =
\begin{cases}
\frac{P_{BESS}}{P_{TG,tot} + P_{BESS}} & P_{BESS} \geq 0 \\
\frac{-P_{BESS}}{P_{FA,tot} - P_{BESS}} & P_{BESS} < 0
\end{cases}
\tag{4.5}
$$

Thus, when discharging, the power split defines the percent of power supplied by the BESS to power the FA, and, when charging, it defines the percent of power consumed by the BESS. Both modes are considered also in the total conversion efficiency, from chemical to electrical energy, defined as

$$
\eta_{tot} =
\begin{cases}
\frac{n_f \cdot P_f}{\text{LHV} \cdot n_{TG} \cdot \dot{m}_{fuel} + P_{BP}} & P_{BP} \geq 0 \\
\frac{n_f P_f - P_{BP}}{\text{LHV} \cdot n_{TG} \cdot \dot{m}_{fuel}} & P_{BP} < 0
\end{cases}
\tag{4.6}
$$

where LHV is the lower heating value of jet fuel, 43.1 MJ/kg.

87

Figure 4.5 illustrates optimal control variation related to the mission range for Cell 3 and a 4.0 mt BESS. The x-axis displays the percent completion of each mission segment to normalize the varying time. The climb and descent segments of all missions and the cruise segment of Mission A are practically the same duration, whereas the normalization renders the cruise segments of Missions B-C to appear relatively short in duration. Thus, the relative rate of change of the SOC is misleading, which is discussed later.

The baseline power consumption in climb is highest for Mission A because it is the fastest to climb to altitude and increases with the addition of a BESS because of the increased system mass. Power consumption reduces steadily throughout climb as the rate of climb reduces until the top of climb. While maintaining constant altitude in cruise, drag is the predominant resistive force, and power consumption is nearly equivalent between the baseline and hybrid (4.0 mt BESS) aircraft in all missions. Descent features a relatively short, "powered" phase at its start, which increases in duration with increasing range, before a longer "gliding" (zero thrust) phase concludes descent. Slight differences between the profiles result in visible but negligible differences in baseline power consumption when gliding, as the power consumption in descent is predominantly influenced by the powered phase.

Energy stored in the BESS is generally reserved for low-power operation due to battery power limits and engine efficiency trends; thus, the power split will analyzed starting in descent and working back to climb. When gliding, the system simply consumes the minimum fuel possible. Where the efficiency is reduced, the additional mass of the BESS reduces thrust (or increases drag) needed to follow the descent trajectory, reducing fuel consumption as engine and fan power is reduced. Mismatch in the engine power output and fan power input results in battery charging. When the FA must again produce some

non-zero thrust, in the latter half of descent, the battery power output is increased, rather than that of the engine, to slightly improve efficiency. The powered phase of descent is the first point at which both baseline power consumption and efficiency are reduced. Battery power output is increased as engine efficiency and FA power input decreases, significantly increasing efficiency for a short duration.

In cruise, the power split is relatively constant. Comparison to the power split in descent can be misleading without also referencing the total power consumption. Low baseline power consumption and engine efficiency increase the power split in cruise, relative to climb. Due to a combination of battery power limits and cruise duration, the power split and, consequently, the efficiency improvement is a small percentage but sustained over a long duration. The power split in cruise decreases with increasing mission range The ramp increase in the power split at the beginning of cruise occurs in the transition to level flight.

The duration of the climb segment compared to that of the full mission significantly impacts the power split in climb. In Mission A, when climb accounts for 28% of the mission, the power split increases as the power consumption decreases in climb. Note that the battery outputs more power at the beginning of climb. In general, the shorter the mission duration, the greater the average battery power output, all else the same. The increasing power split is influenced most by power consumption and mission duration and less by engine efficiency. In Missions B and C, climb only accounts for 18% and 13%, respectively, more energy is reserved for cruise, the average power split in climb decreases, and the power split decreases as engine efficiency peaks at the top of climb.

The relative rate of change of SOC shown is opposite to reality; SOC is depleted faster the shorter the mission duration, as indicated by the magnitudes of power consumption and heat generation. It is important to note the SOC at the transitions between segments, though.

89

It is clear that more energy is reserved for cruise and descent in the longer range missions. Interestingly, the SOC at the end of climb and end of cruise is practically equivalent in both Missions B and C, and, in all cases, the final SOC is the same. The SOC is not constrained to reach a final value of 10%, but charge depleting is the only optimal mode of operation in these cases.

The distribution of battery energy across a longer duration with few instances of relatively high power output significantly reduces TMS requirements. Heat generation closely resembles the relative power but is significantly influenced by the OCV, particularly when SOC drops below 50%. In Mission A, the battery power output at the start of climb (at 95% SOC) is equal to the that of impulse in descent (at 15% SOC), while the heat generation in descent twice that in climb. Similarly, in Missions B and C, the battery power output in climb is half that in descent, but the heat generation in descent is quadruple that in climb.

Reducing the size of the BESS practically impacts the optimal control in the same way as increasing the mission range. Optimal control of the BP is shown for Cell 3, Mission A, and BESS sizes of 1.0, 3.0 and 5.5 mt in Figure 4.6. Generally, the power consumption of the hybrid is increases with increasing BESS size throughout the mission, except for when gliding in descent as discussed previously. The fuel savings achieved both when powered and gliding are significant for the smallest BESS because of its limited use elsewhere. The power split remains relatively constant in climb and cruise, with the average battery output power increasing with increasing size and, consequently, increasing energy storage and power capability. The impulse at the beginning of descent increases primarily due to the increased power capability. Heat generation follows the trends mentioned previously, except the heat generation of the 1.0 mt BESS in the latter half of descent is non-negligible relative
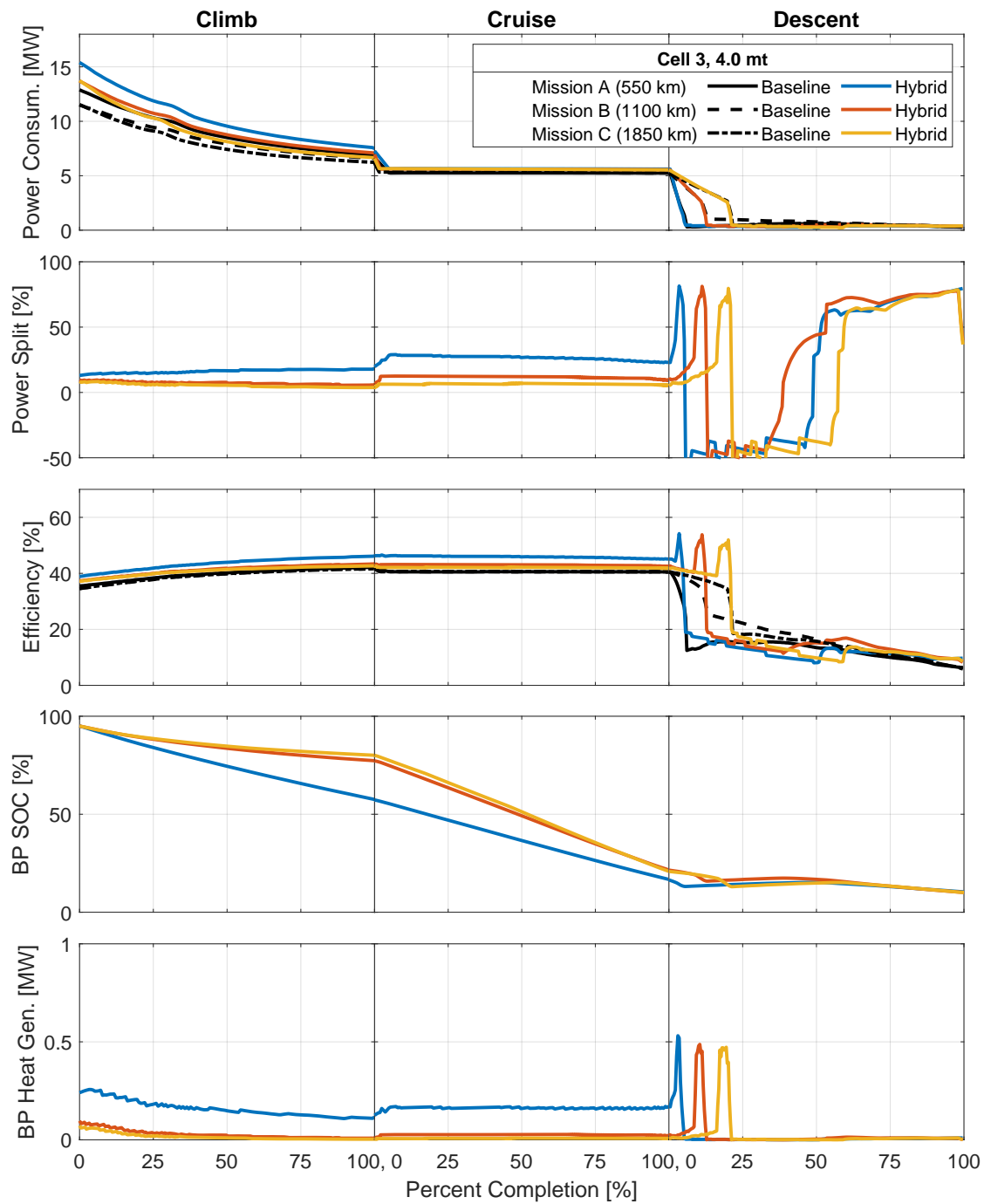
90

Figure 4.5: Battery pack state of charge, power split, and heat generation as a function of mission range (Cell 3, 4.0 t)

to its heat generation elsewhere. It may be considered negligible relative to that of the larger systems and depending on the sizing of the TMS.

Figure 4.7 compares the optimal control of a 5.0 mt BESS, Cells 1, 3, and 5, in Mission B. For the same size BESS and mission profile, the power consumption of the hybrid system is practically equal, regardless of cell selection and control variation. However, fan power input does increase with increasing battery power split, as engine thrust output decreases with decreasing power output. The power split for the majority of descent is independent of cell selection, though the peak power early in descent is dependent on the power capability of the cell.

The battery power output at the beginning of the mission increase with increasing power density; however, the initial power level is only sustained by the most energy-dense cell, which quickly surpasses the power output of Cells 1 and 3. The power split for every cell exhibits the step increase at the beginning of cruise and decreases throughout cruise, gradually for Cells 3 and 5 but in steps for Cell 1. As such, the SOC of every cell gradually diverges from each other throughout cruise. The higher the power density of the cell, the higher the SOC at the end of cruise and the sooner in time and larger the magnitude of the power impulse in descent. Following the power impulse, the SOC converges again and control is equivalent for the remainder of descent.

It is clear that the control exploits the power and current capability of Cell 1; however, relative to the performance of Cells 3 and 5, this capability is primarily detrimental to its performance. With increasing mission range, there is more flexibility in when to use the battery, but limited energy storage capability of the batteries results in low power operation to minimize losses due to internal resistance. A power-dense cell is better suited for a mission with disturbances that shift the engine away from its ideal operating point for short
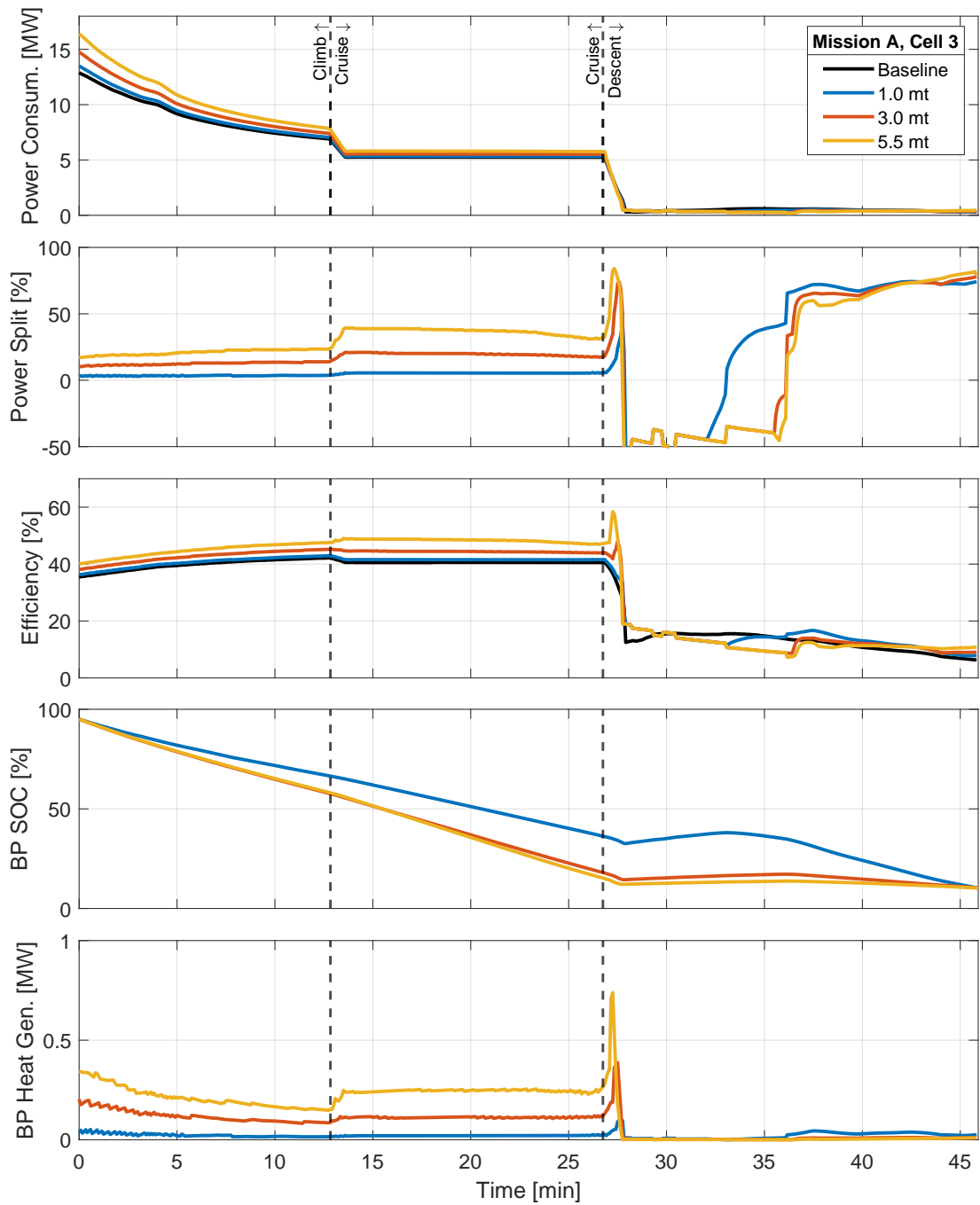
Figure 4.6: Battery pack state of charge, power split, and heat generation as a function of BESS size (Cell 3, Mission A)

periods of time. Lastly, because the sizing of the DC-to-DC converter depends on the peak power capability of the BP, the converter accounts for 10.6% of the BESS mass in a 5.0 mt BESS composed of Cell 1 compared to 3.5% when composed of Cell 5.

Figure 4.8 compares the optimal control of a 5.5 mt BESS, composed of the same cells, in Mission A. This example highlights the potential for power-dense cells and the limitation of energy-dense cells. Still, the hybrid power consumption is elevated relative to the baseline but is predominantly dependent on system mass, rather than cell selection and energy management. Now, the increased size of the BESS and reduced duration of the mission enabled the BESS with Cell 1 to provide 80% of the power to the FA resulting in 65% efficiency for a short duration in cruise, in addition to the highest peak power in descent. While there is clearly need for and benefit from high power capability, the BESS with Cell 3 enables the most fuel savings because it has sufficient power capability and higher energy storage capability.

Cell 5 is inhibited by its discharge current limit. The maximum discharge rate is 1C, meaning 60 minutes is required for a full discharge; however, in Mission A, there is practically less than 30 minutes in which the battery pack can be discharged. Further, Cell 5 generates significantly more heat during climb and cruise, even at lower power output due to the sizing of the BP. The maximum system voltage is fixed, and the maximum voltage of Cells 1 and 5, for example, are nearly equivalent. With approximately equal number of cells in series, the form factor of the cell determines the number of cells in parallel. The resulting pack architecture is 447s90p for Cell 5 and 476s222p for Sony. For the same power output, the current is then divided across fewer cells, also exhibiting higher internal resistance, resulting in higher losses and heat generation.
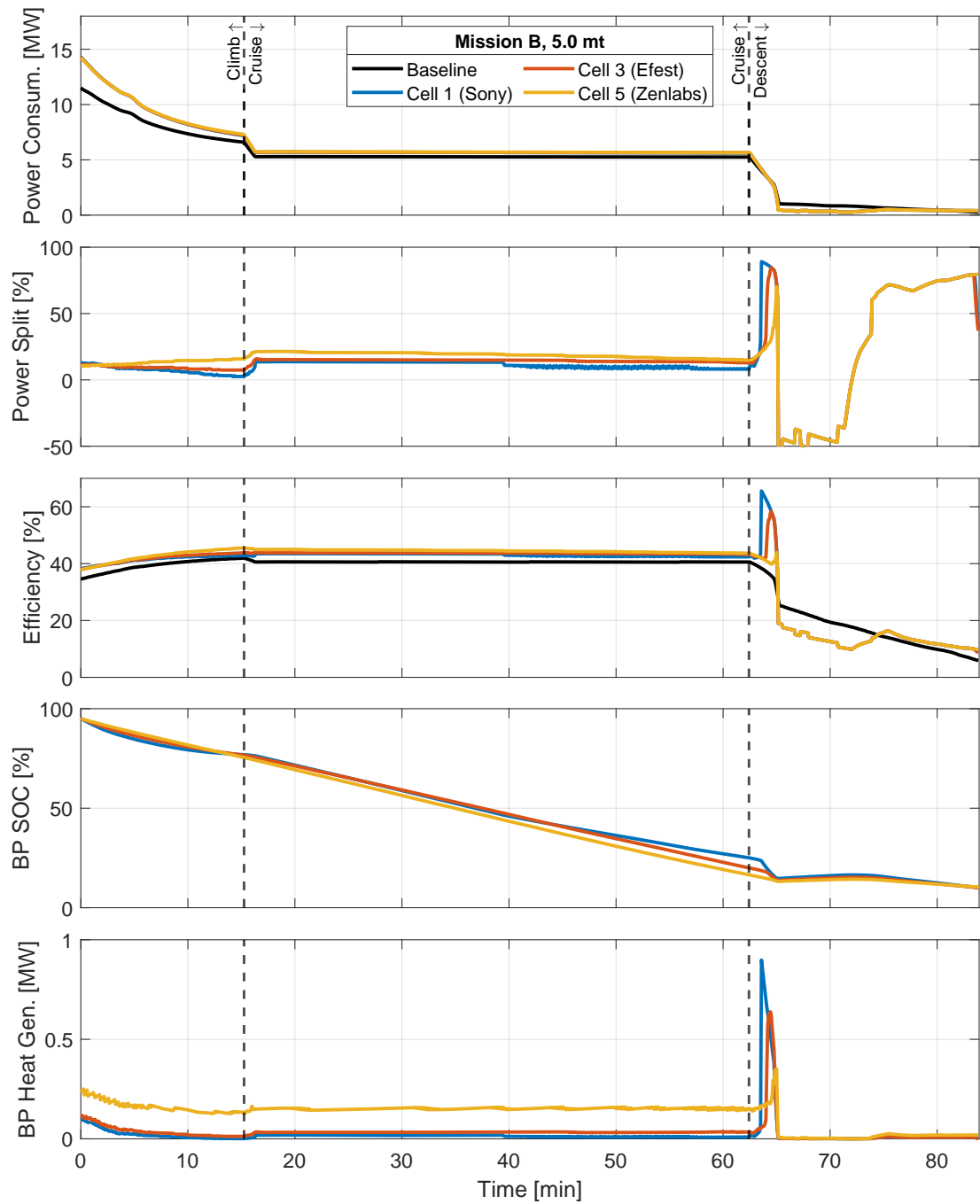
Figure 4.7: Battery pack state of charge, power split, and heat generation as a function of cell selection (5.0 t, Mission B)
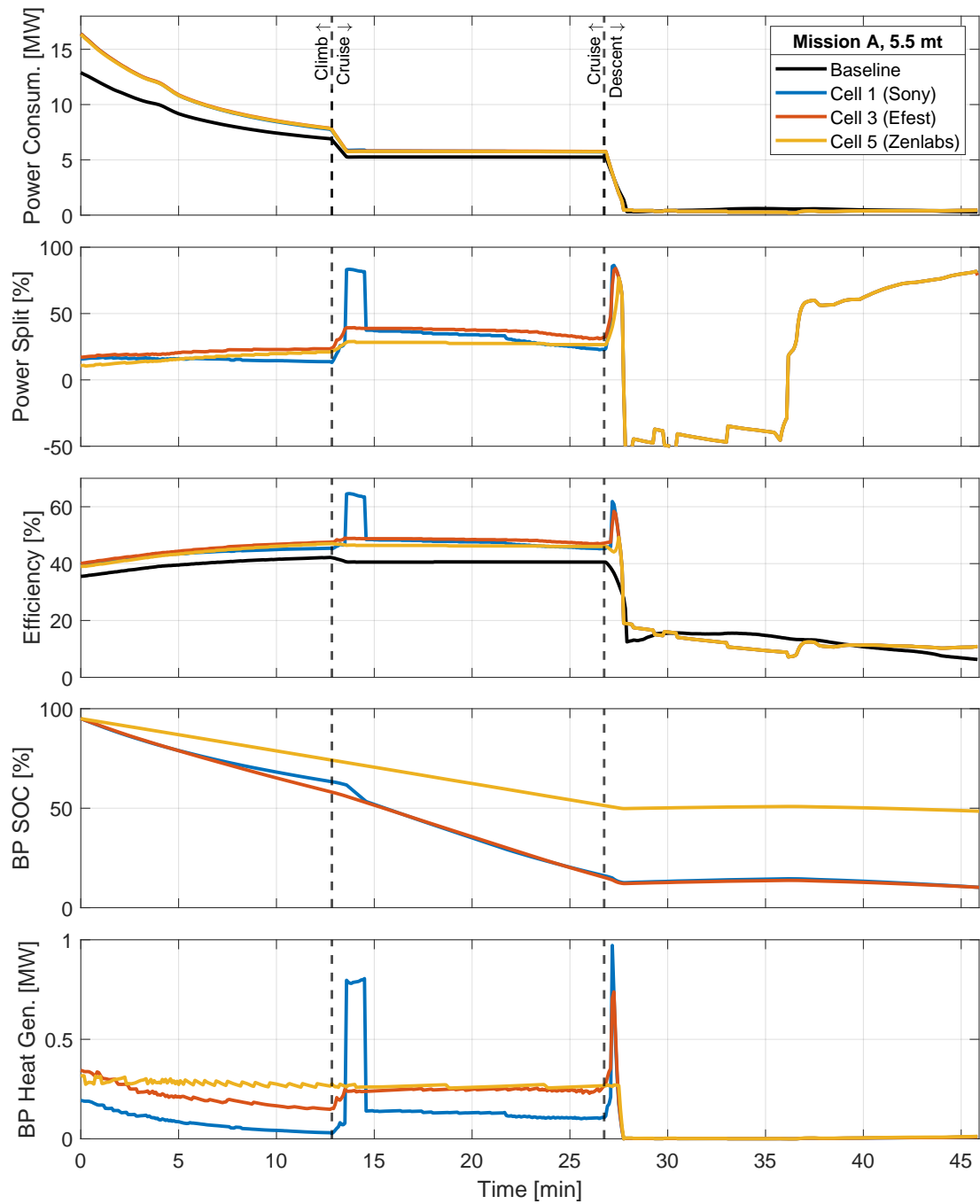
Figure 4.8: Battery pack state of charge, power split, and heat generation as a function of cell selection (5.5 t, Mission A)

4.2.2 Results Overview

Figure 4.9 shows how the segment and overall fuel savings varies between different cell selections in Missions A, B, and C with BESS sizes of 5.5, 5.0, and 4.0 mt, respectively. This figure again highlights the limitations of high-energy cells, Cells 5 and 6, in the short-range mission. All cells offer similar fuel savings in descent because of the low power request from the FA. In cruise, the savings using Cell 5 is significantly lower compared to that of Cells 1 and 3, which perform equally. The increased energy density of Cell 3 enables additional BP use in climb, resulting in the highest savings both in climb and overall.

With increasing mission range, BP use shifts towards the cruise and descent segments. Descent generally presents the best conditions in which to operate the BP, while increasing the mission range primarily increases cruise duration, range, and, consequently, fuel consumption. "On-off" control, i.e. either the engine or BP supplying the full FA power, is generally optimal because engine efficiency reduces significantly at partial power. However, even Cell 1 is prohibited from providing full FA power until the descent segment because of current limits.

Cell 1 is capable of providing the majority of FA power soonest in the descent segment, and its relatively poor performance in climb and cruise is both due to reserving energy for descent and starting with relatively low energy. Not only is Cell 1's energy density lower (and the BESS size is held constant), but also its high power capability requires a larger DC-to-DC-converter (Equation 3.36). The 5.5 mt BESS comprised of Cell 5 versus one of Cell 1 is capable of 3.9 MW and 11.7 MW of power output, increasing the mass of DC-to-DC converter from 193 kg to 585 kg, respectively.

Fuel savings increases with increasing range only for Cell 5 because its discharge current limit no longer inhibits the BP from being fully discharged. Otherwise, as range increases,

fuel consumption increases, likewise savings decreases, because overall energy expenditure begins to exceed the energy storage capability of the BP. In Missions B and C, average power output of a BESS designed with Cell 1 is actually lower than that of Cells 3 and 5, and its high power and current capability only inhibits its overall performance.
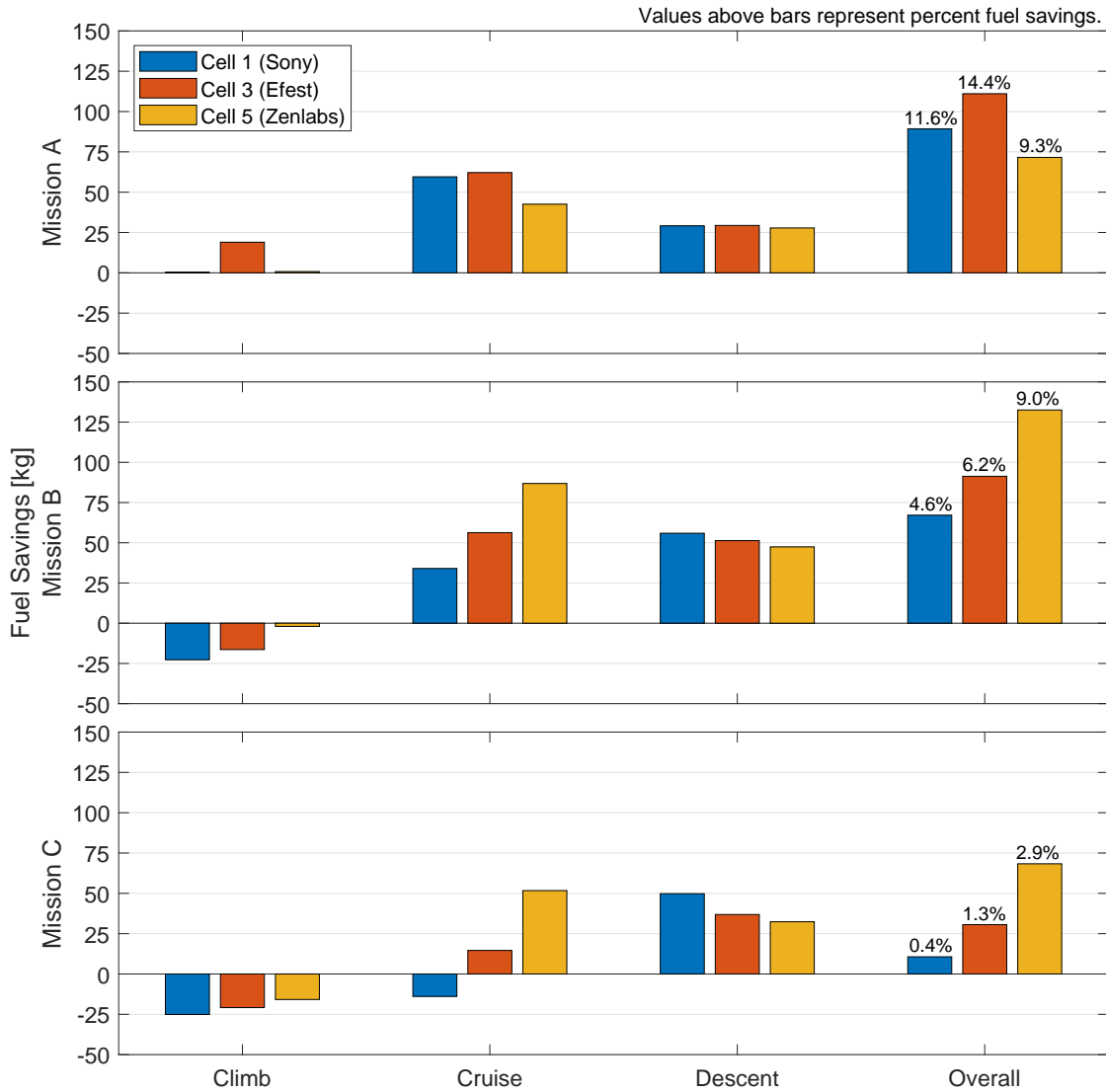

Figure 4.9: Fuel burn reduction, relative to the baseline, non-hybrid system, as a function of cell, range, and segment for the maximum allowable BESS size in each mission

Though there is a clear dependence on cell selection, Figure 4.10 shows there are strong trends in savings when neglecting cell-specific characteristics and, instead, when segregating by mission segment and range. Here, the savings is shown relative to the baseline, segment-specific fuel burn. While this perspective is slightly misleading, it highlights in which segment engine operation varies most from the baseline. It is misleading because, as mission range increases, the overall fuel savings is increasingly influenced by the savings in cruise. Cruise accounts for 30%, 56%, and 69% of the total mission duration and 36%, 64%, and 76% of the total mission range in Missions A-C, respectively.

Objective comparisons can be made between the same segment for different missions, except for in cruise. In all scenarios, the majority of capacity removed from the BP is done so in cruise. Further, the ratio of capacity removed in cruise increases with increasing mission range. Regardless, as range increases, the BP becomes energy limited, i.e. the overall energy required to carry the additional system mass exceeds the amount of energy stored in the BP. In Mission C, engine operation and fuel consumption vary only slightly from the baseline, i.e. the BP is barely capable of storing enough energy to compensate for its own mass. The increasing variance with increasing BESS size in Missions B and C is due to differences in energy storage capability, while, in Mission A, it is driven by differences in power capability.

Regardless of cell selection, BESS size, or mission range, engine operation varies most in descent. Consider the three segments of the simplified mission profiles to represent areas of high, moderate, and low-power demand. The results do not necessarily represent when in time the BP should be used but rather at what power level is optimal, which is influenced equally by both BESS and TG sizing and design. With increasing range, more energy is reserved for the cruise and descent segments, increasing savings in descent in Mission B

relative to that of Mission A. Mission C has a slightly longer descent segment but a smaller ratio of time spent gliding, causing a net decrease in savings in descent relative to that of Mission B.

Only for the shortest range mission allows for fuel savings in climb. With increasing size, on average, savings is further increased until the transition between the 5.0 and 5.5 mt BESS, at which point the additional energy is reserved for cruise. This is relatively nonlinear behavior relative to that of the other profiles and segments. In Missions B and C, the optimal BP power in climb is insufficient to negate the increased energy required to climb, and fuel burn increases with increasing BESS size. Further, fuel burn in climb increases with increasing mission range for the same BESS size, again, as the BP is utilized more in cruise and descent.

The many different dimensions presented in Figure 4.11 allow for comparison of aggregate data for all cells and missions with the BESS sized optimally for each. As mission range and baseline fuel consumption increase, the maximum allowable BESS size is reduced regardless of cell selection. Thus, for all cells, the BESS size decreases with increasing range. Cells 3-6 have sufficient system-level energy density to be sized at the maximum allowable size across all missions. The optimal BESS size for Mission C reduces progressively from Cell 3 to 1 as energy density decreases. Generally, fuel savings decreases with increasing mission range as overall energy expenditure increases and energy storage capability decreases. Practically, the fuel savings is a function of the capacity removed from the BP, and capacity is dependent on sizing and energy density. Lower energy density results in lower energy stored for the same BESS size, and DC-to-DC converter sizing compounds this effect, as power density generally increases with decreasing energy density. In Mission A, the BPs using Cells 4 and 6 have more installed capacity than those for Missions B and
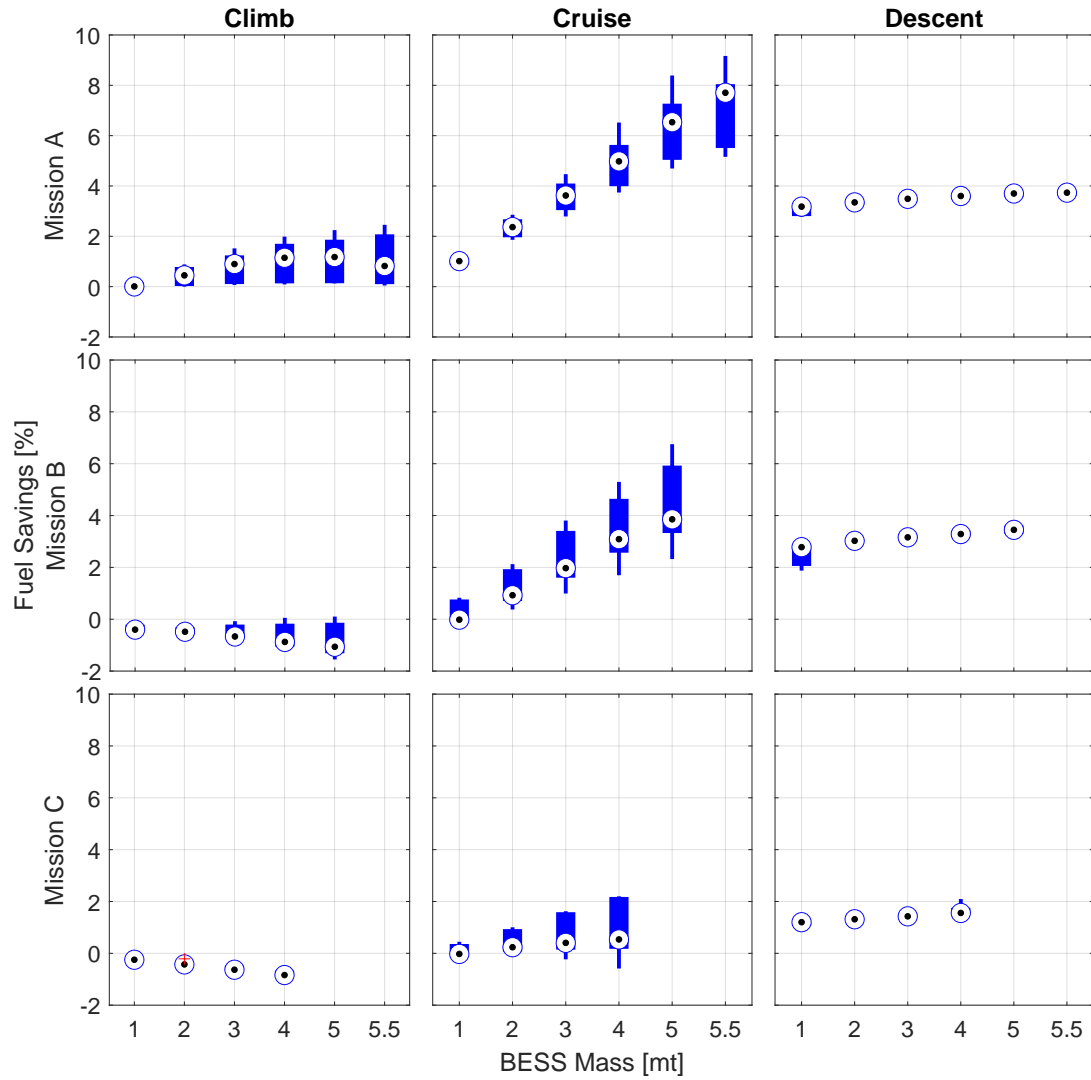
Figure 4.10: Segment-specific fuel burn reduction, relative to the baseline, non-hybrid system, as a function of BESS size and mission range; averages are denoted by the dot, cell-to-cell performance variation is captured by the bars and whiskers

C; however, current limits prevent the full capacity from being removed. These are the only instances where capacity output is not proportional to BESS size.

Given that the cell is not limited, for the same mission, mean discharge power increases with increasing energy density simply because more energy must be discharged in the same duration. Further, and more interestingly, the mean discharge rate is practically the same for every cell for a given mission. This is primarily due to the smoothness of the mission profiles. If the profile contained large variations in thrust request corresponding to steps in altitude changes, the BP would be discharged in pulses at differing magnitude and duration corresponding to the power capability of the BP. Mean heat generation is a function of mean discharge power (and charge power, which is negligible), cell internal resistance, and pack architecture. Cells 1 and 2 have equivalent mean discharge power and heat generation, while Cell 2 exhibits one-third the internal resistance and has four times the capacity of Cell 1. Remember that Cells 4 and 6 were the only cells not experimentally characterized, and the internal resistance used and heat generation computed are lower than would be expected.

Peak discharge power, discharge rate, and heat generation are most influenced by cell parameters and BESS size, otherwise having no dependence on mission range. The cells with the highest power and current limits (by unit mass), Cells 1 and 3, exhibit the highest peak power, rate, and heat generation. Current and power limits can vary somewhat independently such that the relative scale of peak discharge rate and power vary accordingly. Generally, these both decrease with increasing energy density, while peak heat generation is additionally governed by internal resistance and voltage range.

Considering the same mission and BESS size, generally, fuel savings increases with increasing cell energy density. This assumes that cell limitations do not impair the BESS for a significant portion of the mission and neglects any differences in packaging efficiency
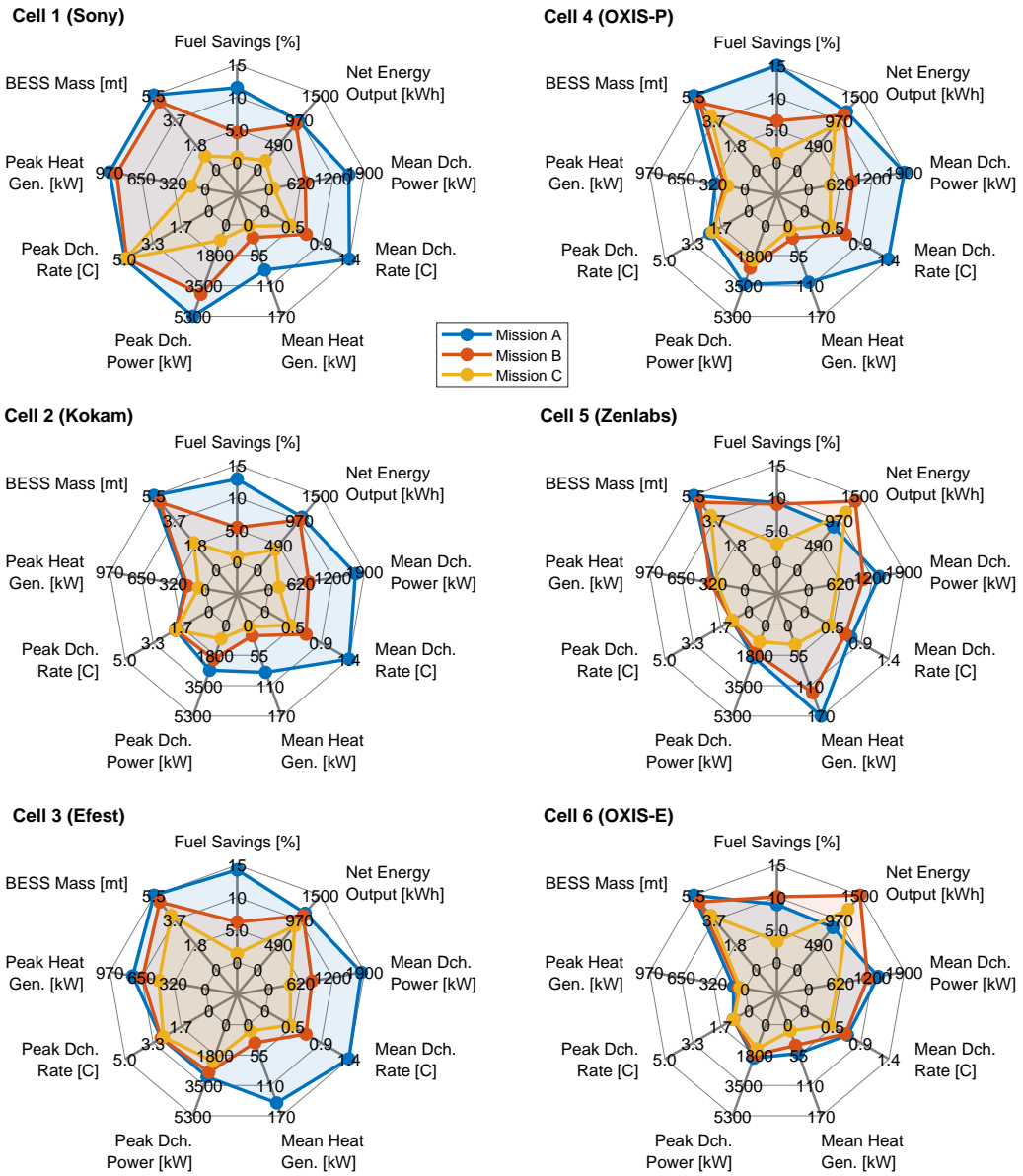
Figure 4.11: Comparison of key BESS performance metrics for every combination of cell selection and BESS sizing that minimizes fuel consumption in each mission

between cells of different form factors. For example, Figure 4.12 shows the two most energy-dense cells suffer in performance in Mission A because the duration of the mission and current limits prevent the BP from being fully discharged. Shorter range missions require highly power-dense cells, or cells with higher allowable discharge current. Still, increasing the size of the BESS using Cells 5 and 6, along with all other cells, reduces fuel consumption because of relatively low overall energy use. For longer range missions such as Mission C, only the most energy-dense cells provide significant benefit, and the optimal BESS size reduces progressively as a function of cell energy density. The energy savings, shown in Figure 4.13 is dependent on the same variables and exhibits similar trends; however, energy savings are more limited, and, generally, savings increases with decreasing BESS size.
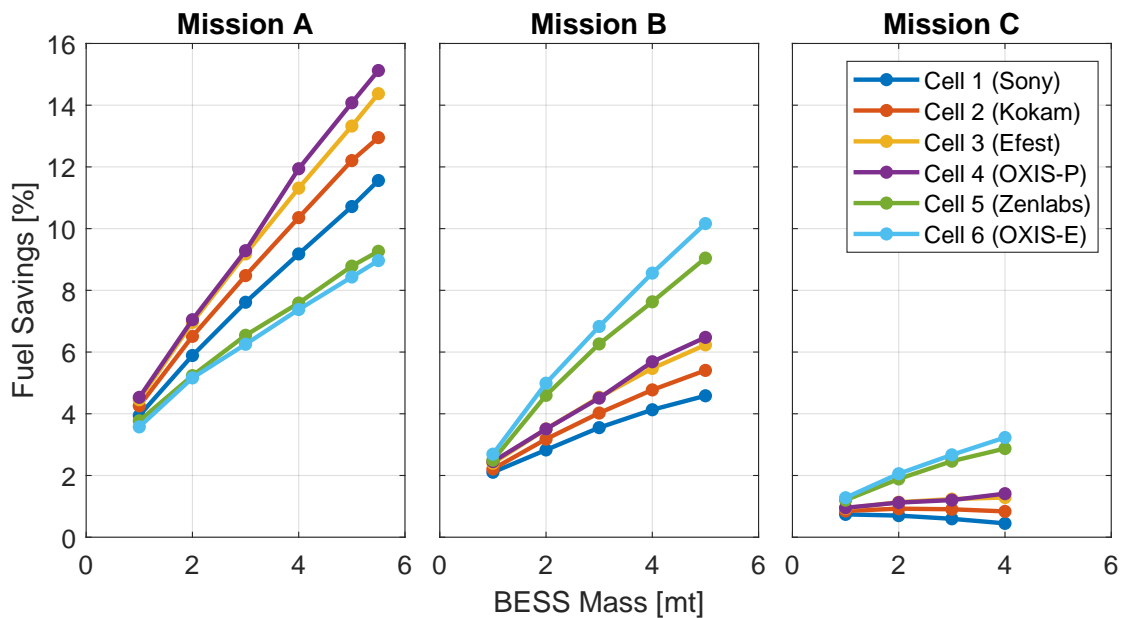
Figure 4.12: Total fuel savings by cell selection, BESS size, and mission range
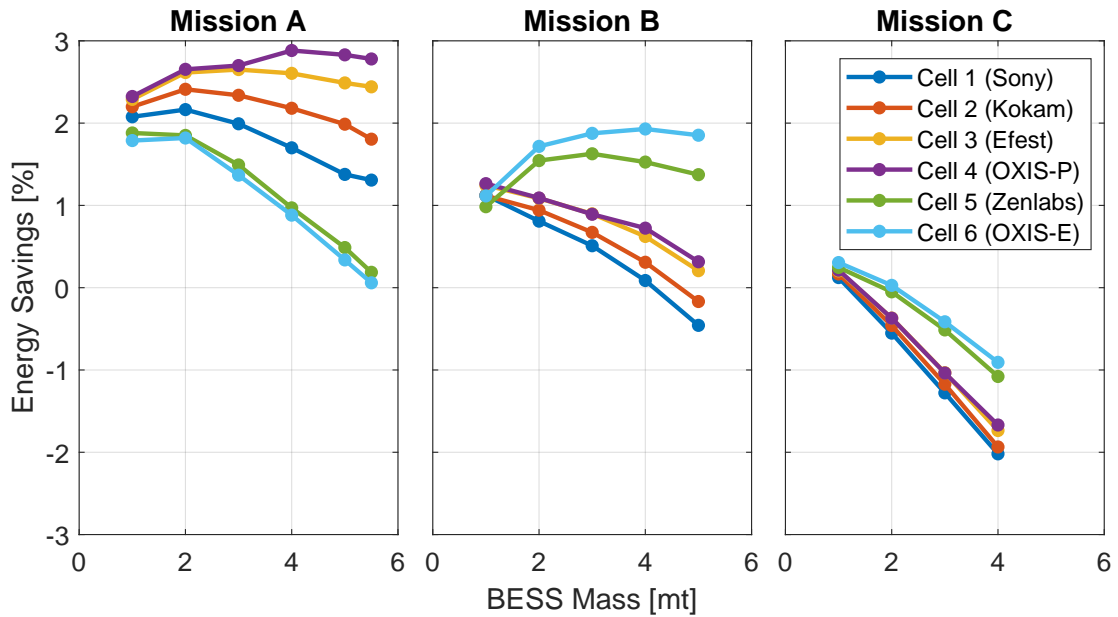
Figure 4.13: Total energy savings by cell selection, BESS size, and mission range

4.3 Utility Study

Flight history data sets of two CRJ-900 aircraft, EDV5152/9E5152 and ASH5982/YV5982, between the dates of 1/29/2019-2/4/2019 and 1/28/2019-2/3/2019 referred to as Group 1 and Group 2, respectively, were acquired from FlightAware.com. Group 1 features 31 flights between Midwest, Northeast, and Southeast hubs with a wide-spread distribution in range between 370 km and 1920 km. Group 2 features 41 flights primarily out of a single Southern hub serving the South and Midwest with range between 310 km and 1490 km but concentrated at 600 km and 1050 km. A point-to-point mapping of departure-to-arrival airports overlaid on a map of the US is shown in Figure 4.14, and Figure 4.15 shows the distribution of flight range.
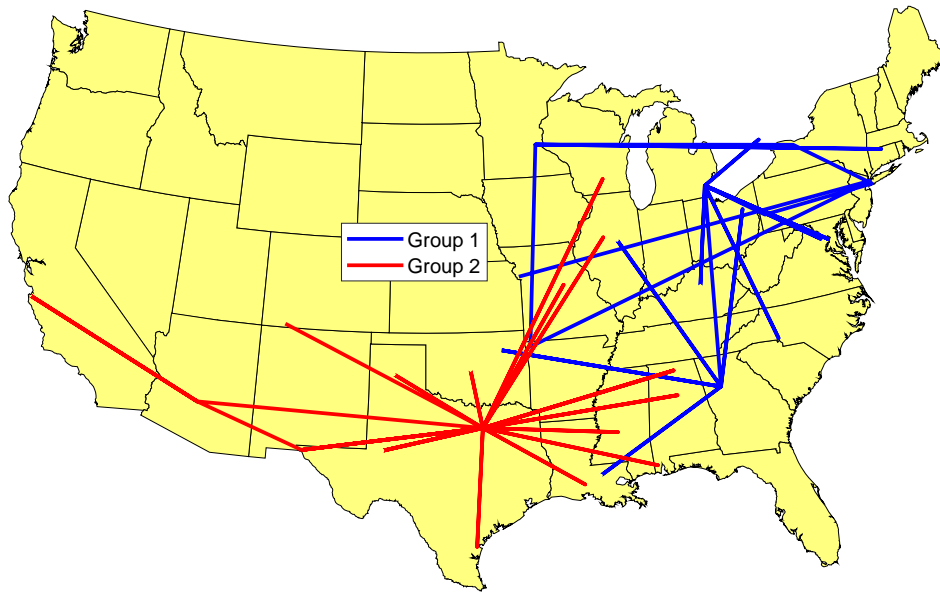
Figure 4.14: Point-to-point map of one-week set of missions flown in two separate regions by CRJ-900 aircraft
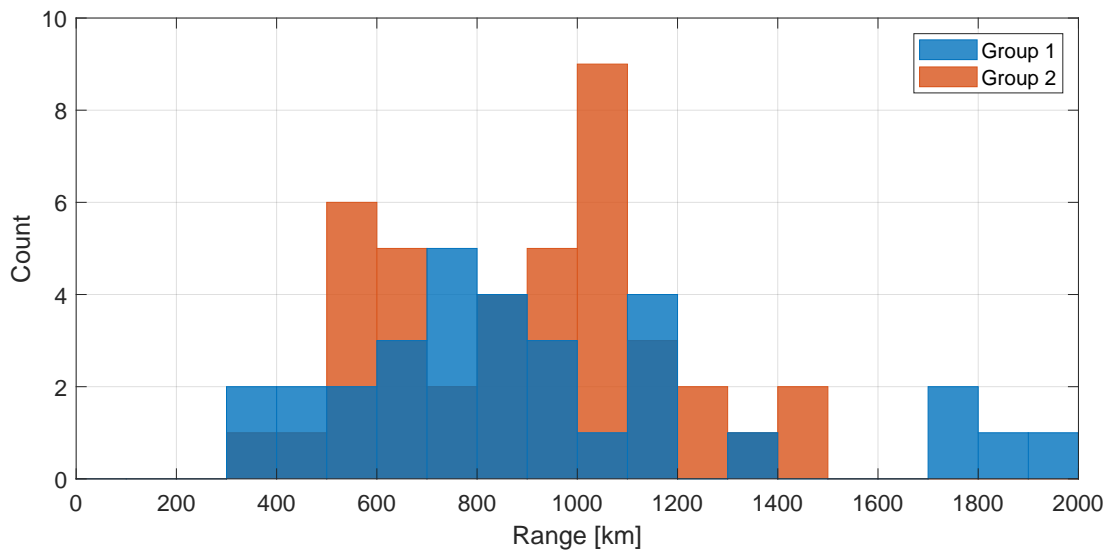
Figure 4.15: Distribution of mission range and number of missions for each group

The power function "power1" of the form $y = ax^b$ was used to fit the baseline fuel consumption evaluated for Missions A-C, and the curve fit was used determine baseline fuel consumption for all missions in Groups 1 and 2 (Figure 4.16). Further, the baseline fuel consumption and system parameters were used to define the maximum BESS size across all ranges. The polynomial function "poly22" of the form $z = p_{00} + p_{10}x + p_{01}y + p_{11}xy + p_{20}x^2 + p_{02}y^2$ was used to fit the hybrid fuel consumption evaluated for Missions A-C. For every mission, the baseline fuel consumption and maximum BESS size were estimated using the curve fit, and the hybrid fuel consumption was estimated using the surface fit for every BESS size up to the maximum allowable.
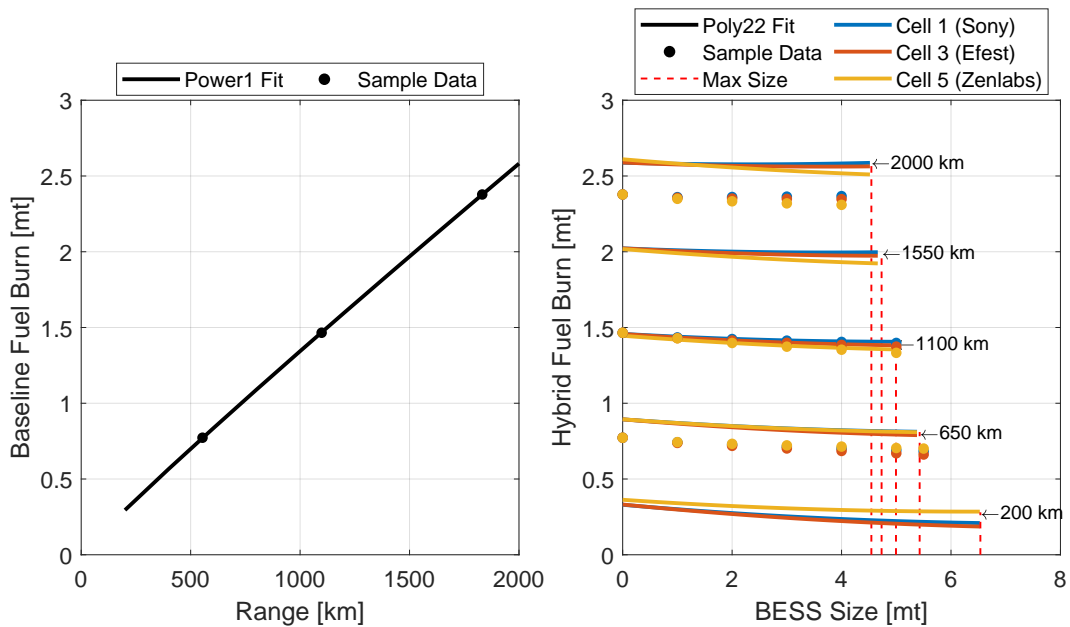
Figure 4.16: "power1" curve fit of baseline fuel consumption as a function of mission range and "poly22" surface fit of hybrid fuel consumption as a function of mission range and BESS size (for Cell 3)

The optimal BESS size and fuel savings corresponding to each mission in each group for Cell 3 is detailed in Figure 4.17. This study not only aims to extrapolate the mission savings to annual savings but also to evaluate the necessity of a modular BESS. The optimal fixed mass provides the maximum total fuel savings over all missions in a given group while satisfying the size limitation for every mission in that group. For both groups, the optimal fixed BESS size is the maximum allowable, as constrained by the longest range mission, and the optimal variable BESS size is also the maximum allowable, except for the four longest range missions, all in Group 1.

As energy density decreases, this threshold range, at which the optimal BESS size is reduced, decreases, and the size of the Cell 1 BESS is reduced for four missions each in Group 1 and 2. In contrast, as energy density increases (and current capability decreases), the BESS is expected to be downsized for the shortest range missions; the surface fit does estimate significantly reduced fuel savings using Cells 5 and 6, but does not predict maximum fuel savings away from the boundary for a range as low as 300 km. The larger the range of mission range, the larger the difference in fuel savings attained by the fixed and variable size BESSs. The largest difference occurs for either the longest and shortest missions depending on energy density. The longer the mission range and duration, in combination with reducing the fuel savings, practically reduces the number of missions possible in a given time, neglecting all other factors of flight planning. However, the shorter and more frequent the mission, the higher the rate of discharge, the higher the heat generation, and the higher the cycle count, which all negatively impact the life cycle of the BP.

The weekly fuel savings for each cell is assumed to be representative of the distribution of flights flown by each respective aircraft over the course of a year. Using the price of jet fuel in Q1 of 2019, $80/bbl, the minimum annual fuel savings of 100 mt (Group 1, fixed,
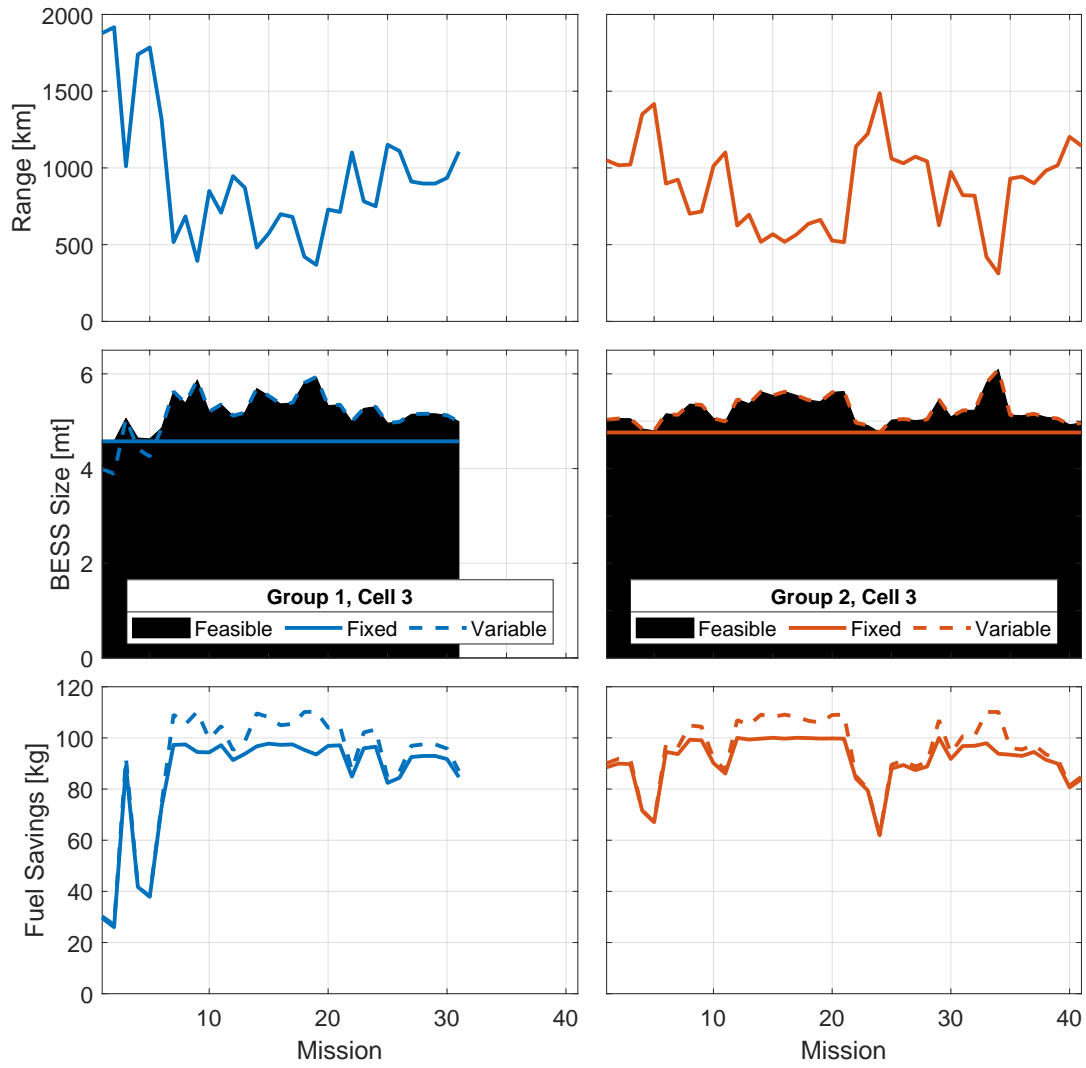
Figure 4.17: Optimal BESS size and fuel savings using Cell 3 for all missions in each group

Cell 1) equates to $63,000 of savings, while the maximum annual fuel savings of 225 mt (Group 2, variable, Cell 6) equates to $142,000 of savings (Figure 4.18). The difference in fuel savings between Group 1 and 2 is primarily driven by the difference in the number of missions.

Enabling the BESS size to be varied results in an average increase in fuel savings of 6.5% and 4.0% for Group 1 and 2, respectively. The longest range mission is 1940 km in Group 1 compared to 1490 km in Group 2, but both groups predominantly consist of missions between 500 km and 1200 km. Fuel savings increases with decreasing range for Cells 1-4 and is greatest for Cells 5 and 6 near 1100 km; thus, the fixed sizing is most limiting for Group 1, and the variable sizing offers more benefit. The histogram in Figure 4.18 illustrates which cells and groups are most inhibited by the fixed sizing.

More specifically, approximately 70% of Group 1 missions are under 1000 km of range, where the most energy-dense cells are limited. Variable sizing enables a 6.5% increase in fuel savings for Cells 1 and 2 and a 5.3% for Cells 5 and 6 in Group 1 missions. In Group 2, the benefit of variable sizing is nearly equivalent for Cells 1-2 and 5-6 at 3.5% because 46% of missions are less than 900 km of range and 54% are between 900 km and 1500 km. Variable sizing is most beneficial for the mixed-use cells, Cells 3 and 4, in both groups, increasing fuel savings by 6.9% and 5%, because of significantly higher savings in short-range missions.

While there is a larger difference in percent fuel savings between Cells 3-4 and 5-6 in short-range missions than in medium-range missions, 100% more fuel is burned by the baseline aircraft in medium-range missions. The fuel savings attained by Cell 6 in medium-range missions is sufficient to overcome its performance limitations in short-range

missions and to consistently offer the most fuel savings, though Cell 4 matches Cell 5 in a fixed-size BESS and outperforms Cell 5 in a variable-size BESS in both groups.
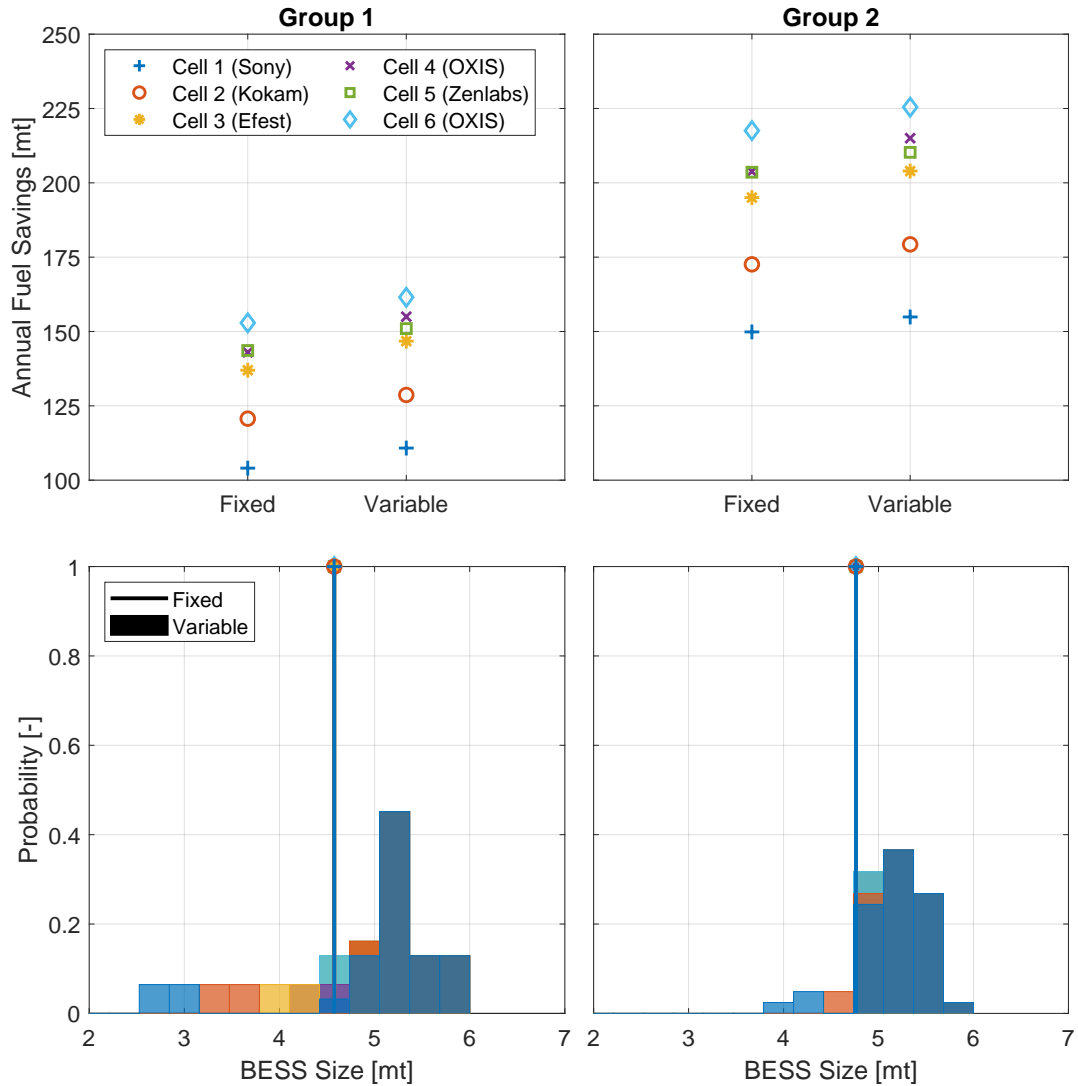
Figure 4.18: Annual fuel savings and BESS size variability as a function of cell selection and mission group

Chapter 5: Conclusion

5.1 Summary

Historically, volatile and generally increasing oil prices have motivated improvements in fuel efficiency in the transportation industry. Until recently, most all commercial vehicles and, still, all aircraft depend entirely on fossil fuels. Petroleum and other liquid fuels (natural gas, biofuels, gas-to-liquids, and coal-to-liquids) are the source for 96% of global transportation energy consumption. Of the US transportation sector energy use in 2018, petroleum products accounted for 92% and electricity for less than 1%, nearly all in mass transit systems. Because of the transportation sector's heavy reliance on fossil fuels and limited efficiency of on-board, combustion-based power plants, in the US in 2019, it was responsible for 36% of emissions while only consuming 28% of energy, and, in 2050, it is projected to remain responsible for 36% of emissions, even with reduced percentage of total energy consumption at 24%.

Light-duty vehicles are currently the main source of consumption and emissions and are predicted to remain so. However, the consumption of the aviation industry is predicted to double, increasing by 10 quadrillion Btu, nearly matching the 15 quadrillion Btu increase in consumption of light-duty vehicle. The Asia-Pacific market is projected to be home to 66% of the middle-class population globally by 2030 and primary contributor to global aviation

growth through 2030. Africa, projected to have the largest working class population by 2040, will likely be responsible for continued growth in aviation well into the future.

While significant progress toward wide-spread adoption of electric road vehicles has been made, the aviation industry has been lagging, though, in many regards, electrification in aviation has significantly more hurdles. The MEA initiative dramatically influenced the development of the Boeing 787 and Airbus A380, which feature substantial increases in electric power generation by the engines and consumption in auxiliary applications. A multitude of TEDP aircraft, which extend the utilization of electric power to propulsion, have been conceptualized and studied, showing potential for up to 70% FBR and driving research and development of the enabling technologies in academia, industry, and government.

Still, TEDP aircraft rely solely on fossil fuels for propulsive power. The hybridization (fuel and BESS) and full electrification (BESS) are considered to be revolutionary advances in aircraft technology, and the inclusion of an on-board ESS is solely capable of enabling zero-emissions flight (locally). Fully-electrified urban air mobility and low-capacity (<20 passengers), regional aircraft are being actively developed, as SOA battery technology is proven to be capable in these applications. However, results presented in this work show SOA and near-term battery technology to be capable in full-size (up to 100 passengers), regional jets with range up to 2000 km, which presents significantly greater potential savings due to relative flight frequency and fuel consumption.

The Bombardier CRJ-900 aircraft and its General Electric CF34 engine were referenced in the design of the HEDP concept aircraft. The regional aircraft maintains its design range of 3700 km with a payload of 8.2 mt. The airframe and engine, in the form of a turboshaft, were modified assuming technology improvements projected for 2030. The technology improvements and electrification of the propulsion system (TEDP conversion) alone result

113

in 23% FBR in an 1100 km mission (Mission B) [60]. It is optimal for the concept to be configured with the TEDP system for ranges exceeding 2000 km.

The model equations and parameters constituting the system were outlined. The airframe and turbomachinery models, provided by GT-ASDL and converted to steady-state maps, were validated against simulations performed in native software, GT-HEAT. Sizing and performance of the inverters and motors powering the fans were provided by OSU-CHPPE and UW-EMPEC, respectively, and were referenced to estimate sizing and performance of the remaining powertrain components, except the EDS, which was also designed by GT-ASDL. The battery cell performance was characterized by referencing datasheet information and static and dynamic test data. The sizing of the BESS is a variable studied in this work but is constrained by the MTOW and DC link voltage.

The system model was implemented in MATLAB to be paired with a DP algorithm such that the design and control of the BESS could be analyzed in detail. In full, the system was considered to have two states - the SOC and fuel mass. Analysis showed that the fuel consumption was insensitive to variations in fuel mass in the missions studied in this work. Instituting the fuel mass as a time-varying, external input rather than a state variable, was shown to significantly reduce computational time, increase accuracy, and maintain SOC trajectory characteristics. Accuracy was improved by re-initializing the DP algorithm using fuel consumption estimates that account for the addition of the BESS and optimal energy management.

The FBR and energy management strategy and their dependence on cell characteristics, BESS sizing, and mission range were evaluated. Six cell models (three SOA, three future technology), discrete BESS sizes (up to the MTOW), and three mission ranges (ranges between 550 km and 1850 km) were considered. FBR, as a percentage, increases with

decreasing mission range; increasing BESS size, except for BPs with relatively low energy density; and increasing energy density, unless the BP is current-limited in a short-duration mission. Note that the energy density at the pack level is both influenced by the cell energy density and the DC-to-DC converter sizing, which scales linearly as a function of the BP's maximum rated continuous power, and packaging efficiency is neglected. The highest FBR achieved in Missions A-C are 15.1% (117 kg, Cell 4, 5.5 t), 10.2% (149 kg, Cell 6, 5.0 t), and 3.2% (77 kg, Cell 6, 4.0 t), respectively.

The system always operates in charge depleting mode; the final SOC is not constrained and no cost is included if the final SOC is not at 10%. The only cases when the BP is not full depleted occur when the BP is current-limited. Generally, the charging that occurs is at relatively low power, is largely driven by differences in TG output power and FA power consumption when idling in descent, and can be neglected. However, descent is the segment of the simplified mission profile in which the engine control most significantly deviates from the baseline because of the low-power operation. Otherwise, the power split is relatively constant in climb and cruise with increasing magnitude in cruise, though generally with higher absolute power in climb. With increasing mission range, a larger percent of stored energy is used in cruise and descent, and mean discharge power, mean discharge rate, and mean heat generation decrease. Similar trends are observed with decreasing BESS size, in addition to decreasing peak discharge power, peak discharge rate, and peak heat generation. Variation by cell can be generally described as a high ratio of power to energy density results in increased power and duration of peak-power bursts and decreased mean power, and vice versa.

The results and analysis conducted using the simplified missions were assumed to be reasonable approximations of actual flights. The data was used to estimate savings of the

concept aircraft, considering both a fixed and variable-size BESS, in two different week-long groups of missions typical for a CRJ-900. The lower the range of mission distance, the lower the benefit of designing a modular battery pack. Mission distance in Group 1 ranges between 370 km and 1920 km and, even then, a modular BESS only enables a 6.4% increase in FBR on average. However, for the concept to fulfill the maximum payload/range mission, the BESS must be removable at a minimum. The lower the mean mission range for a given group of missions, the higher the savings in a given time. This is less related to the mission range and more related to the frequency of missions. The percent FBR does increase with decreasing mission range, but the highest absolute FBR is possible in the medium-range mission. Generally, though short-range missions can be flown more frequently. In both Group 1 and Group 2, the BESS is frequently sized at the maximum allowable size, except for power-dense BPs being reduced in size for long-range missions, and vice-versa. For the mission groups studied, FBR generally increases with increasing energy density and always increases if modular. The minimum annual FBR of 100 mt (Group 1, fixed, Cell 1) equates to $63,000 in savings, while the maxmimum FBR of 225 mt (Group 2, variable, Cell 6) equates to $142,000 in savings.

5.2 Contributions

This publication details the development of the Map-based Aircraft Propulsion Simulator (tMAPS), and its application in optimizing the size and control of a BESS in a HEDP regional jet aircraft. tMAPS is responsible for interfacing ROMs of aircraft subsystems to construct a system model and coupling the system model to a DP algorithm. The generation and implementation of performance maps are proven to result in negligible losses in accuracy when constrained appropriately, e.g. dynamics can be limited in turbomachinery

116

operation, such that results remain valid. The tool developed here is validated against the NPSS-based Georgia Tech Hybrid Electric Aircraft Test-bed (GT-HEAT). The fuel mass estimation process, developed to reduce problem complexity, is shown to significantly reduce computation time, while slightly improving accuracy. SOA battery technology with energy density of 200 Wh/kg is evaluated and shown to enable significant reduction in fuel consumption, while most previous studies have only considered advanced technology with energy densities of 750-1500 Wh/kg. Benefits using SOA battery technology are limited to short-range missions, but extrapolation to global operations shows potential for substantial reduction in fuel consumption. The optimal energy management strategy is evaluated as a function of BESS size, cell chemistry, and mission and profile to deduce system-level implications.

5.3   Future Work

Manufacturer specified current limits significantly inhibit cell performance but thermal and aging parameters must be characterized to better define these limits. Further, the limit definition should be modified to enable continuous peak power limit evaluation [55].

The design mission and engine design and sizing procedure limit the benefit of the BESS, which offers the most advantage in adverse conditions. Dynamic mission profiles and operation at conditions distanced from the design point will enable better utilization of the BP, i.e. a more substantial increase in mean efficiency of the propulsion power supply. Further, down-sizing the engine, while considering the BESS to be a critical component, enables design of the two power systems to be co-optimized. However, tMAPs is not an appropriate tool to be used for optimize the design of components and/or subsystems in parallel.

Predicting the payback period and return on investment requires thermal and aging characteristics of the cell and detailed design of the BESS, including the BMS and TMS, with consideration for the safety requirements of aerospace applications. The economics will result in the best estimate of when battery energy storage systems will be widely integrated in aircraft.

There is likely benefit to maintaining a small amount of energy storage for the maximum range and payload mission for buffering transients and supplying non-propulsive loads, both in-taxi and in-flight. This use-case may actually benefit the reported energy savings, reducing the weight impact and exploiting lower-power, less-efficient auxiliary systems. These systems are also most prone to failure, and airline vulnerability to unplanned maintenance should be sufficient for economic-viability of small BESSs in MEA. Further, gradual increases in the level of hybridization may be necessary as regulations are still in development.

Bibliography

[1] Boeing, "Commercial Market Outlook 2019-2038," Tech. rep., The Boeing Company, Sept. 2019.

[2] Lee, D. S., Pitari, G., Grewe, V., Gierens, K., Penner, J. E., Petzold, A., Prather, M. J., Schumann, U., Bais, A., Berntsen, T., Iachetti, D., Lim, L. L., and Sausen, R., "Transport impacts on atmosphere and climate: Aviation," *Atmospheric Environment*, Vol. 44, No. 37, pp. 4678–4734, Dec. 2010, doi: 10.1016/j.atmosenv.2009.06.005.

[3] Yim, S. H. L., Lee, G. L., Lee, I. H., Allroggen, F., Ashok, A., Caiazzo, F., Eastham, S. D., Malina, R., and Barrett, S. R. H., "Global, regional and local health impacts of civil aviation emissions," *Environmental Research Letters*, Vol. 10, No. 3, March 2015, doi: 10.1088/1748-9326/10/3/034001.

[4] Grobler, C., Wolfe, P. J., Dasadhikari, K., Dedoussi, I. C., Allroggen, F., Speth, R. L., Eastham, S. D., Agarwal, A., Staples, M. D., Sabnis, J., and Barrett, S. R. H., "Marginal climate and air quality costs of aviation emissions," *Environmental Research Letters*, Vol. 14, No. 11, Nov. 2019, doi: 10.1088/1748-9326/ab4942, Publisher: IOP Publishing.

[5] EIA, "Annual Energy Outlook 2020," Tech. rep., EIA, Jan. 2020.

[6] IEA, "World Energy Outlook 2019," Tech. rep., IEA, Paris, France, 2019.

[7] Kharas, H., "The Emerging Middle Class in Developing Countries," Tech. Rep. 285, The Brookings Institution, Paris, France, Jan. 2010.

[8] AbdElhafez, A. A. and Forsyth, A. J., "A Review of More-Electric Aircraft," Vol. 13, The Military Technical College, Cairo, Egypt, pp. 1–13, May 2009, doi: 10.21608/asat.2009.23726.

[9] IATA, "Aircraft Technology Roadmap to 2050," Tech. rep., IATA, Geneva, Switzerland, June 2019.

[10] Kim, H. D., Felder, J. L., Tong, M. T., and Armstrong, M., "Revolutionary Aeropropulsion Concept for Sustainable Aviation: Turboelectric Distributed Propulsion," *21st International Symposium on Air Breathing Engines*, Busan, South Korea, Sept. 2013.

[11] Wen, J., Yu, Y., and Chen, C., "A Review on Lithium-Ion Batteries Safety Issues: Existing Problems and Possible Solutions," Sept. 2012, Library Catalog: www.ingentaconnect.com Publisher: American Scientific Publishers.

[12] Nitta, N., Wu, F., Lee, J. T., and Yushin, G., "Li-ion battery materials: present and future," *Materials Today*, Vol. 18, No. 5, pp. 252–264, June 2015, doi: 10.1016/j.mattod.2014.10.040.

[13] Fotouhi, A., Auger, D. J., Propp, K., Longo, S., and Wild, M., "A review on electric vehicle battery modelling: From Lithium-ion toward Lithium–Sulphur," *Renewable and Sustainable Energy Reviews*, Vol. 56, pp. 1008–1021, April 2016, doi: 10.1016/j.rser.2015.12.009.

[14] He, H., Xiong, R., Guo, H., and Li, S., "Comparison study on the battery models used for the energy management of batteries in electric vehicles," *Energy Conversion and Management*, Vol. 64, pp. 113–121, Dec. 2012, doi: 10.1016/j.enconman.2012.04.014.

[15] Schröder, R., Aydemir, M., and Seliger, G., "Comparatively Assessing different Shapes of Lithium-ion Battery Cells," *Procedia Manufacturing*, Vol. 8, pp. 104–111, 2017, doi: 10.1016/j.promfg.2017.02.013.

[16] Chen, D., Jiang, J., Kim, G.-H., Yang, C., and Pesaran, A., "Comparison of different cooling methods for lithium ion battery cells," *Applied Thermal Engineering*, Vol. 94, pp. 846–854, Feb. 2016, doi: 10.1016/j.applthermaleng.2015.10.015.

[17] Hannan, M. A., Hoque, M. M., Hussain, A., Yusof, Y., and Ker, P. J., "State-of-the-Art and Energy Management System of Lithium-Ion Batteries in Electric Vehicle Applications: Issues and Recommendations," *IEEE Access*, Vol. 6, pp. 19362–19378, 2018, doi: 10.1109/ACCESS.2018.2817655.

[18] Hernandez Lugo, D., Clarke, S., Miller, T., Redifer, M., and Trevor, F., "X-57 Maxwell Battery from Cell Level to System Level Design and Testing," July 2018, Library Catalog: NASA NTRS.

[19] Lequesne, B., "Automotive Electrification: The Nonhybrid Story," *IEEE Transactions on Transportation Electrification*, Vol. 1, No. 1, pp. 40–53, June 2015, doi: 10.1109/TTE.2015.2426573.

[20] Cloyd, J., "A status of the United States Air Force's More Electric Aircraft initiative," *IECEC-97 Proceedings of the Thirty-Second Intersociety Energy Conversion Engineering Conference (Cat. No.97CH6203)*, Vol. 1, pp. 681–686 vol.1, July 1997, doi: 10.1109/IECEC.1997.659272.

[21] Cutts, S., "A collaborative approach to the More Electric Aircraft," *2002 International Conference on Power Electronics, Machines and Drives (Conf. Publ. No. 487)*, pp. 223–228, June 2002, doi: 10.1049/cp:20020118, ISSN: 0537-9989.

[22] Faleiro, L., "Summary of the European Power Optimised Aircraft (POA) Project," ICAS, Hamburg, Germany, p. 4, Sept. 2006.

[23] Rosero, J., Ortega, J., Aldabas, E., and Romeral, L., "Moving towards a more electric aircraft," *IEEE Aerospace and Electronic Systems Magazine*, Vol. 22, No. 3, pp. 3–9, March 2007, doi: 10.1109/MAES.2007.340500.

[24] Wheeler, P. and Bozhko, S., "The More Electric Aircraft: Technology and challenges." *IEEE Electrification Magazine*, Vol. 2, No. 4, pp. 6–12, Dec. 2014, doi: 10.1109/MELE.2014.2360720.

[25] Sarlioglu, B. and Morris, C. T., "More Electric Aircraft: Review, Challenges, and Opportunities for Commercial Transport Aircraft," *IEEE Transactions on Transportation Electrification*, Vol. 1, No. 1, pp. 54–64, June 2015, doi: 10.1109/TTE.2015.2426499.

[26] Sinnett, M., "787 No-Bleed Systems: Saving Fuel and Enhancing Operational Efficiencies," *Aero Quarterly*, Vol. 9, No. 4, pp. 6, 2007.

[27] "Boeing 787-8 (Dreamliner) Sample Analysis," 2005.

[28] Felder, J., Kim, H., and Brown, G., "Turboelectric Distributed Propulsion Engine Cycle Analysis for Hybrid-Wing-Body Aircraft," *47th AIAA Aerospace Sciences Meeting including The New Horizons Forum and Aerospace Exposition*, American Institute of Aeronautics and Astronautics, Orlando, Florida, Jan. 2009, doi: 10.2514/6.2009-1132.

[29] Kim, H. D., "Distributed Propulsion Vehicles," *27th International Congress of the Aeronautical Sciences*, Nice, France, Sept. 2010.

[30] Felder, J. L., Brown, G. V., Kim, H. D., and Chu, J., "Turboelectric Distributed Propulsion in a Hybrid Wing Body Aircraft," *20th International Symposium on Air Breathing Engines*, International Society for Air Breathing Engines, Gothenburg, Sweden, Sept. 2011.

[31] ATAG, "The Aviation Sector's Climate Action Framework," Tech. rep., ATAG, Nov. 2015.

[32] Kim, H. D., Perry, A. T., and Ansell, P. J., "A Review of Distributed Electric Propulsion Concepts for Air Vehicle Technology," *2018 AIAA/IEEE Electric Aircraft Technologies Symposium*, American Institute of Aeronautics and Astronautics, Cincinnati, Ohio, July 2018, doi: 10.2514/6.2018-4998.

[33] Hall, C. A. and Crichton, D., "Engine Design Studies for a Silent Aircraft," *Journal of Turbomachinery*, Vol. 129, No. 3, pp. 479–487, July 2007, doi: 10.1115/1.2472398, Publisher: American Society of Mechanical Engineers Digital Collection.

[34] Welstead, J. R. and Felder, J. L., "Conceptual Design of a Single-Aisle Turboelectric Commercial Transport With Fuselage Boundary Layer Ingestion," San Diego, CA, United States, Jan. 2016.

[35] Perullo, C. A., Trawick, D., Clifton, W., Tai, J. C. M., and Mavris, D. N., "Development of a Suite of Hybrid Electric Propulsion Modeling Elements Using NPSS," *Volume 1A: Aircraft Engine; Fans and Blowers*, American Society of Mechanical Engineers, Düsseldorf, Germany, June 2014, doi: 10.1115/GT2014-27047.

[36] Friedrich, C. and Robertson, P., "Hybrid-Electric Propulsion for Aircraft," *Journal of Aircraft*, Vol. 52, No. 1, pp. 176–189, Jan. 2015, doi: 10.2514/1.C032660.

[37] Pornet, C., Gologan, C., Vratny, P. C., Seitz, A., Schmitz, O., Isikveren, A. T., and Hornung, M., "Methodology for Sizing and Performance Assessment of Hybrid Energy Aircraft," *Journal of Aircraft*, Vol. 52, No. 1, pp. 341–352, Jan. 2015, doi: 10.2514/1.C032716.

[38] Pornet, C. and Isikveren, A., "Conceptual design of hybrid-electric transport aircraft," *Progress in Aerospace Sciences*, Vol. 79, pp. 114–135, Nov. 2015, doi: 10.1016/j.paerosci.2015.09.002.

[39] Voskuijl, M., van Bogaert, J., and Rao, A. G., "Analysis and design of hybrid electric regional turboprop aircraft," *CEAS Aeronautical Journal*, Vol. 9, No. 1, pp. 15–25, March 2018, doi: 10.1007/s13272-017-0272-1.

[40] Trawick, D. R., *A Methodology for the Determination of Optimal Operational Schedules of Hybrid Electric Architectures*, Ph.D. thesis, 2018.

[41] Perullo, C., Tai, J., and Mavris, D. N., "A New Sizing and Synthesis Environment for the Design and Assessment of Advanced Hybrid and Electric Aircraft Propulsion Systems," *22nd International Symposium on Air Breathing Engines*, Phoenix, AZ, Oct. 2015.

[42] Deng, D., "Li-ion batteries: basics, progress, and challenges," *Energy Science & Engineering*, Vol. 3, No. 5, pp. 385–418, 2015, doi: 10.1002/ese3.95, _eprint: https://onlinelibrary.wiley.com/doi/pdf/10.1002/ese3.95.

[43] Chemali, E., Preindl, M., Malysz, P., and Emadi, A., "Electrochemical and Electrostatic Energy Storage and Management Systems for Electric Drive Vehicles: State-of-the-Art Review and Future Trends," *IEEE Journal of Emerging and Selected Topics in Power Electronics*, Vol. 4, No. 3, pp. 1117–1134, Sept. 2016, doi: 10.1109/JESTPE.2016.2566583.

[44] Vetter, J., Novák, P., Wagner, M. R., Veit, C., Möller, K. C., Besenhard, J. O., Winter, M., Wohlfahrt-Mehrens, M., Vogler, C., and Hammouche, A., "Ageing mechanisms in

lithium-ion batteries," *Journal of Power Sources*, Vol. 147, No. 1, pp. 269–281, Sept. 2005, doi: 10.1016/j.jpowsour.2005.01.006.

[45] Zubi, G., Dufo-López, R., Carvalho, M., and Pasaoglu, G., "The lithium-ion battery: State of the art and future perspectives," *Renewable and Sustainable Energy Reviews*, Vol. 89, pp. 292–308, June 2018, doi: 10.1016/j.rser.2018.03.002.

[46] Etacheri, V., Marom, R., Elazari, R., Salitra, G., and Aurbach, D., "Challenges in the development of advanced Li-ion batteries: a review," *Energy & Environmental Science*, Vol. 4, No. 9, pp. 3243–3262, Aug. 2011, doi: 10.1039/C1EE01598B, Publisher: The Royal Society of Chemistry.

[47] Fotouhi, A., Auger, D., O'Neill, L., Cleaver, T., and Walus, S., "Lithium-Sulfur Battery Technology Readiness and Applications—A Review," *Energies*, Vol. 10, No. 12, pp. 1937, Nov. 2017, doi: 10.3390/en10121937.

[48] Zhang, H. and Chow, M.-Y., "Comprehensive dynamic battery modeling for PHEV applications," *IEEE PES General Meeting*, pp. 1–6, July 2010, doi: 10.1109/PES.2010.5590108, ISSN: 1944-9925.

[49] D'Arpino, M., Cancian, M., Sergent, A., Canova, M., and Perullo, C., "A simulation tool for battery life prediction of a Turbo-Hybrid-Electric Regional Jet for the NASA ULI Program," *AIAA Propulsion and Energy 2019 Forum*, American Institute of Aeronautics and Astronautics, Indianapolis, IN, Aug. 2019, doi: 10.2514/6.2019-4469.

[50] Yann Liaw, B., Nagasubramanian, G., Jungst, R. G., and Doughty, D. H., "Modeling of lithium ion cells—A simple equivalent-circuit model approach," *Solid State Ionics*, Vol. 175, No. 1, pp. 835–839, Nov. 2004, doi: 10.1016/j.ssi.2004.09.049.

[51] Cai, Y., Cancian, M., D'Arpino, M., and Rizzoni, G., "A generalized equivalent circuit model for large-scale battery packs with cell-to-cell variation," *IEEE National Aerospace & Electronics Conference*, Dayton, OH, p. 7, Aug. 2019.

[52] Christopherson, J. P., "Battery Test Manual For Electric Vehicles," Tech. Rep. INL/EXT-15-34184, Idaho National Laboratory, June 2015.

[53] He, H., Xiong, R., and Fan, J., "Evaluation of Lithium-Ion Battery Equivalent Circuit Models for State of Charge Estimation by an Experimental Approach," *Energies*, Vol. 4, No. 4, pp. 582–598, April 2011, doi: 10.3390/en4040582, Number: 4 Publisher: Molecular Diversity Preservation International.

[54] Jiang, S., "A Parameter Identification Method for a Battery Equivalent Circuit Model," April 2011, doi: 10.4271/2011-01-1367.

[55] Sun, F., Xiong, R., He, H., Li, W., and Aussems, J. E. E., "Model-based dynamic multi-parameter method for peak power estimation of lithium–ion batteries," *Applied Energy*, Vol. 96, pp. 378–386, Aug. 2012, doi: 10.1016/j.apenergy.2012.02.061.

[56] Saw, L. H., Ye, Y., and Tay, A. A. O., "Integration issues of lithium-ion battery into electric vehicles battery pack," *Journal of Cleaner Production*, Vol. 113, pp. 1032–1045, Feb. 2016, doi: 10.1016/j.jclepro.2015.11.011.

[57] Xia, G., Cao, L., and Bi, G., "A review on battery thermal management in electric vehicle application," *Journal of Power Sources*, Vol. 367, pp. 90–105, Nov. 2017, doi: 10.1016/j.jpowsour.2017.09.046.

[58] Williard, N., He, W., Hendricks, C., and Pecht, M., "Lessons Learned from the 787 Dreamliner Issue on Lithium-Ion Battery Reliability," *Energies*, Vol. 6, No. 9, pp. 4682–4695, Sept. 2013, doi: 10.3390/en6094682, Number: 9 Publisher: Multidisciplinary Digital Publishing Institute.

[59] Swanke, J., Bobba, D., Jahns, T. M., and Sarlioglu, B., "Comparison of Modular PM Propulsion Machines for High Power Density," *2019 IEEE Transportation Electrification Conference and Expo (ITEC)*, pp. 1–7, June 2019, doi: 10.1109/ITEC.2019.8790587, ISSN: 2377-5483.

[60] Perullo, C., Alahmad, A., Wen, J., D'Arpino, M., Canova, M., Mavris, D. N., and Benzakein, M. J., "Sizing and Performance Analysis of a Turbo-Hybrid-Electric Regional Jet for the NASA ULI Program," *AIAA Propulsion and Energy 2019 Forum*, American Institute of Aeronautics and Astronautics, Indianapolis, IN, Aug. 2019, doi: 10.2514/6.2019-4490.

[61] Sundstrom, O. and Guzzella, L., "A generic dynamic programming Matlab function," *2009 IEEE Control Applications, (CCA) Intelligent Control, (ISIC)*, pp. 1625–1630, July 2009, doi: 10.1109/CCA.2009.5281131, ISSN: 1085-1992.

[62] Ramunno, M., *Control Optimization of Turboshaft Engines for a Turbo-electric Distributed Propulsion Aircraft*, Master's thesis, The Ohio State University, Columbus, OH, March 2020.

[63] "Cree CAS325M12HM2 Datasheet," April 2018.

[64] "Lithium Ion Rechargeable Battery Technical Information for Model Number: US18650VTC6," June 2015.

[65] "Superior Lithium Polymer Battery (SLPB) Cell Specification for Model Number: SLPB065070180," Jan. 2017.

[66] "Efest IMR18650 3500mAh 20A," March 2020.

[67] "OXIS POA000343 Cell Datasheet," Nov. 2019.

[68] "Zenlabs Glide Drone Cells," March 2020.

[69] "OXIS POA000412 Cell Datasheet," Nov. 2019.

[70] "Pratt & Whitney PW1000G," March 2020, Wikipedia, Page Version ID: 946504286.

[71] Norris, G., "P&W plans PW8000 first run for 1999," Feb. 1998, Library Catalog: www.flightglobal.com.

[72] Schwarz, F. M., Sheridan, W. G., and Levasseur, G., "Geared turbofan high gearbox power density," Sept. 2015, Library Catalog: Google Patents.

[73] Bellman, R., "The theory of dynamic programming," *Bulletin of the American Mathematical Society*, Vol. 60, No. 6, pp. 503–515, Nov. 1954, Publisher: American Mathematical Society.